

# M.Sc. Thesis

---

## Fracture Network Prediction in the Geneva Basin: A Geothermal Case Study

Mahmood Abdulaziz Alhamad

### Abstract

The aim of this study is to reduce the risk of the ongoing Geothermal exploration effort in Geneva Basin by estimating the influence of the natural fracture on the reservoir properties. A Discrete Fracture Network (DFN) was generated to resemble the fracture network in the Lower Cretaceous carbonate reservoir. The DFN modelling approach is using a novel workflow that is based on a geomechanical forward modelling simulation approach. Two 2D seismic lines and well data, including interpreted fractures using Borehole Image (BHI) log, were used to prepare the model inputs. Some results were derived from the fracture data that were also used to prepare the model inputs. In general, the fracture data have fairly constant orientation along the Lower Cretaceous interval. In this study the fractures are assumed to be formed under a single tectonic regime. However, when partitioning the fractures in different stratigraphic formations, a change in the direction of the fractures with depth is observed. This observation could be explained by the variation in rock's stiffness between different stratigraphic formations.

Two techniques were used to model the subsurface fracture network: paleo-tectonic stress inversion and fracture network forward modelling techniques. The modelled DFN resembles the fractures geometry at the well location whereas away from the well the model is constrained by the subsurface fault geometry and far-field tectonic stress. Moreover, the modelled DFN consists of multiple 2 meters thick layers where each layer include a layer-bound fracture network. One of the main limitations of this approach is that it can not consider multiple tectonic regimes to simulate the fracture network. In addition, this approach requires large computational power.



Delft University of Technology



# Fracture Network Prediction in the Geneva Basin

## A Geothermal Case Study

---

THESIS

submitted in partial fulfillment of the  
requirements for the degree of

MASTER OF SCIENCE

in

APPLIED EARTH SCIENCES

by

Mahmood Abdulaziz Alhamad

Student number: 5605933  
Project duration: November 9, 2020 - August 30, 2021  
Thesis committee: Dr. P. B. R. Bruna, TU Delft, Chairman & Supervisor  
Prof. Dr. G. Bertotti, TU Delft, Supervisor  
Prof. Dr. D. F. Bruhn, TU Delft, Committee Member

This work was performed in:

Applied Geology Group  
Department of Geoscience & Engineering  
Faculty of Civil Engineering and Geosciences  
Delft University of Technology



**Delft University of Technology**

Copyright © 2021 Applied Geology Group  
All rights reserved.

# Abstract

---

The aim of this study is to reduce the risk of the ongoing Geothermal exploration effort in Geneva Basin by estimating the influence of the natural fracture on the reservoir properties. A Discrete Fracture Network (DFN) was generated to resemble the fracture network in the Lower Cretaceous carbonate reservoir. The DFN modelling approach is using a novel workflow that is based on a geomechanical forward modelling simulation approach. Two 2D seismic lines and well data, including interpreted fractures using Borehole Image (BHI) log, were used to prepare the model inputs. Some results were derived from the fracture data that were also used to prepare the model inputs. In general, the fracture data have fairly constant orientation along the Lower Cretaceous interval. In this study the fractures are assumed to be formed under a single tectonic regime. However, when partitioning the fractures in different stratigraphic formations, a change in the direction of the fractures with depth is observed. This observation could be explained by the variation in rock's stiffness between different stratigraphic formations.

Two techniques were used to model the subsurface fracture network: paleo-tectonic stress inversion and fracture network forward modelling techniques. The modelled DFN resembles the fractures geometry at the well location whereas away from the well the model is constrained by the subsurface fault geometry and far-field tectonic stress. Moreover, the modelled DFN consists of multiple 2 meters thick layers where each layer include a layer-bound fracture network. One of the main limitations of this approach is that it can not consider multiple tectonic regimes to simulate the fracture network. In addition, this approach requires large computational power.



# Acknowledgments

---

Praise to God Almighty for all His blessing and protection.

I would like to express my sincere gratitude towards everyone who contributed to my success in obtaining my Master degree including the staff of TUDelft, family, friends and Saudi Aramco.

Special thanks to my supervisor Dr. Pierre-Oliver Bruna, who took part in each phase of the project from step one and made it possible to enjoy researching. His knowledge and experience surely enhanced my learning curve at TUDelft. Above all, he always guided me through the research with such a unique character that is full of energy and positivity. I Would also like to thank Prof. Dr. Giovanni Bertotti for steering the project with his unquestionable knowledge. Moreover, I would like to thank Prof. Dr. David Bruhn for taking part in my thesis committee.

I would like to thank Prof. Dr. Andrea Moscariello and Dr. Ovie Eruteya from the University of Geneva for giving me the opportunity to work on the datasets of Geneva Basin. I also would like to thank Prof. Dr. Michael Welch and Dr. Simon Oldfield from the Technical University of Denmark (DTU) for providing the fracture network forward modelling tool (DFN Generator) and for the continuous support throughout the project.

In addition, I would like to express my gratitude to Saudi Aramco for sponsoring my studies and being there for me all the time providing support and making sure the experience in the Netherlands is well worth it. Having special place in my mind and heart, I would like to thank my RAK family for the infinite effort in providing all the possible support to make me successful in my career.

Finally, I am forever indebted to my parents for giving me the opportunities and experiences that have made me who I am. My deep and sincere gratitude to my wife Jumana for her endless, continuous and unparalleled love, help and support. My kids, Joud and Abdulaziz, you inspire me every day to grow and be better, also I would like to thank both of you for making the experiences of studying from home during the pandemic very quiet and peaceful!!! Furthermore, I am grateful to my sisters and brothers for always being there for me. This journey would not have been possible if not for every member of my family, and I dedicate this milestone to them.

Mahmood Abdulaziz Alhamad  
Delft, August 2021



UNIVERSITÉ  
DE GENÈVE



Denmark  
Technical  
University





# Table of Contents

---

<b>Abstract</b>	<b>iii</b>
<b>Acknowledgments</b>	<b>v</b>
<b>Table of Contents</b>	<b>viii</b>
<b>List of Figures</b>	<b>xii</b>
<b>List of Tables</b>	<b>xiii</b>
<b>1 Introduction</b>	<b>1</b>
1.1 Objectives . . . . .	1
1.2 Context of Study . . . . .	1
1.3 GEothermie 2020 program . . . . .	2
<b>2 Geological Setting</b>	<b>5</b>
2.1 Stratigraphy Framework . . . . .	6
2.1.1 Mesozoic . . . . .	6
2.1.2 Stratigraphy of Lower Cretaceous . . . . .	6
2.2 Tectonic and Structural Settings . . . . .	7
2.3 Aquifer Potential . . . . .	8
2.4 Regional Hydrogeology . . . . .	9
<b>3 Datasets</b>	<b>11</b>
3.1 Seismic Data . . . . .	11
3.1.1 Horizons Interpretations . . . . .	12
3.1.2 Faults Interpretations . . . . .	12
3.2 Borehole Data . . . . .	15
3.2.1 GGeo-01 well . . . . .	15
3.2.2 Petrophysical Logs . . . . .	15
3.2.3 Fracture Data . . . . .	16
<b>4 Methodology of Preparing the Data and Creating DFN Model</b>	<b>19</b>
4.1 General Workflow Chart for DFN Creation . . . . .	19
4.2 Structural Model . . . . .	19
4.2.1 modelling grid . . . . .	20
4.2.2 Fault Model . . . . .	20
4.3 Geomechanical Properties Calculations . . . . .	20
4.3.1 Properties Calculation Method . . . . .	20
4.3.2 Rock Stiffness Partitioning Approach . . . . .	21
4.4 Fracture Data Analysis . . . . .	22
4.5 Paleo-tectonic Stress Inversion Technique . . . . .	22
4.5.1 Methodology . . . . .	22
4.5.2 Boundary Conditions . . . . .	24

4.5.3	Assumption of Strain Rate and Strain Value . . . . .	24
4.5.4	Technique Limitations . . . . .	24
4.6	Fracture Forward Modelling Approach . . . . .	25
4.6.1	Methodology . . . . .	25
4.6.2	Boundary Conditions and Tool Limitations . . . . .	27
<b>5</b>	<b>Processing Data for DFN Model Generation</b>	<b>29</b>
5.1	Results and Interpretations of the Input Data for the DFN Generator . . . . .	29
5.1.1	Horizon Grid Construction . . . . .	29
5.1.2	Fault Model . . . . .	30
5.1.3	Geomechanical Logs and Rock Stiffness Partitioning Results . . . . .	31
5.1.4	Fracture Analysis and Stress State Interpretation . . . . .	34
5.1.5	Estimating Paleo-tectonic stresses and Strain tensors . . . . .	37
5.2	Discussion and Uncertainties of the Input Data for the DFN Generator . . . . .	40
5.2.1	The Structural Model Uncertainties . . . . .	40
5.2.2	Scaling Factor discussion and Young's Modulus Log Selection . . . . .	41
5.2.3	Rock Stiffness Partitioning Uncertainties . . . . .	41
5.2.4	Fracture Data Related Tectonic Events . . . . .	42
5.2.5	Uncertainties of the Paleo Stress Inversion Results . . . . .	42
<b>6</b>	<b>Forward Modelling (DFN Model Generation)</b>	<b>43</b>
6.1	Forward Modelling Inputs . . . . .	43
6.1.1	Default Input Parameters . . . . .	43
6.1.2	Young's Modulus and Poisson's Ratio Models Creation . . . . .	43
6.1.3	Strain Related Models . . . . .	44
6.2	DFN Model Creation Approach and Results . . . . .	44
6.2.1	DFN Model Creation Approach . . . . .	44
6.2.2	DFN Results . . . . .	45
6.3	Evaluation and Discussion of the Results . . . . .	47
6.3.1	Fracture Data Extraction and Analysis . . . . .	47
<b>7</b>	<b>Discussion</b>	<b>51</b>
7.1	Advantages and Limitation of the Modelling Approach . . . . .	51
7.2	Assumptions and Uncertainties . . . . .	52
7.3	Implication for Geothermal Exploration . . . . .	52
7.3.1	Applicability for Dynamic Modelling . . . . .	52
7.3.2	Uncertainties Mitigation and Model Improvement . . . . .	53
<b>8</b>	<b>Conclusion</b>	<b>55</b>
	<b>References</b>	<b>57</b>
	<b>Appendix A Fracture Data</b>	<b>61</b>
	<b>Appendix B Forward Modelling</b>	<b>65</b>
B.1	DFN Generator Input . . . . .	65
B.2	Large DFN Figures . . . . .	65

# List of Figures

---

1.1	Implementation plan for <i>GEothermie 2020</i> program to assess the geothermal potential in Geneva Basin. (modified after Moscariello (2016)) . . . . .	3
2.1	Location map of the study area showing the 2x2 km area of interest (AOI) in the yellow box. It is also showing the GGeo-01 well and the two seismic lines that are used in this project. (modified after (Lo, 2019)) . . . . .	5
2.2	Stratigraphic column of the subdivisions of the Lower Cretaceous interval that are penetrated by GGeo-01 well. The blue box indicated the formations of interest in this study. (modified after Lo (2019); Koumrouyan (2019)) . . . . .	7
2.3	Structural scheme of the Mesozoic-Cenozoic in Great Geneva Basin that shows two main structural trends. <b>1)</b> SW-NE Mesozoic structural lows that are related to the underlying Permo-Carboniferous basins that are located on front thrust of both Subalpine/Prealpine units and Salève ridge. <b>2)</b> Four main zones that is influenced by NW-SE trending wrench faults crossing both Bornes Plateau and Geneva Basin. The zones are as following: (I) Vuache; (II) Crusseilles; (III) Le Coin; (IV) Arve (Modified after (Clerc et al., 2015)). . . . .	8
2.4	NW to SE [A to A'] cross-section that illustrates the major stratigraphic units and the key structural elements in Geneva basin based on couple of 2D seismic lines in addition to well data. See Figure 2.3 for the location of the A-A' line projection. (modified after (Moscariello, 2019)) . . . . .	9
2.5	A) Temperature data in the Western Alpine Molasse Basin (WAMB) and average geothermal gradient (Chelle-Michou et al., 2017). B) Typology of the thermal anomalies identified in the WAMB. Approximate depth is shown for reference but may strongly vary from one place to another (Chelle-Michou et al., 2017). . . . .	10
3.1	Top view of the study area with locations of the used two seismic lines in this study, GG87-02 (Red line) and SIG-2015-L08 (Blue line). It also shows the time structural map for the Top of Jurassic horizon. . . . .	11
3.2	The provided velocity models along the following two horizons: A) Base of Cenozoic (BCen), and B) Top Jurassic (TJrsc) . . . . .	12
3.3	Two seismic sections show the most of the picked horizons, one of them shows the 2D fault interpretation. <b>A)</b> GG87-02 seismic line, <b>B)</b> SIG-2015-L08 seismic line. The locations of the seismic lines are shown in Figure 3.1. . . . .	13
3.4	Two seismic sections show the two main picked horizons in this study. <b>A)</b> GG87-02 seismic line, <b>B)</b> SIG-2015-L08 seismic line. The locations of the seismic lines are shown in Figure 3.1. . . . .	14
3.5	The acquired geophysical logs in addition to some calculated logs (Young's Modulus and Poisson ratio) and described lithology. . . . .	16
3.6	<b>(a)</b> (lower hemisphere) illustrating pole of each measurement and pole density of true dip orientation of the full fractures data. <b>(b)</b> Rose diagram representing the strike of the full fractures data. . . . .	17
3.7	Dip azimuth, Dip angle, and fracture intensity along the depth in the Lower Cretaceous interval in GGeo-01 well. . . . .	17

3.8	Rose diagrams representing the strike of the fractures in different groups based on their mechanical types. . . . .	18
4.1	The workflow for the fracture network modelling in this project. . . . .	19
4.2	Left: A cross-plot of P-wave velocity with Poisson’s ratio. Right: the best fit lines for the upper limit, lower limit and the middle curves of the carbonate data. (modified after (Kenter et al., 2007)) . . . . .	21
4.3	Work flow of the Paleo-tectonic Stress Inversion Technique. . . . .	22
4.4	Example of a tectonic stress domain. The x-axis is the stress ratio, and the y-axis is the orientation, $\theta$ , of the maximum horizontal stress relative to north. A point in the domain represents one simulation that is coloured with respect to the computed cost which varies between 0 and 1 (Maerten et al., 2016). . . . .	23
4.5	Simplified explanation of the process of fracture nucleation, propagation, and interaction in DFN Generator tool. Going from left to right, the figure illustrates the fracture formation process through time. The red circles are initial microfractures and blue rectangular are the layer-bound fractures. (modified after Welch et al. (2019)) . . . . .	26
5.1	Schematic cross-section illustrating the construction of the modelling grid horizons. The lower left figure shows the cross-section location within the study area in a map view. The formation well tops are presented in meters Measured Depth (mMD). . . . .	29
5.2	A) Structural model that includes the horizon grid and the faults. B) The modelling grid of all the formations in the Lower Cretaceous, (yellow=Vallorbe Fm), (blue=Gorges de l’Orbe Fm), (green=Upper Grand Essert Fm), (light blue & pink=Lower Grand Essert Fm), and (orange=Vuache Fm). In Lower Grand Essert light blue=soft and pink=stiff, based on the stiffness layering. C) Horizon grid showing that each formation is divided into 2 m thick layers. . . . .	30
5.3	A) 3D view shows the depth fault traces. B) 3D view shows the laterally extended fault into the 3D space with an angle of $68^\circ$ with respect to the north. C) Top view showing the faults parts that intersect the modelling grid. The red box represent the 2x2 km study area. . . . .	30
5.4	The blue lines represent the calculated velocity log using the SV-density relation in Equation 4.2. The orange line in <b>(A)</b> represents the measured P-sonic log in GGeo-01. The Orange line in <b>(B)</b> represents the measured P-sonic log in GGeo-01 scaled with a factor of (1.4). . . . .	31
5.5	Different RMSE values between the measured and calculated P-sonic using different scaling factors for the measured P-sonic. . . . .	32
5.6	A) Young’s modulus log that is calculated using the empirical relation provided by Yasar and Erdogan (2004) and using scaling factor of (1.4). B) Young’s modulus log that is calculated by Koumrouyan (2019). C) Both Young’s modulus logs on the same graph with the error bars for the Yasar and Erdogan scaled (1.4) log. The error bars represent the two scaling factors (1.2 & 1.6). D) The Poisson’s ratio log that is calculated using the empirical relation provided by Kenter et al. (2007). . . . .	33

5.7	A) Well logs from GGeo-01 well illustrating the Gamma ray $GR$ , Young's modulus $E$ , and Stiffness logs. It is also illustrating the cutoff values of $GR = 16API$ and $E = 53GPa$ . B) Well logs from GGeo-01 well illustrating the Gamma ray $GR$ , Young's modulus $E$ , Stiffness, Upscaled Stiffness, lithology, P-sonic, and density logs. The red and blue shaded layers represent stiff and soft rock intervals, respectively. . . . .	34
5.8	A) Rose diagram representing the strike of the fracture data. B) Lower hemisphere stereonet illustrating poles the fractures and pole density. C) Schematic block diagrams and correspondent pole measurement of fractures (Lower hemisphere) for a polymodal fracture pattern (Healy et al., 2015). . . . .	35
5.9	A) The density of the fractures poles with the interpretation of the related principle stress state. The green and blue arc regions show where the poles of the fractures are confined. B) Fractures strike rose diagram and the fractures pole density for the Upper Grand Essert , Lower Grand Essert, and Vuache Formations. C) Fracture data in GGeo-01. . . . .	35
5.10	Map view showing two faults, TF1 and SW3, at the level of the Lower Cretaceous represented by the dashed green lines. It is illustrating the shortest distances between GGeo-01 and the two faults. The red and blue lines are GG-87-02 and SIG-2015-L08 seismic lines, respectively. . . . .	36
5.11	A) Plain GG87-02 seismic-line. B) The green circles are highlighting the main discontinuities between the Base Cenozoic and Top Jurassic horizon interpretation. C) Illustrating the interpretation of the six faults. D) Illustrating the three selected faults for the fracture network modelling. . . . .	37
5.12	The top figures illustrating three fault geometries for the inversion tool. The bottom figures illustrating the displacement distribution resulted from the faults slip. All figures have the same colour scale (Red=0 m and blue=800 m). A) Faults with 4km lateral extension. B) Faults laterally extended to the edge of study area. C) Faults that are laterally extended to the edge of study area and cropped vertically from top and bottom. . . . .	38
5.13	Tectonic domain showing the result of the paleo-tectonic stress inversion on the data. Green circle represents the simulation with the best fit between the modelled stress and the observed fracture geometry. The black rectangle represent simulations with high fit 55%. . . . .	39
5.14	The input orientations of the maximum horizontal stress for different formations based on the fracture data interpretations. . . . .	40
5.15	An example of the principal strain tensors output with $\sigma_{H\max}$ orientation= $90^\circ$ along Upper Grand Essert Formation. . . . .	40
5.16	Distances between GGeo-01 well and the faults (TF1 & SW3) at Lower Cretaceous level with the following strike angles with respect to north: A) $40^\circ$ , B) $68^\circ$ , and C) $90^\circ$ . . . . .	41
6.1	Well log, upscaled well log, and populated properties in the modelling grid of both properties: A) Young's modulus and B) Poisson ratio. (Vertical exaggeration of the window=5). . . . .	44
6.2	The top figures illustrate the properties along one Upper Grand Essert Formation. The bottom figures illustrate the populated properties in the full modelling grid. (Vertical exaggeration of the window=3). . . . .	45

6.3	A) The modelling grid for the three formations, Upper Grand Essert (green), Lower Grand Essert (light blue), and Vuache Formations (orange). B) The populated DFN models in all layers for three the formations at (Location 3). (Vertical exaggeration of the window=5). . . . .	46
6.4	Map view of the study area showing the location of the generated DFN models in addition to the faults. . . . .	46
6.5	Examples of a single 2m layer of DFN for three formations around GEO-01 location. The correspondent fracture strike rose diagram from GEO-01 are presented in the right upper corner. . . . .	47
6.6	Close image for the modelled fracture geometry in Upper Grand Essert Fm. around GEO-01. A) DFN realisation at time=0.06 Ma, B) Final DFN realisation at time=1.00 Ma. . . . .	47
6.7	Histogram of the modelled fractures length in Upper Grand Essert Formation. . . . .	48
6.8	Fracture dip azimuth histogram on one DFN layer in Upper Grand Essert Fm. for A) Full exported data from one layer in Location 1, B) Filtered data using fracture length cutoff=3.25m in Location 1. . . . .	49
6.9	Top: Fracture dip azimuth histogram. Bottom: Fracture dip Angle histogram. . . . .	50
7.1	Three different fault model configurations in the study area. Model 1 is the base model that has been used in this study. Model 2 and 3 are possible fault models that are provided by the Department of Earth Science of the University of Geneva. . . . .	54
A.1	Categorization of different lithology layers. . . . .	61
A.2	This figures shows the fractures data for the 10 different lithology layers. Full Data include all the fractures. 2 Sets Data include on the the NNE-SSW and the E-W sets. . . . .	62
A.3	This figures shows the fractures data for the 9 different geomechanical layers. Full Data include all the fractures. 2 Sets Data include on the the NNE-SSW and the E-W sets. . . . .	63
A.4	This figures shows the fractures data for the 5 different lithological formation. Full Data include all the fractures. 2 Sets Data include on the the NNE-SSW and the E-W sets. . . . .	64
B.1	Main settings . . . . .	65
B.2	Mechanical properties inputs . . . . .	66
B.3	Stress State inputs . . . . .	66
B.4	Outputs control . . . . .	67
B.5	Control parameters . . . . .	67
B.6	DFN result in U.Grand Essert Formation. The correspondent strike rose diagram is presented in the right upper corner. . . . .	68
B.7	DFN result in L.Grand Essert Formation. The correspondent strike rose diagram is presented in the right upper corner. . . . .	69
B.8	DFN result in Vuache Formation. The correspondent strike rose diagram is presented in the right upper corner. . . . .	70

# List of Tables

---

3.1	GEO-01 well information Lo (2019).	15
3.2	GEO-01 well logging details Lo (2019).	15
3.3	Lower Cretaceous formation tops in GEO-01 well.	16
5.1	Results of regression equations and the correlation coefficients (Yasar and Erdogan, 2004).	32
5.2	The input used in the stresses calculations.	39
6.1	Mechanical properties and stress state default input parameters that are used in the DFN Generation.	43





# Introduction

---

## 1.1 Objectives

The main objective of this study is to reduce the risk of the geothermal exploration effort in Geneva Basin by estimating the influence of the natural fracture on the reservoir properties. A Discrete Fracture Network (DFN) was constructed to resemble the fracture network in the Lower Cretaceous carbonate reservoir. The DFN modelling workflow includes paleo-tectonic stress inversion and geomechanical forward modelling simulation approaches. The framework of the fracture network creation is using two 2D seismic lines, well data, and a number of empirical relationship. The questions that this study tries to answer are:

- What are the geomechanical characteristics of the rocks in the Lower Cretaceous unit?
- What is the tectonic regime and the paleo-stress configuration during the creation of the observed fractures in GGeo-01 well?
- How to model a fracture network that is constrained by the available data?
- What are the strengths, limitations, assumptions, and uncertainties that are related to the predicted 3D fracture network using the adapted approach?
- How applicable is the produced DFN to the geothermal application?
- How to mitigate the uncertainties and to improve the model?

## 1.2 Context of Study

Carbonate reservoirs with natural fractures are often targeted for geothermal water or hydrocarbons production, especially in case of tight carbonate rocks. Fractures can have a major influence on fluid flow behaviour in reservoirs by enhancing or demolish the rock permeability and/or introducing permeability anisotropy (Nelson, 2001). Therefore, natural fracture modeling has become an important part in reservoir characterization for fluid flow patterns prediction (Laubach et al., 2019).

One of the issues to model natural fractures reservoir is the scarcity of data which provides detailed understanding of the three-dimensional (3D) fracture network characteristics. Another issue is the limitation of the seismic resolution to capture the characteristics of 3D fracture network. High-quality seismic reflection data can characterize and map large structural features such as faults ranging from tens to several hundreds of meters in length. Small-scale features that are below the seismic resolution (e.g. meter scale fractures or joints) can be captured and characterized in one-dimension (1D) using core data and borehole image log. Nevertheless, the small-scale features are confined to the location of the well (Boersma, 2020). Thus, integration of different data sources and scales is required to produce a reasonable fracture network (Rusillon, 2017). Outcrop studies show that characteristics of the

fracture networks can be influenced by the mechanical properties of the rock (Bourne, 2003), regional tectonic regime (Sibson, 1998), and proximity to the faults which causes perturbed stress field (Rawnsley et al., 1992). Taking those factors in consideration is helpful to predict the fracture network.

Considering the limitations to predict subsurface 3D fracture network, optimal characterization of 3D fracture network is still crucial for the development of fractured reservoirs. Consequently, different methods have been developed to model fracture networks. A standard fracture modelling method is performed based on geostatistical analysis of the available fracture data. Another fracture modelling method is based on geomechanical characteristics of the rock by considering the physical laws controlling the fractures creation (Lei et al., 2017). The latter method illustrated high fractures pattern predictability in fractured reservoirs (Welch et al., 2020).

In case of Geneva area, several projects have been completed which were focused on structural, stratigraphic, and petrophysical aspects to understand the subsurface geology of the area (Clerc et al., 2015; Rusillon, 2017; Brentini, 2018). After drilling GGeo-01 well in Geneva Basin, it shows that understanding of the natural fracture in the Mesozoic is important for driving an effective geothermal exploration campaign (Moscariello, 2019). This motivated Lo (2019) to characterize and simulate sub-seismic scale fracture network in the Lower Cretaceous unit in the area around GGeo-01 well. The produced fracture network model was based on a hybrid geomechanics-based stochastic simulation approach. A new approach of 3D fracture network modelling is proposed for geothermal application in this study. This approach is using fracture network forward modelling method that is constrained by geomechanical and fracture data from the well. This approach provides an additional solution of fracture network in the study area.

### 1.3 GGeo-01 program

More attention was brought to the development of geothermal energy resources in Switzerland in the last 10 years. The main driver is to produce electricity in addition to cold/heat water production to cover the demand of both domestic and industrial sectors. To achieve this goal, the Canton of Geneva (CoG) and the local main energy supplier SIG (Services Industriels de Genève) initiated a geothermal energy exploration project '*GGeo-01*' in 2014. This project is considered as the basis for a long term energy strategy which aims to supply geothermal energy to the entire Geneva Canton area through multiple phases (Figure 1.1).

In 2018, GGeo-01 well was drilled as part of the exploration phase of *GGeo-01* program. GGeo-01 has a total depth of 744m below ground floor (bfg) and it penetrated a fractured aquifer that flowed water with high flow rates at 34°C. This aquifer showed that the area around GGeo-01 could potentially be developed for geothermal heat production.

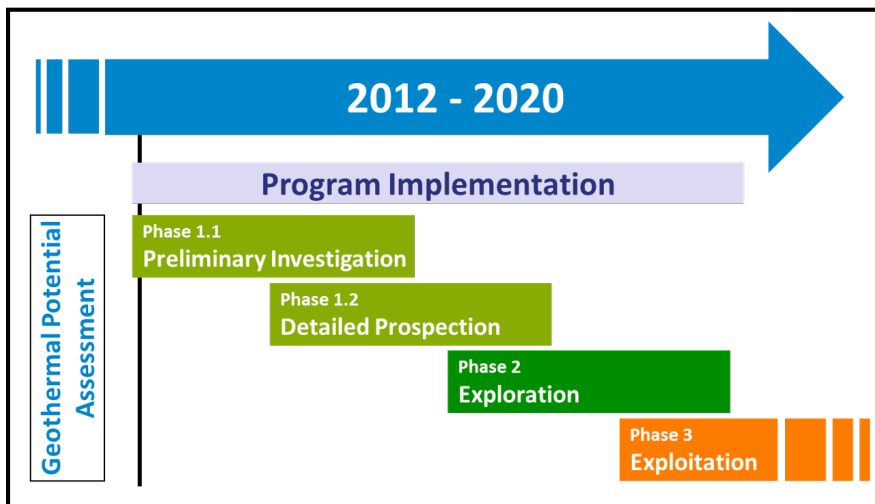


**Figure 1.1:** Implementation plan for *GEothermie 2020* program to assess the geothermal potential in Geneva Basin. (modified after [Moscariello \(2016\)](#))



# Geological Setting

# 2

The Geneva Basin is located in the southwestern part of the Alpine foreland Molasse Basin. The Geneva Basin covers a low relief area of more than  $600 \text{ km}^2$  bounded to the NW by the Jura Mountains, to the SE by the Saleve Mountains, and to the SW by Vuache Mountains (Figure 2.1) (Moscariello et al., 2014; Moscariello, 2021). In this chapter, the stratigraphy framework, tectonic and structural settings, and the aquifer potential will be addressed.

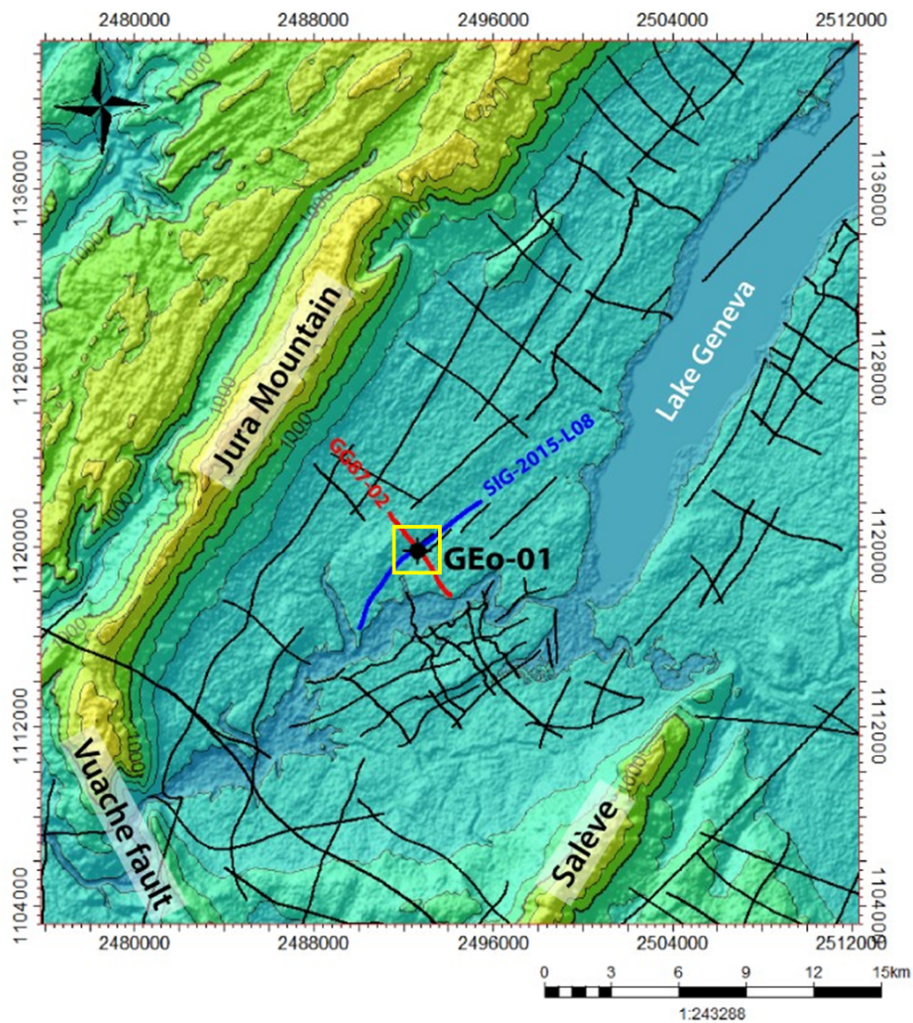


**Figure 2.1:** Location map of the study area showing the  $2 \times 2 \text{ km}$  area of interest (AOI) in the yellow box. It is also showing the GEO-01 well and the two seismic lines that are used in this project. (modified after (Lo, 2019))

## 2.1 Stratigraphy Framework

Geneva Basin sedimentary successions overlie a crystalline basement formed during the Variscan orogeny (Matte, 2001). The Mesozoic and Cenozoic sediments cover 3,000-4,000 m of thickness in Geneva Basin (Figure 2.4). Since this study is focused on the Lower Cretaceous units, this section provides a brief description of the underlying Mesozoic successions followed detailed stratigraphy of the Lower Cretaceous units.

### 2.1.1 Mesozoic

**Triassic:** the Triassic in Geneva Basin includes three main units, Buntsandstein, Muschelkalk, and Keuper. The Buntsandstein consists mainly of continental sandstone. The Muschelkalk is characterized by marine transgressive deposits including dolomite and anhydrite. Finally, the Keuper interval is characterised by dolomite, gypsum, and halite (Brentini, 2018; Clerc et al., 2015).

**Jurassic:** Three units form the Jurassic successions. The Lower unit is characterized by marly carbonates and shale that are interpreted to be deposited during a marine transgression. The Middle unit developed in a relatively deep water environment which resulted in an alternating bioclastic carbonates and mud-dominated facies. The Upper unit represent a regional marine regression that is characterized by shallow platform carbonate deposits containing reef patches (Rusillon, 2017; Moscariello, 2019).

**Cretaceous:** in general, the Cretaceous in Geneva Basin is characterized by a shallow water carbonate environment marked by limestone and marly intervals (Brentini, 2018).

### 2.1.2 Stratigraphy of Lower Cretaceous

The Lower Cretaceous in Swiss Jura Mountains area is divided into 10 formations covering a time interval from the Berriasian to the Barremian (Figure 2.2). Our study focuses on 5 formations described as below from bottom to top, based on the outcome of Strasser et al. (2016):

**Chambotte Fm:** this formation consists of limestone beds that represents high energy shoals and lagoons in a shallow marine environment. The bed thicknesses range from 10s of centimeters to several meters.

**Vuache Fm.:** this formation consists of reddish limestone beds. It shows indications of storm generated structures (hummocky cross-stratification). The facies contain bioclastic and oolitic packstones to grainstones. The thickness of this formation ranges from 10 to 60m.

**Grand Essert Fm.:** this formation consists of two main units. The Marnes d’Hauterive (lower units) shows limestone and marl alternations. It was deposited in an open marine environment under the effect of tidal currents. The Pierre Jaune de Neuchatel (upper unit) is characterised by cross-bedded, bioclastic and oolitic limestone beds. The sedimentary expressions show an indication of strong tidal currents.

**Gorges de l’Orbe Fm.:** this formation is characterised by argillaceous limestone beds (decimeter to meter scale) interbedded with marly thin layers (millimetre to centimeter scale). Gorges de l’Orbe Formation was deposited in a shallow water to deeper open marine environment. This formation thickness ranges from 10 to 30m.

**Vallorbe Fm.:** the lithology of this formation includes limestone beds. Its thickness ranges between 10 and 60m.

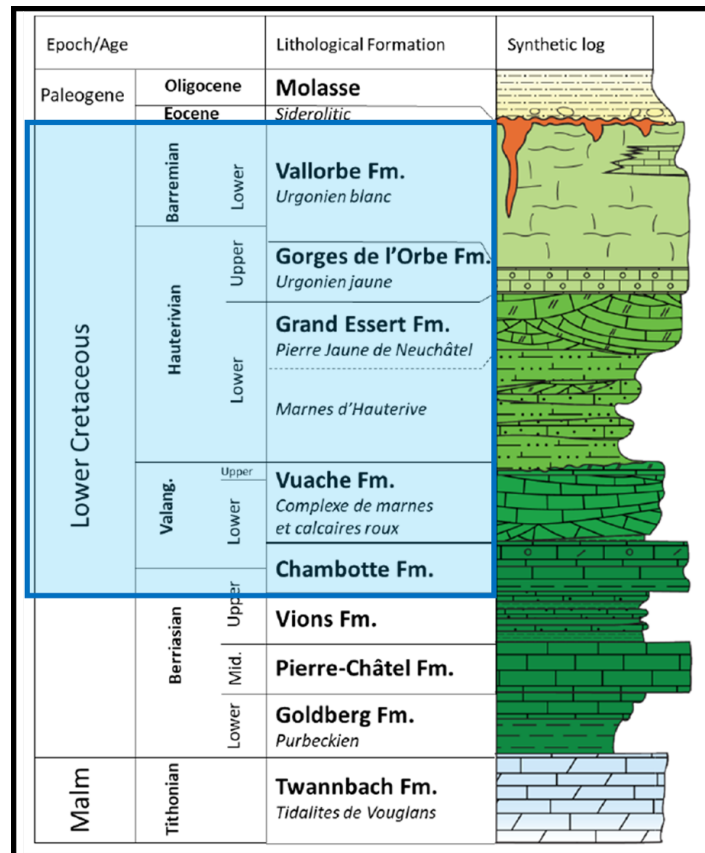


**Figure 2.2:** Stratigraphic column of the subdivisions of the Lower Cretaceous interval that are penetrated by GEo-01 well. The blue box indicated the formations of interest in this study. (modified after Lo (2019); Koumrouyan (2019))

## 2.2 Tectonic and Structural Settings

The main deformation in the area of Geneva Basin resulted from the Alpine orogeny (around 30 Ma) which has a local NW-SE orientation of contraction tectonic that generated thrust planes and anticlinal folds. This contraction tectonic is also accommodated by a series of major NW-SE wrench fault systems (Clerc et al., 2015).

Jura Mountain and the Subalpine units are linked by four major NW-SE wrench fault systems (Clerc et al., 2015). Those faults are called Vuache, the Cruseilles, Le Coin, and the Arve (Figure 2.3). They are cutting through the reliefs of Jura and Salève which suggests they were formed after the formation of the reliefs. As observed in Humilly-2 well, the transpressional movement of those strike-slip faults has led to the creation of flower structures that are cross-cutting the shallow stratigraphy (Moscariello et al., 2014).

A Cenozoic paleo-stress evolution model has been proposed by Homberg et al. (2002) using fault slip data collected from Jura Mountains outcrops. The major identified stages are described as following:

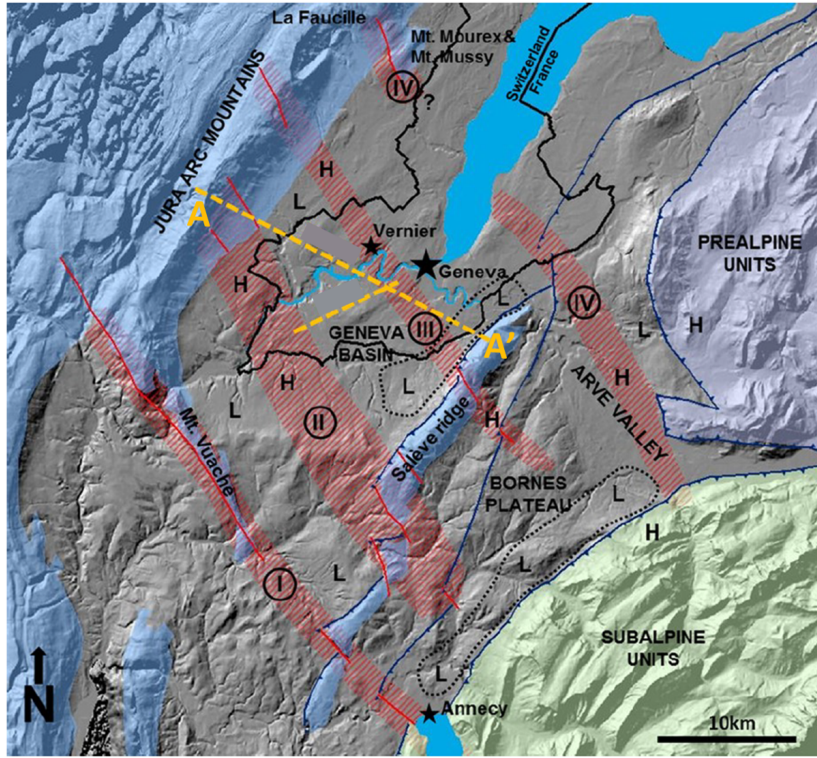


**Figure 2.3:** Structural scheme of the Mesozoic-Cenozoic in Great Geneva Basin that shows two main structural trends. **1)** SW-NE Mesozoic structural lows that are related to the underlying Permo-Carboniferous basins that are located on front thrust of both Subalpine/Prealpine units and Salève ridge. **2)** Four main zones that is influenced by NW-SE trending wrench faults crossing both Bornes Plateau and Geneva Basin. The zones are as following: (I) Vuache; (II) Cruseilles; (III) Le Coin; (IV) Arve (Modified after (Clerc et al., 2015)).

1. **The Eocene Stage (Pyrenean orogeny):** this stage occurred from Early Eocene to Early Oligocene. It is strike-slip N-S compression that resulted in NNE-SSW strike-slip faults.
2. **The Oligocene Stage (West-European rifting):** this stage took place from Early Oligocene to Early Miocene. WNW-ESE extension that resulted in a series of normal faults striking NE-SW to WNW-ESE.
3. **The Miocene Stage:** this stage is a compressional tectonics with a fan-shape stress distribution almost perpendicular to the major thrust axes.

## 2.3 Aquifer Potential

In the Geneva Basin, the Lower Cretaceous interval is considered as a regional aquifer (Clerc et al., 2015). In general, the Lower Cretaceous rock matrix shows poor reservoir quality with porosity ( $\phi$ ) less than 8% and permeability ( $K$ ) ranging between 0.001 and 1mD. The results of the production tests of different wells around the study area illustrate the complexity of the fluid circulation conditions (Moscarriello, 2019). Nevertheless, the fracture networks in the Mesozoic prove their importance to provide enough permeability to the geothermal



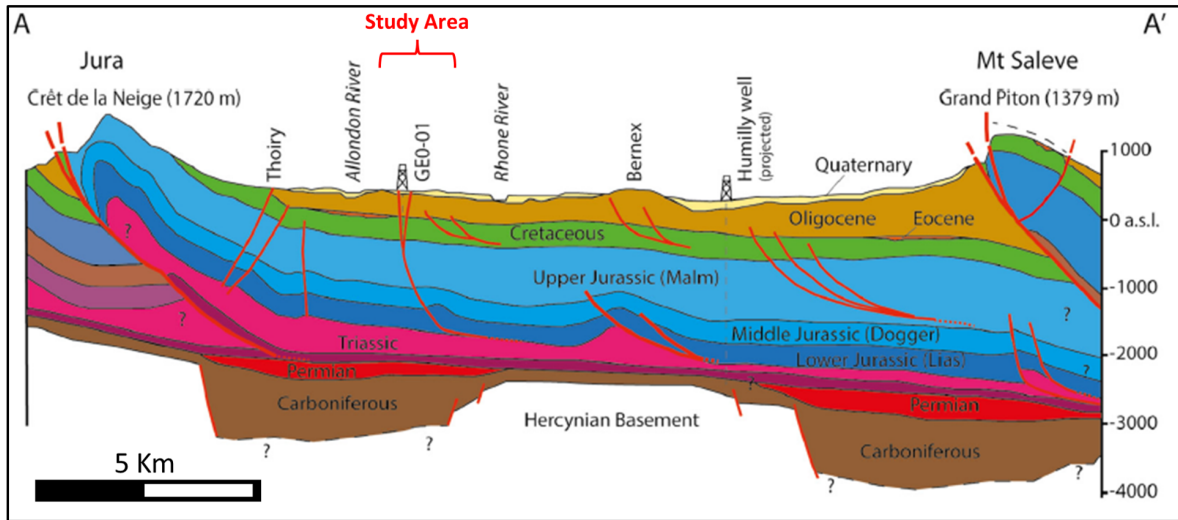


**Figure 2.4:** NW to SE [A to A'] cross-section that illustrates the major stratigraphic units and the key structural elements in Geneva basin based on couple of 2D seismic lines in addition to well data. See Figure 2.3 for the location of the A-A' line projection. (modified after (Moscariello, 2019))

system and to maintain good storage capacity. Géo-01 has penetrated a fractured aquifer that flowed water with high flow rates (50 l/s) at 34°C (Moscariello, 2019). This rate and temperature at this depth is good enough to develop an effective geothermal energy by using the underground heat and indirectly (temperature upgrade by heat pump) injected on the district heating of Canton of Geneva area.

## 2.4 Regional Hydrogeology

In a regional scale, there is no asthenosphere anomalies occurring in the Swiss Plateau where the geothermal process are mainly conduction-dominated (Moeck, 2014). The geothermal source is associated with deep aquifers systems which are heated by near normal heat flow (Chelle-Michou et al., 2017).

In Western Alpine Molasse Basin (WAMB), the average geothermal gradient is around 25–30 °C/km (Figure 2.5 A). Based on several wells in WAMB, the subsurface temperature distribution model highlights a number of positive and negative thermal anomalies which are interpreted in the context of heat advection caused by fluid circulation along faults and/or karst systems (Figure 2.5 B) (Chelle-Michou et al., 2017).

In Geneva Basin, the recharge area of the groundwater is located in the Jura mountain. The meteoritic water infiltrates through the gently south-east dipping Mesozoic sedimentary units. Many sources are present at the foot of the Jura Mountain, however, the circulations of the ground water are still poorly known (SIG, 2018; Koumrouyan, 2019).

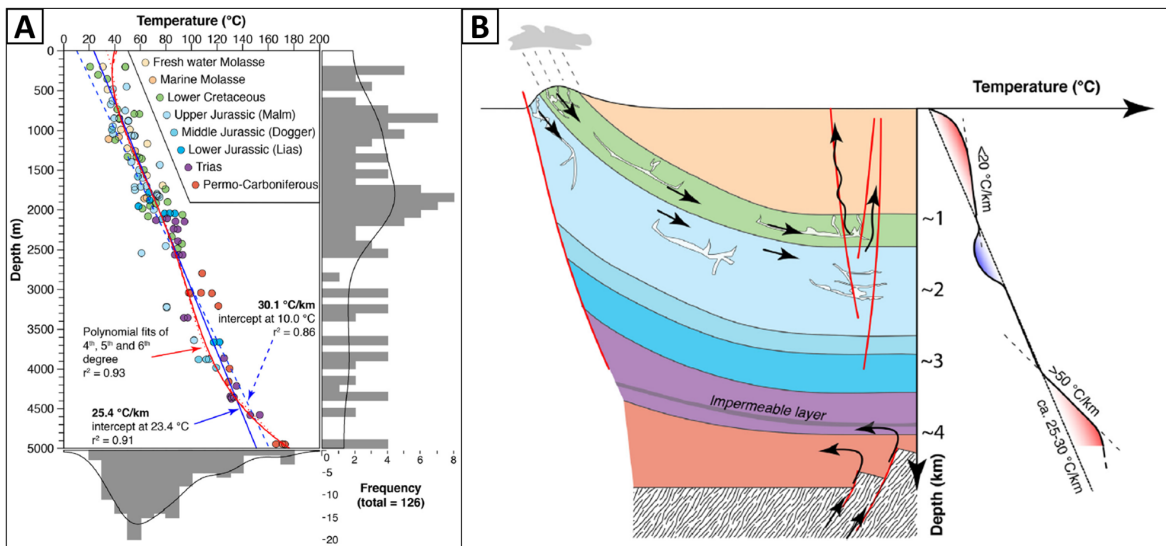


**Figure 2.5:** A) Temperature data in the Western Alpine Molasse Basin (WAMB) and average geothermal gradient (Chelle-Michou et al., 2017). B) Typology of the thermal anomalies identified in the WAMB. Approximate depth is shown for reference but may strongly vary from one place to another (Chelle-Michou et al., 2017).

### 3.1 Seismic Data

In this project, two 2D seismic lines (GG87-02 and SIG-2015-L08) are used to understand the structure of the subsurface of the study area (Figure 3.1). The two seismic reflection profiles are time migrated data. The two profiles are perpendicular to each other oriented NW-SE and NE-SW. They intersect each other almost at the location of GGeo-01 well.

Velocity models (Figure 3.2), a 2D horizons interpretations, a 2D faults interpretation, and 3D fault model were provided by the the Department of Earth Science of the University of Geneva from the provided seismic data, and used as such in the present project.

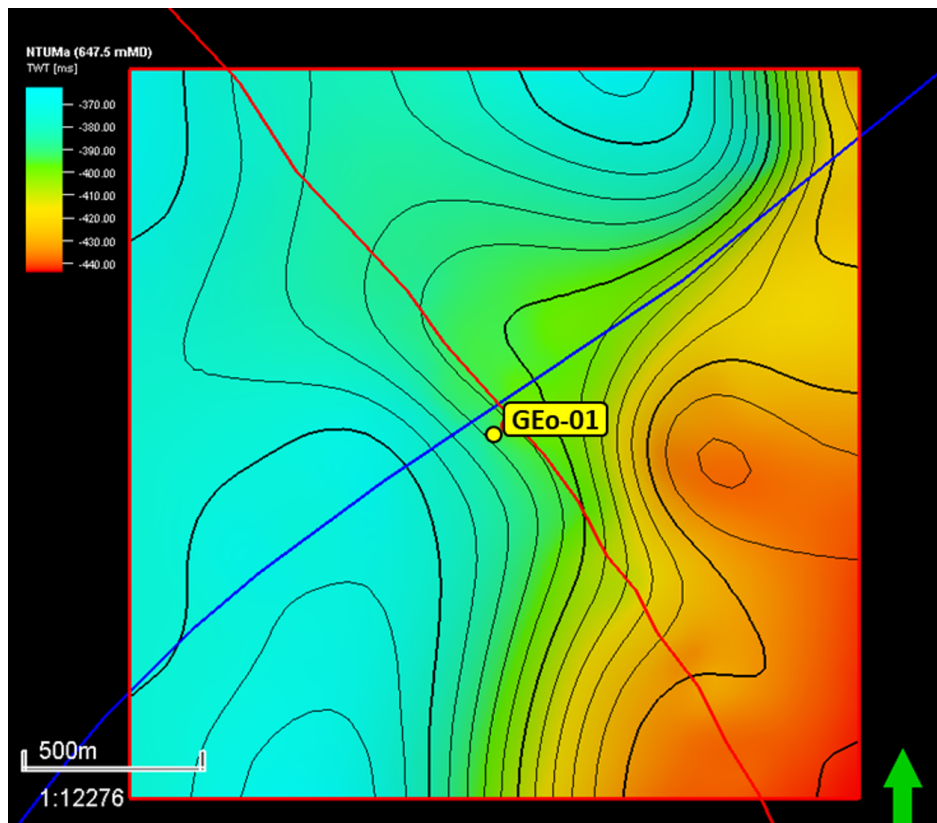


**Figure 3.1:** Top view of the study area with locations of the used two seismic lines in this study, GG87-02 (Red line) and SIG-2015-L08 (Blue line). It also shows the time structural map for the Top of Jurassic horizon.

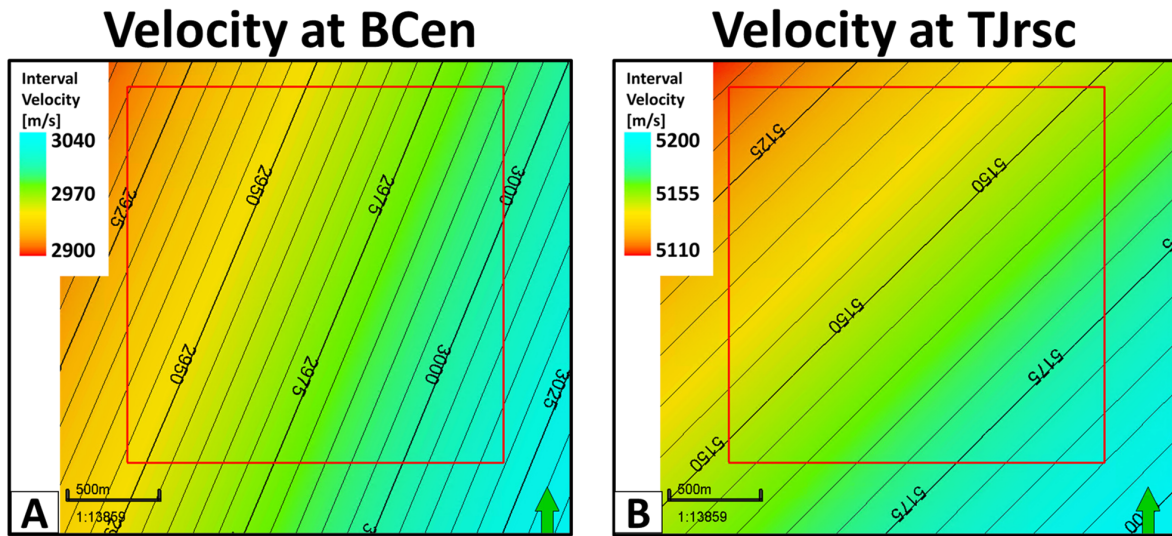


**Figure 3.2:** The provided velocity models along the following two horizons: A) Base of Cenozoic (BCen), and B) Top Jurassic (Tjrsc)

### 3.1.1 Horizons Interpretations

The interpretation of the seismic time horizons for different stratigraphies in the study area have been provided by the the Department of Earth Science of the University of Geneva. The two relevant horizons, which were used for the constuction of the structural model, are the Base of Cenozoic (BCen) and Top Jurassic (Tjrsc) horizons (Figure 3.4). The two horizons correspond to the top and base of the targeted reservoir (see section 5.1.1).

### 3.1.2 Faults Interpretations

Both seismic lines illustrate highly disturbed intervals around GGeo-01 that might be associated to deformation in a fault zone (Lo, 2019). Number of discontinuities are observed which are interpreted as faults with low confidence since only 2D profiles data are available. The objective of the faults' interpretation in this project is to characterize the geometry of the faults and then using them to build a 3D structural model.

Among the two provided seismic lines, the faults discontinuities are visible only on the GG87-02 seismic line. The other seismic line (SIG-2015-L08) does not illustrate the faults as individual discontinuities, instead it shows a zone of highly disturbed units (Figure 3.3).

The 2D faults interpretation was provided only for GG87-02 seismic line, which is oriented NW-SE. The provided 2D fault interpretation shows six faults that are cutting through shallow stratigraphy (Cenozoic) down to the Upper Jurassic (Figure 3.3 A). Three of them are dipping toward the SE and other three are dipping toward the NW. One of the SE dipping fault is extended down to the Triassic and connected to the lower unit of the Triassic interval.

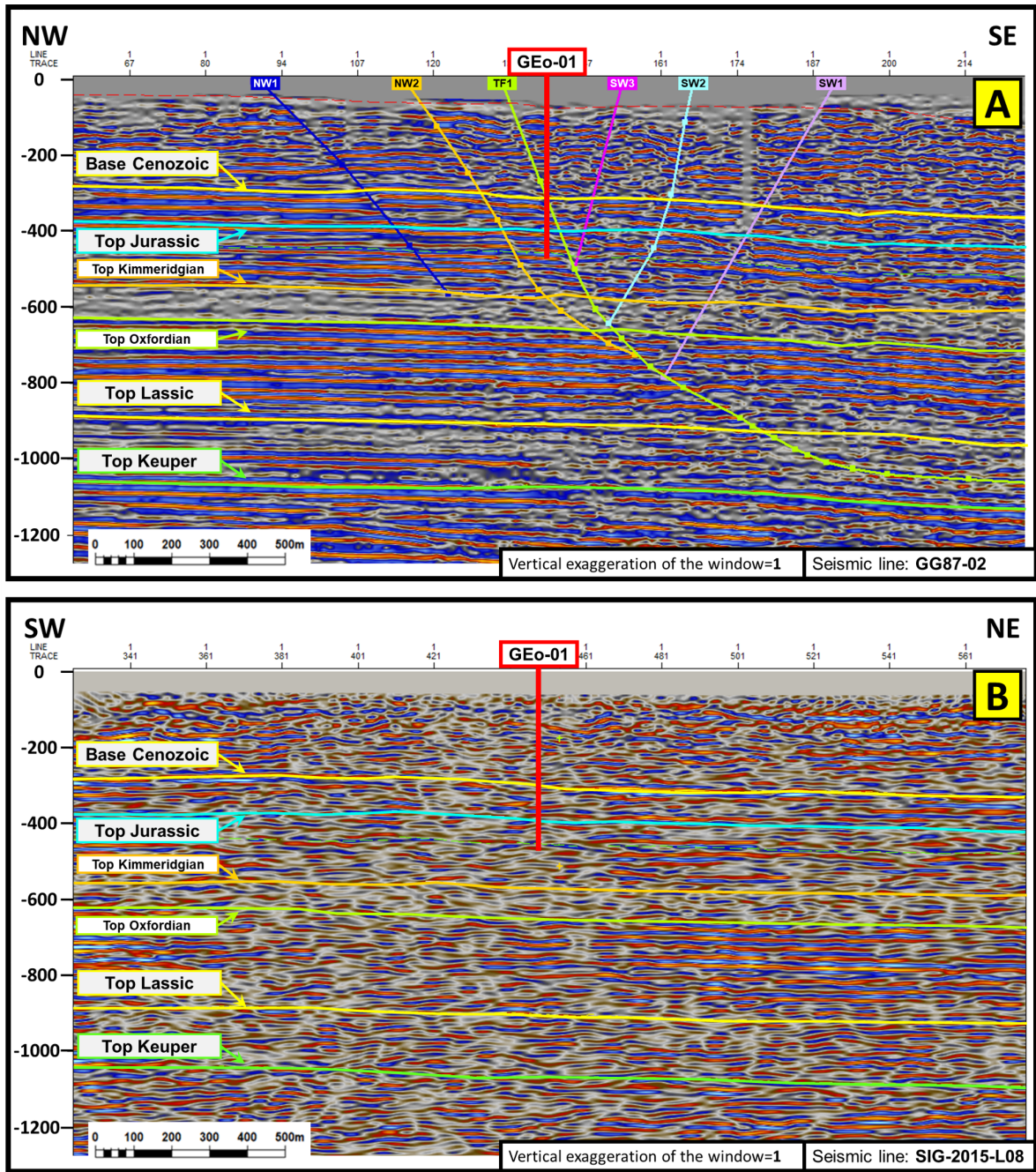


**Figure 3.3:** Two seismic sections show the most of the picked horizons, one of them shows the 2D fault interpretation. **A)** GG87-02 seismic line, **B)** SIG-2015-L08 seismic line. The locations of the seismic lines are shown in Figure 3.1.

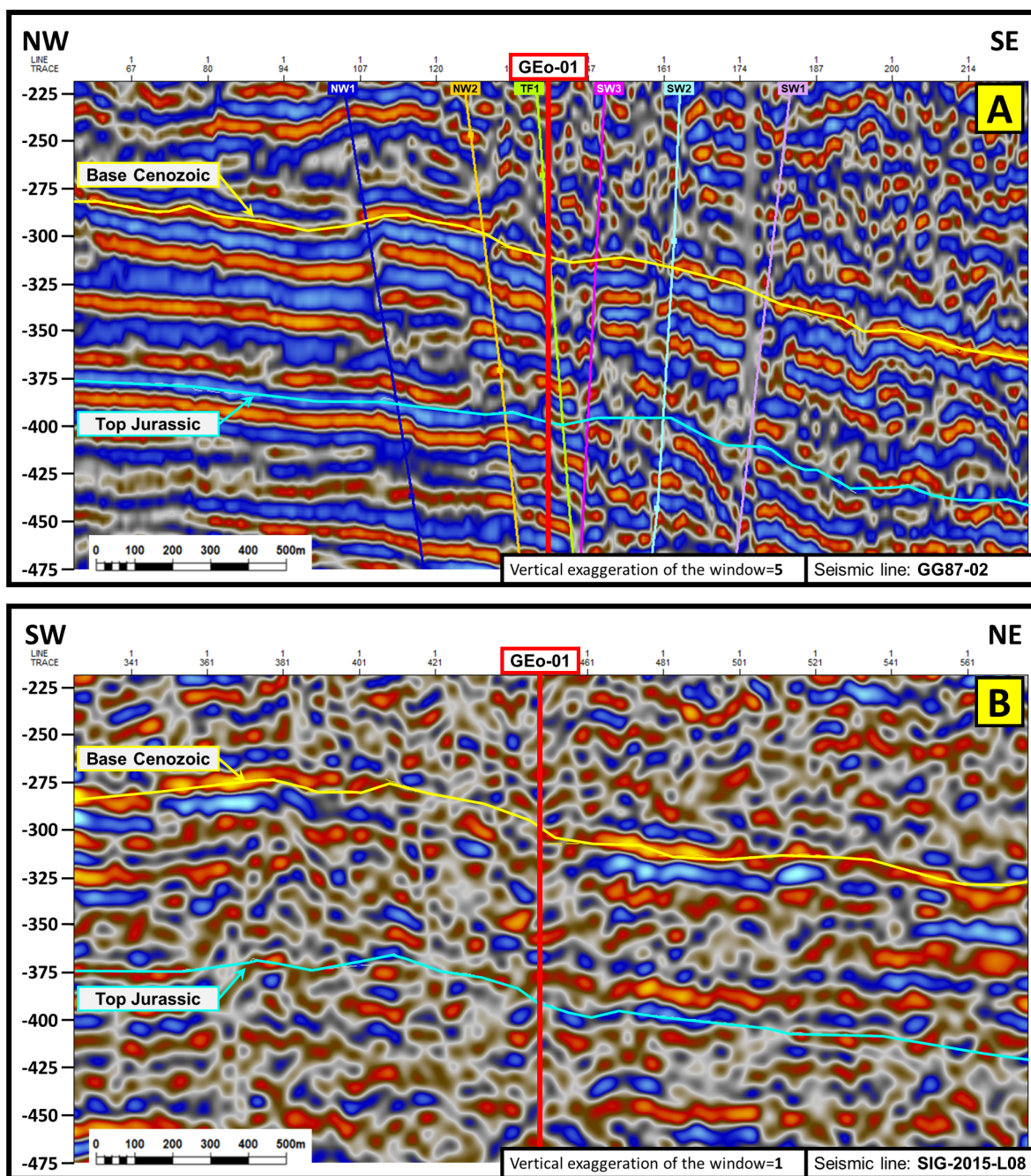


Figure 3.4: Two seismic sections show the two main picked horizons in this study. A) GG87-02 seismic line, B) SIG-2015-L08 seismic line. The locations of the seismic lines are shown in Figure 3.1.

## 3.2 Borehole Data

### 3.2.1 GEO-01 well

GEO-01 is a medium depth geothermal exploration well that was drilled in Satigny, Geneva in 2017. It penetrated through the Lower Cretaceous units and reached the top of the Upper Jurassic with a total depth of 744m bgf. It went through a fractured aquifer that flowed water with high flow rates (50 l/s) at 34°C (Moscariello, 2019). The main objective of this well was to penetrate the fractured carbonate of the Lower Cretaceous units and to cross a naturally karstified layers to increase the probability of the water flow (Koumrouyan, 2019).

**Table 3.1:** GEO-01 well information Lo (2019).

Well	GEO-01
Project	GEothermie 2020
Company	Services Industriels de Genève (SIG)
Drilling contractor	Hydroforage
Logging contractor	SEMM Logging
Country	Switzerland
Canton	Geneva
Address	Route de Satigny, 1247 Satigny
Surface coordinates (CH1903+/LV95)	X : 2, 492, 617 m Y : 1, 119, 863 m
Datum for elevation	Mean sea level
Measurement ref.	Ground level (413.84 m a.s.l.)
Total depth	744.06 mMD
Start date of drilling	23/10/2017

### 3.2.2 Petrophysical Logs

The logging program of GEO-01 well included both images and petrophysical logs (Table 3.2). No logging data were acquired below the depth of 533 mMD due to the unstable wellbore condition.

Petrophysical logs in GEO-01 well were acquired from 15 to 533 mMD. The logs acquisition covers the Lower Cretaceous units which include Gamma Ray, caliper, resistivity (deep and shallow), P-sonic, bulk density, and neutron-porosity (Figure 3.5). The well tops of the Lower Cretaceous units were picked using different well logs (Table 3.3).

**Table 3.2:** GEO-01 well logging details Lo (2019).

Date of logging	14 – 15/12/2017	5 – 6/2/2018	21 – 23/3/2018
No. of runs	4	6	9
Logged interval	14.48 – 336.03 mMD	340 – 409.67 mMD	413 – 533 mMD
Casing-Driller	20" @ 15.5mMD	133/8" @ 338mMD	95/8" @ 411mMD
Bite Size	17.5in	12.25in	8.5in
Fluid type	Mud (Bentonite)	Mud (Bentonite)	Water
Bottom Hole Temp.	24°C	26°C	32.5°C

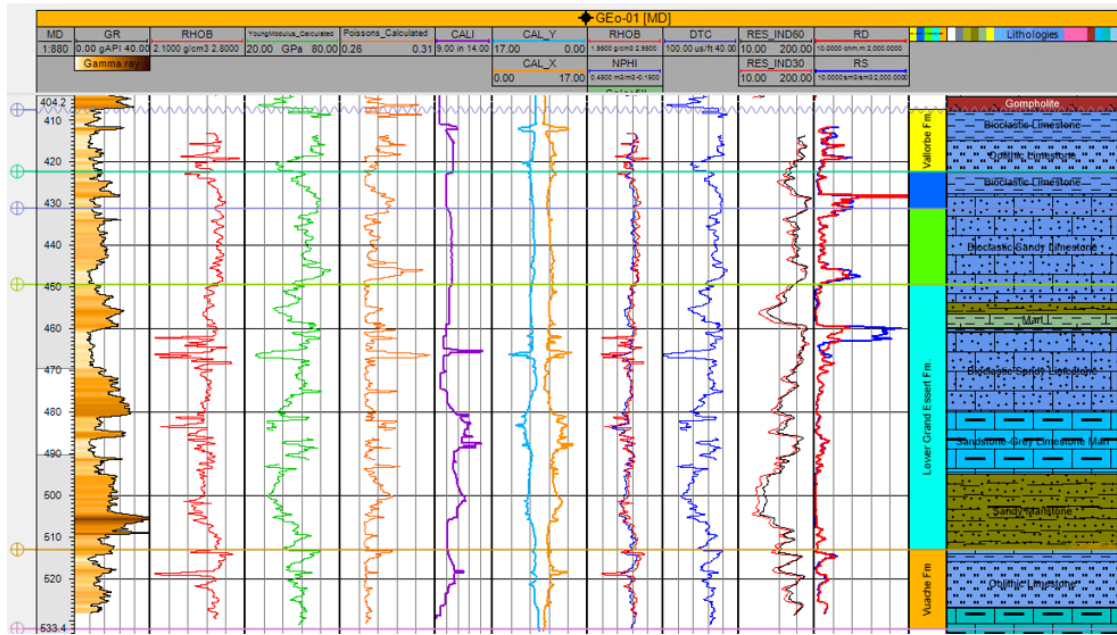


**Figure 3.5:** The acquired geophysical logs in addition to some calculated logs (Young’s Modulus and Poisson ratio) and described lithology.

**Table 3.3:** Lower Cretaceous formation tops in GEO-01 well.

Formation	TVDSS [m]	MD [m]
Vallorbe Fm.	6.5	407.5
Gorges de l’Orbe Fm.	-8.3	422.3
Upper Grand Essert Fm.	-17.11	431.11
Lower Grand Essert Fm.	-35.38	449.38
Vuache Fm.	-99	513
Chambotte Fm.	-118	532

### 3.2.3 Fracture Data

An Optical Borehole Imager (OBI) and Acoustic Borehole Imager (ABI) were acquired from 413 to 533 mMD. The image logs were analysed and fractures were picked (Koumrouyan, 2019; Lo, 2019). The picked fracture data were used in the present project. The provided data contain 212 fractures in the Lower Cretaceous interval in GEO-01 well. The fracture data include depth, dip azimuth, and dip angle for each fracture.

The fractures were plotted as poles. These poles were contoured to highlight densities in the dataset. They are also presented in form of rose diagram of the fracture strike (Figure 3.6). Furthermore, the fractures’ dip azimuth and dip angle are presented in a well log across the Lower Cretaceous interval (Figure 3.7).

Fracture classification with respect to their mechanical type is performed by Lo (2019). The proper fracture classification is usually done by describing cores or outcrops. However, Lo has performed indirect classification of the observed fractures in BHI using some diagnostic characteristic that have been suggested for certain fracture types (Figure 3.8) (e.g. Trice, 1999).



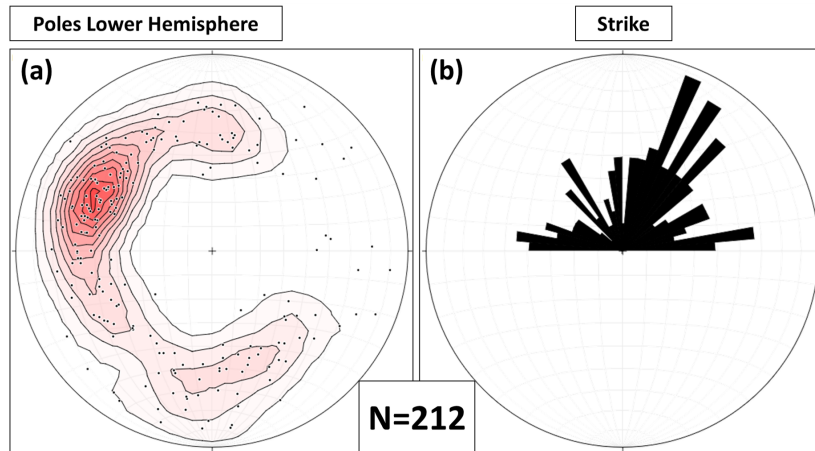


**Figure 3.6:** (a) (lower hemisphere) illustrating pole of each measurement and pole density of true dip orientation of the full fractures data. (b) Rose diagram representing the strike of the full fractures data.

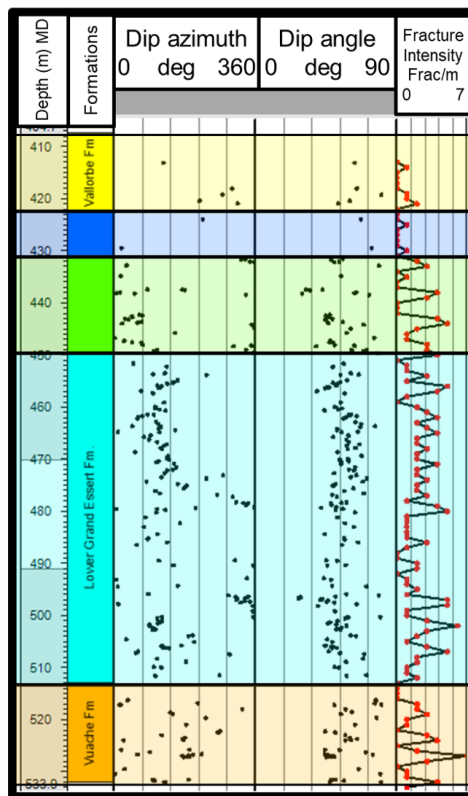


**Figure 3.7:** Dip azimuth, Dip angle, and fracture intensity along the depth in the Lower Cretaceous interval in GEO-01 well.

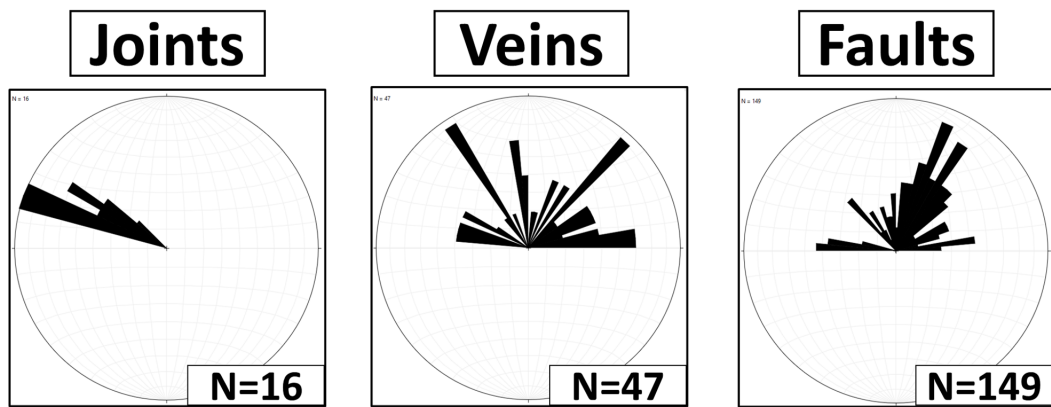


**Figure 3.8:** Rose diagrams representing the strike of the fractures in different groups based on their mechanical types.

# Methodology of Preparing the Data and Creating DFN Model

# 4

## 4.1 General Workflow Chart for DFN Creation

The workflow of the fracture modelling in this project utilizes two tools, tectonic inversion tool and fracture network forward modelling tool (DFN Generator). The inputs of the tectonic inversion tool are the horizon from the constructed 3D grid model, fault model, mechanically classified fracture data, and tectonic stress configuration. This tool shows the fitting between the observed fracture geometry from the well and different stress configurations. It also produces distribution of strain tensors. The main inputs of the DFN Generator tool are minimum horizontal strain rate, maximum horizontal strain rate, azimuth of the minimum horizontal strain, different elastic and mechanical properties, and stress states parameters. This tool produces fracture network (Figure 4.1).

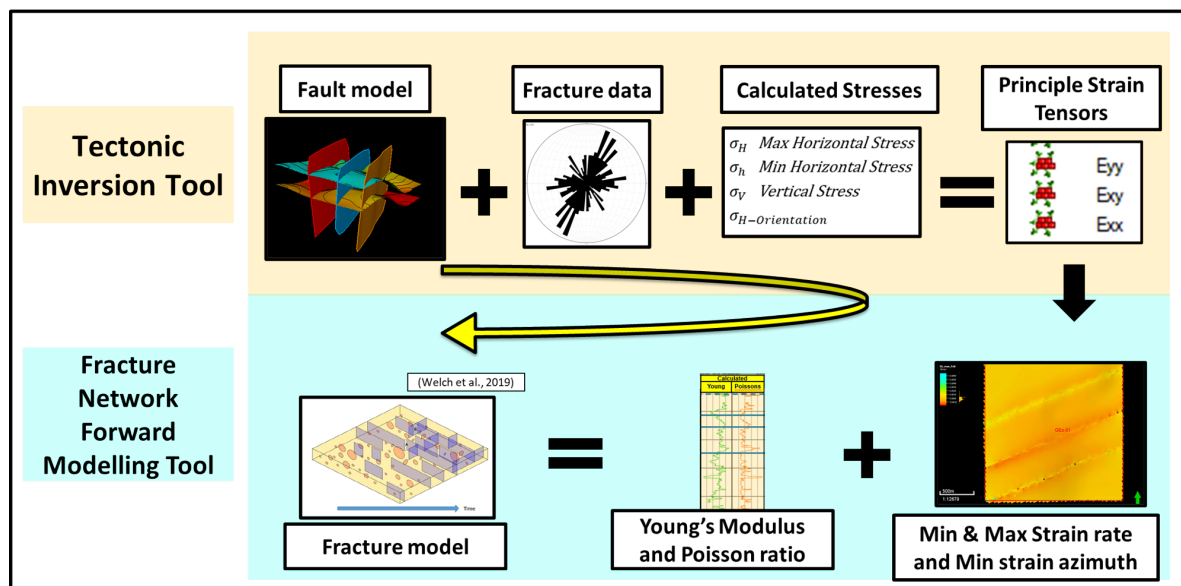


Figure 4.1: The workflow for the fracture network modelling in this project.

## 4.2 Structural Model

Three structural models were provided by the Department of Earth Science of the University of Geneva. All the horizons are the same in all the provided models. However, each model has different faults configuration. In this project, only one model was considered. The orientation of the faults were chosen to have a strike of N068°. For technical reasons, the model was re-created in this project.

### 4.2.1 modelling grid

The Base of Cenozoic and Top Jurassic horizon interpretations in the TWTT seismic profiles are extrapolated within the 2x2 km study area to generate two time surfaces. The two time surfaces were converted to depth surfaces using the provided velocity model. The depth surfaces were shifted vertically to tie with the corresponding well tops in GGeo-01.

### 4.2.2 Fault Model

The provided 2D fault interpretation are basically traces on the TWTT seismic profile. The fault traces were converted to depth domain using the provided velocity model. The depth fault traces were extended laterally in three dimensional space with a chosen strike direction.

## 4.3 Geomechanical Properties Calculations

### 4.3.1 Properties Calculation Method

In this study, we had to calculate the Young's Modulus and Poisson's Ratio logs to perform rock's geomechanical analysis. Empirical relations and some of measured logs have been used to calculate Young's Modulus and Poisson's Ratio logs.

#### 4.3.1.1 Young's Modulus $E$

Some of the rock mechanical properties such as Young's modulus can be obtained using P-wave velocity. Empirical relations that relate the P-wave velocity with the Young's modulus ( $E$ ) and with density ( $\rho$ ) are determined by [Yasar and Erdogan \(2004\)](#). these empirical relations are obtained using the laboratory test result of carbonate rock's mechanical properties. The empirical relations that relate the Sound Velocity (SV) with the Young's modulus and with density are shown in Equation 4.1 & Equation 4.2, respectively

$$E = (SV - 1.7528)/0.0937 \quad (4.1)$$

$$SV = 4.3183\rho - 7.5071 \quad (4.2)$$

#### 4.3.1.2 Poisson's Ratio

Similar to the Young's modulus calculation, an empirical relationship between P-wave velocity ( $V_P$ ) and Poisson's ratio was used to calculate the Poisson's ratio log. [Kenter et al. \(2007\)](#) used Poisson's ratio measurements and  $V_P$  from different rock types to derive Poisson's ratio from  $V_P$  values. Relatively to the nature of the rock of the targeted interval, we focused on carbonate data densities and  $V_P$  (Figure 4.2 blue zone). Equation 4.3 represents the fit curve in the middle of the carbonate density area.

$$Poisson's\ ratio = 0.0126(V_P)^2 - 0.1174V_P + 0.5464 \quad (4.3)$$

where  $V_P$  is the P-wave velocity. Simply, the measured P-sonic log in GGeo-01 was used in Equation 4.3 to calculate the Poisson's ratio log.

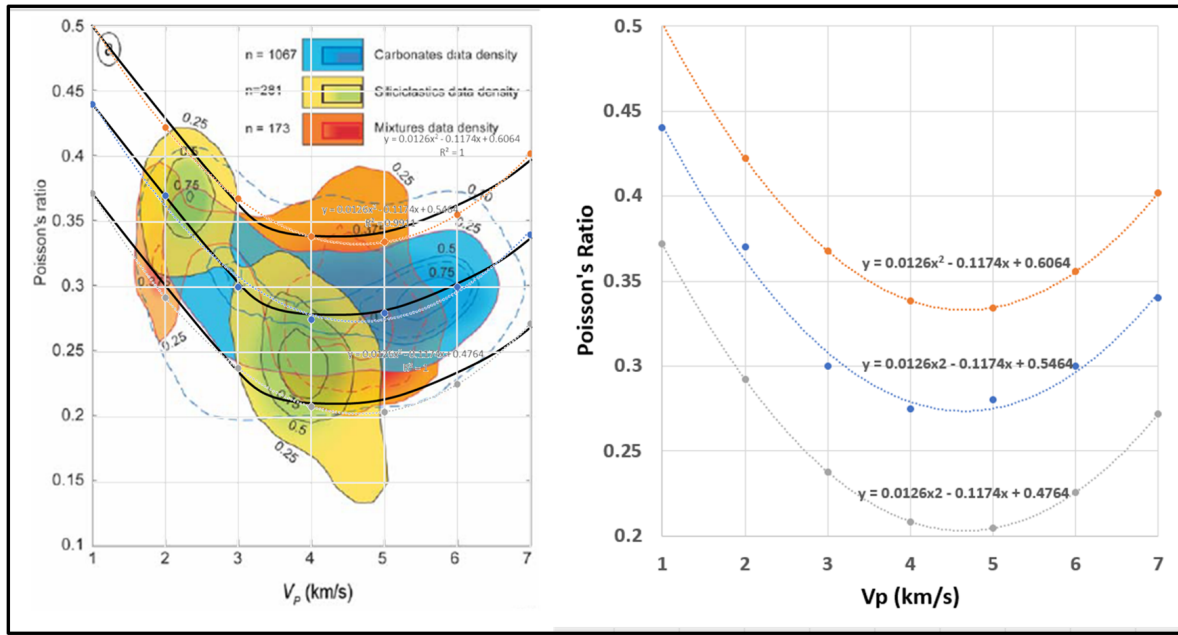


**Figure 4.2:** Left: A cross-plot of P-wave velocity with Poisson's ratio. Right: the best fit lines for the upper limit, lower limit and the middle curves of the carbonate data. (modified after (Kenter et al., 2007))

### 4.3.2 Rock Stiffness Partitioning Approach

Analysing the rock's stiffness in different layers is an important process since it influence the modelling of the fracture network. Young's modulus values can give an indication about the rock's stiffness. Stiffer rocks such as limestone and dolomite are indicated by relatively high Young's modulus values (50-60 GPa). Whereas softer rocks such as sandstone or marls are indicated by lower Young's modulus values (35-45 GPa) (Gudmundsson, 2011). Moreover, Gamma ray log can give an indication about the shale content in the rock where high Gamma ray values correspond to more shale content and vice versa (Schlumberger, 1991).

The approach of the rock's stiffness analysis is based on the behaviour of both Gamma ray and Young's modulus logs. The criteria to perform the rock's stiffness analysis is described as following:

- Rocks that are characterised by high Gamma ray and low Young's modulus values are interpreted to have higher shale content and correspond to **soft rock group**.
- Rocks that are characterised by low Gamma ray and high Young's modulus values are interpreted to have low shale content and correspond to **stiff rock group**.

The average value of the log across the Lower Cretaceous formations in GGeo-01 defines the cutoff value. This applies to both Gamma ray and Young's modulus cutoffs. The log is considered high when its values are higher than the cutoff and vice versa.

## 4.4 Fracture Data Analysis

The analysis of the fracture data in GEO-01 well consists of two stages. In the first stage, the full fracture data is analysed as one set. The dip angle and dip azimuth of the fracture data were analysed along the full interval of fracture data. The pattern of the fractures' poles in the stereonet was also analysed. The fracture pattern analysis was used to interpret the principal stress configuration at the time of the fracture formation.

In the second stage, the fracture data was partitioned into different groups based on different stratigraphic formations, different rock stiffness layer, and different lithologies. The behaviour of the fracture groups was analysed and possible explanations of the observed behaviour were provided.

## 4.5 Paleo-tectonic Stress Inversion Technique

In this study, the paleo-tectonic stress inversion tool is used mainly to estimate the fracture related paleo-tectonic stress and to produce the distribution of the principal stress and strain tensors.

### 4.5.1 Methodology

It is possible to measure the distribution and magnitude of the present-day stress of a certain area. However, obtaining the magnitude and orientation of the stress at the time of fracture generation (paleo stresses) represents a considerable challenge. Maerten et al. (2016) have developed a paleo-tectonic stress tool that is using iBem3D technology.

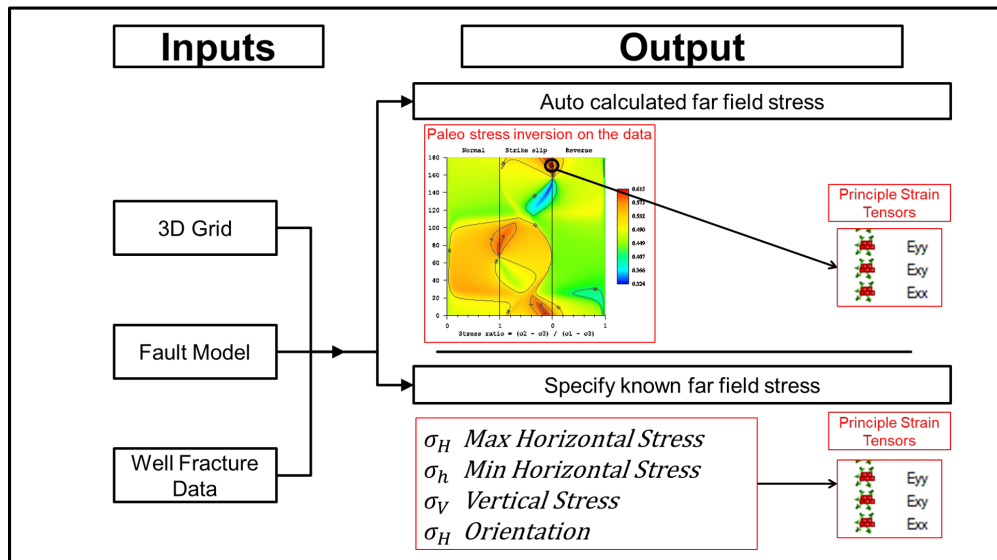


**Figure 4.3:** Work flow of the Paleo-tectonic Stress Inversion Technique.

The main inputs in this tool are horizon from the constructed 3D grid model, fault model, and the observed fracture data from the well (Figure 4.3). Thousands of simulations are performed where all possible configurations of orientation and relative magnitude of tectonic stress are covered. The modelled stresses in each simulation is compared with the geometry

of the observed fracture data. In each simulation the cost is calculated which represents the match between the observed fractures geometries and local computed stresses. The cost value ranges from 0 to 1 where 0 means a perfect match and 1 means the worst match. The simulation that results in the best fit between the modelled stress and the observed fracture geometry (lowest cost) is considered as the optimum tectonic stress regime (Figure 4.4). The tool records several outputs that are associated to the best fit simulation. The main outputs that are used in this study are the distribution of the principal strain tensors ( $\varepsilon_{xx}$ ,  $\varepsilon_{yy}$ , and  $\varepsilon_{xy}$ ).

In case if the far-field stresses are known, the tool provides an option to utilize them as inputs. In this option, the produced principle strain tensors are associated to the known far-field stresses.

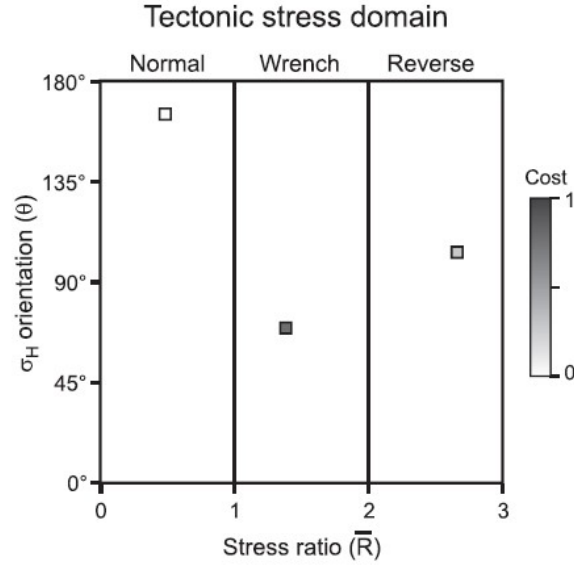


**Figure 4.4:** Example of a tectonic stress domain. The x-axis is the stress ratio, and the y-axis is the orientation,  $\theta$ , of the maximum horizontal stress relative to north. A point in the domain represents one simulation that is coloured with respect to the computed cost which varies between 0 and 1 (Maerten et al., 2016).

The input stresses can be calculated using the following Equations 4.4, 4.5, and 4.6 (Higgins-Borchardt et al., 2016).

$$\sigma'_V = (zg\rho_{Rock}) - (zg\rho_{Fluid}) \quad (4.4)$$

where  $\sigma'_V$  is the effective vertical stress [ $Pa$ ],  $z$  is the model depth [ $m$ ],  $g$  is the gravity acceleration [ $m/S^2$ ],  $\rho_{Rock}$  and  $\rho_{Fluid}$  are the rock and fluid densities [ $kg/m^3$ ], respectively.

$$\sigma'_{Hmax} = \frac{\nu}{1-\nu}\sigma'_V + \frac{E}{1-\nu^2}\varepsilon_{Hmax} + \nu\frac{E}{1-\nu^2}\varepsilon_{hmin} \quad (4.5)$$

$$\sigma'_{hmin} = \frac{\nu}{1-\nu}\sigma'_V + \nu\frac{E}{1-\nu^2}\varepsilon_{Hmax} + \frac{E}{1-\nu^2}\varepsilon_{hmin} \quad (4.6)$$

where  $\sigma'_{hmin}$  and  $\sigma'_{Hmax}$  are the minimum and maximum effective horizontal stresses [ $Pa$ ], respectively,  $\varepsilon_{hmin}$  and  $\varepsilon_{Hmax}$  are the minimum and maximum principal horizontal strain,  $E$

is the Young's modulus [ $Pa$ ], and  $\nu$  is the Poisson's ratio

#### 4.5.2 Boundary Conditions

To estimate the paleo-tectonic stress for the geomechanical simulations, two main assumption are made:

1. The computed far-field stress configuration is obtained under the consideration of the input fractures to be associated with perturbed stress field of the pre-existing faults.
2. The geometry of the natural fractures are influenced by the far field tectonic stress in addition to the perturbed stress field around the active large faults.

#### 4.5.3 Assumption of Strain Rate and Strain Value

According to [Welch et al. \(2019\)](#), the mean strain rates across active rift basins are typically of the order of  $1.00E-3$  to  $1.00E-2 Ma^{-1}$ . Furthermore, the time period of an extensional strain can typically last for 10s of millions of years ([Welch et al., 2019](#)). However, the fracture network is often formed early in the deformation episode (e.g. 100s of thousands of years) ([Welch et al., 2020](#)). In this project, the fracture formation time period was arbitrarily set up to  $1 Ma$ . Moreover, the horizontal strain is assumed to be uniaxial ((i.e.  $\varepsilon_{h\min} < 0, \varepsilon_{h\max} = 0$ )). Over a time period of  $1 Ma$ , the total accumulated horizontal strain is assumed to be  $3.00E - 3$  with a minimum strain rate of  $3.00E-3 Ma^{-1}$ .

#### 4.5.4 Technique Limitations

- The output of this tool is very sensitive to the fault model geometry. Any change to the fault lateral extension or fault height will result in a major change in the model outputs.
- This technique does not provide an option to control the rock geomechanical properties. It assumes a homogeneous elastic rock properties where the default value for Young's modulus is  $30 GPa$  and for Poisson's ratio is  $0.25$ . The default values are fairly close to the used geomechanical properties values in this study.
- This technique does not offer a control over the amount of the fault slip. The faults are slipping freely in response to the remote load. The amount of displacement that are caused by the faults' slip is found to be associated with the size of the faults. Larger faults result in larger amount of displacement and vice versa.
- The algorithm of the inversion ignores the effect of fractures. It assumes that the rock remain intact and behaves as a continuum elastic body. In reality, fractures will start to accommodate some of the strain and reduce the elastic strain in the rock mass. To compensate for this limitation, the input principal horizontal strain values in the stresses calculations (Equations 4.5 & 4.5) are scaled down.



## 4.6 Fracture Forward Modelling Approach

In this approach, a DFN Generator (plug-in in Petrel 2018) is used (Welch et al., 2019). The tool models fracture growth (4D modelling) of layer bound fracture network. This approach considers the growth and the interaction of the layer bound fractures to be a response to an externally applied horizontal strain. Using the DFN Generator provides an alternative fracture network model to other DFN modelling tools (such as stochastic DFN modelling approach (Lei et al., 2017)).

### 4.6.1 Methodology

The DFN Generator considers a single homogeneous and brittle layer surrounded by a ductile layers. The brittle layer is assumed to be perfectly elastic material where the applied horizontal strain can be accommodated either by elastic displacement on the fractures or elastic strain in the host rock. The principal stresses and strains are always considered to be coaxial (Welch et al., 2020).

The brittle layer contains initially population of small circular 'microfractures' that are randomly distributed within the brittle layer following the power-law size distribution which is given in Equation 4.7.

$$P_{30}(r) = Br^{-c} \quad (4.7)$$

where  $P_{30}(r)$  represents the number of fractures of size  $r$  or greater per unit volume,  $B$  is a fracture density coefficient, and  $c$  is a power-law exponent. Those microfractures are striking perpendicular to the horizontal principal strains. The layer is initially under a constant vertical effective stress  $\sigma'_v$  and an initial isotropic horizontal effective stress  $\sigma'_{h0}$ . The initial horizontal stress can be in viscoelastic equilibrium with the vertical effective stress (i.e.  $\sigma'_{h0} = \sigma'_v$ ) or in elastic equilibrium (i.e.  $\sigma'_{h0} = v/(1-v)\sigma'_v$ ). A constant horizontal extensional strain is applied to the modelling layer. The horizontal strain can be either uniaxial (i.e.  $\varepsilon_{h\min} < 0, \varepsilon_{h\max} = 0$ ) or biaxial ( $\varepsilon_{h\min} \neq \varepsilon_{h\max} \neq 0$ ). The applied horizontal extensional strain decreases the horizontal effective stress while the vertical effective stress remains constant.

At the beginning of the modelling, the circular microfractures will start to grow while maintaining their shape. the microfractures continue to grow until they reach the top and bottom of the layer where they will stop growing vertically and continue growing horizontally along the layer. At this stage, the fracture will become as rectangular planes that are called layer-bound 'macrofracture' (Figure 4.5). During the propagation of the fractures, the stress around them decreases locally due to the fracture displacement. The zone where the stress is decreasing is called 'Stress Shadow Zone'. Bai and Pollard (2000) and Bai et al. (2000) showed that in outcrops, the spacing of fractures is typically proportional to the layer thickness. They attributed this relation to the stress shadow effect. In the DFN Generator tool, the stress shadow zone is defined as a rectangular box with a width (on both sides of the fracture) equal to twice the layer thickness. Moreover, in thick layers, fracture network will have low fracture intensity whereas in thin layers it will have higher fracture intensity. For simplicity, the horizontal elastic strain in the rock mass is assumed to be zero within the stress shadow zone. The two tips of the macrofractures continue growing in both direction at equal rate until they either:

1. reach a mechanical barrier to propagation (e.g. intersect perpendicularly with another macrofracture); or

2. the driving stress changes (e.g. propagate into another parallel macrofracture's stress-shadow zone).

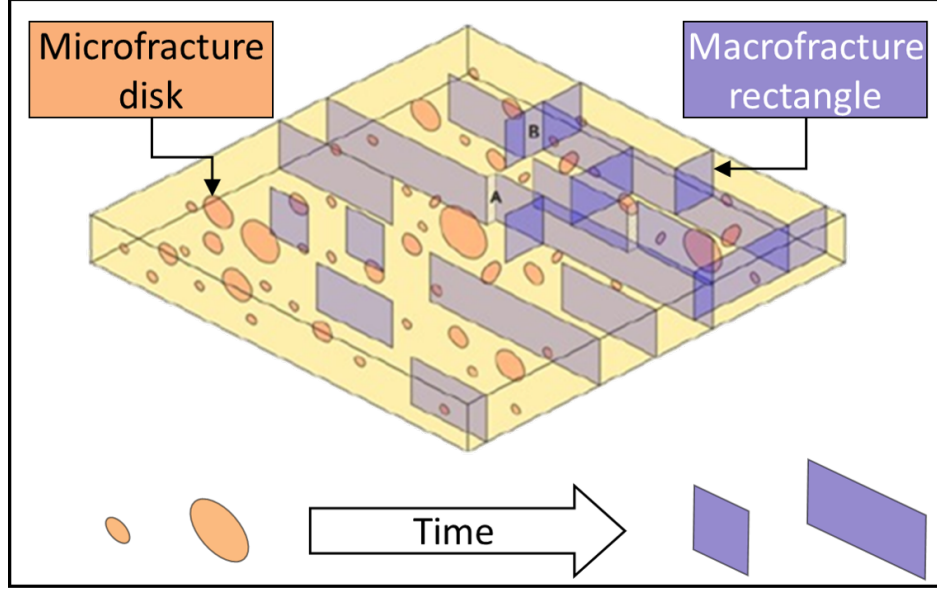


**Figure 4.5:** Simplified explanation of the process of fracture nucleation, propagation, and interaction in DFN Generator tool. Going from left to right, the figure illustrates the fracture formation process through time. The red circles are initial microfractures and blue rectangular are the layer-bound fractures. (modified after [Welch et al. \(2019\)](#))

DFN Generator allows for many inputs regarding the different parameters for mechanical properties and stress state. The most important inputs are the constructed 3D grid, Young's modulus, Poisson's ratio, azimuth of minimum horizontal strain [deg], minimum horizontal strain rate [/ma], and maximum horizontal strain rate [/ma].

The azimuth of minimum horizontal strain ( $\theta$ ), the minimum horizontal strain ( $\varepsilon_{hmin}$ ), and the maximum horizontal strain ( $\varepsilon_{hmax}$ ) are calculated using the the principal strain tensors outputs of the paleo-tectonic stress inversion tool ( $\varepsilon_{xx}$ ,  $\varepsilon_{yy}$ , and  $\varepsilon_{xy}$ ) using Equations 4.8, 4.9, and 4.10 ([Roylance, 2001](#)).

$$\theta = \left[ \tan^{-1} \left( \frac{2\varepsilon_{xy}}{\varepsilon_{yy} - \varepsilon_{xx}} \right) \right] / 2 \quad (4.8)$$

$$\varepsilon_{hmin} = \varepsilon_{xx} \sin^2 \theta + \varepsilon_{yy} \cos^2 \theta + 2\varepsilon_{xy} \sin \theta \cos \theta \quad (4.9)$$

$$\varepsilon_{hmax} = \varepsilon_{yy} \sin^2 \theta + \varepsilon_{xx} \cos^2 \theta - 2\varepsilon_{xy} \sin \theta \cos \theta \quad (4.10)$$

By knowing the time period (' $t$ ' in million years [Ma]) of the fracture formation, the minimum and maximum horizontal strain rate can be calculated using Equations 4.11 and 4.12.

$$\text{Min Horizontal Strain Rate [Ma]} = \varepsilon_{hmin}/t \quad (4.11)$$

$$\text{Max Horizontal Strain Rate [Ma]} = \varepsilon_{hmax}/t \quad (4.12)$$

It worth mentioning that when input the azimuth of minimum horizontal strain ( $\theta$ ) into the DFN generator tool in Petrel 2018, it has to be converted from degree to radian.

#### **4.6.2 Boundary Conditions and Tool Limitations**

In order to run the DFN Generator to estimate the fracture network, few boundary conditions and limitations have to be considered:

1. The modelling tool assumes only layer-bound fractures. So, it is not possible for this modelling approach to model a fracture that propagates through multiple layers.
2. The applied horizontal extensional strain rate can only be constant. This is considered as a tool limitation since it does not provide an option to change the strain rate during the fractures propagation.
3. fracture propagation will stop when intersecting a perpendicular macrofracture or enters a stress shadow zone of another parallel fracture. The final fracture network will never include a crossing fractures.



## 5.1 Results and Interpretations of the Input Data for the DFN Generator

### 5.1.1 Horizon Grid Construction

In the TWTT seismic profile, two main horizons were picked near the interval of the Lower Cretaceous: the Base Cenozoic and Top Jurassic reflectors (Figure 3.4). Two surfaces were generated based on the two picked horizons in both seismic lines in time domain and then they were converted to depth domain. To create the structural model, the Top Jurassic depth surface was shifted up vertically to tie with the corresponding well tops in GEO-01. This was performed to create the depth surfaces for all the formations except the top one (Vallorbe Fm) where it was created by shifting the Base Cenozoic depth surface vertically down to tie with Vallorbe Fm top in GEO-01 well (Figure 5.1).

Each interval in the structural model is divided into 2 m thick layers (Figure 5.2 C. The constant thickness layering is compatible with the DFN Generator tool where it discards the effect of the layer thickness on the intensity of the modelled fracture network.

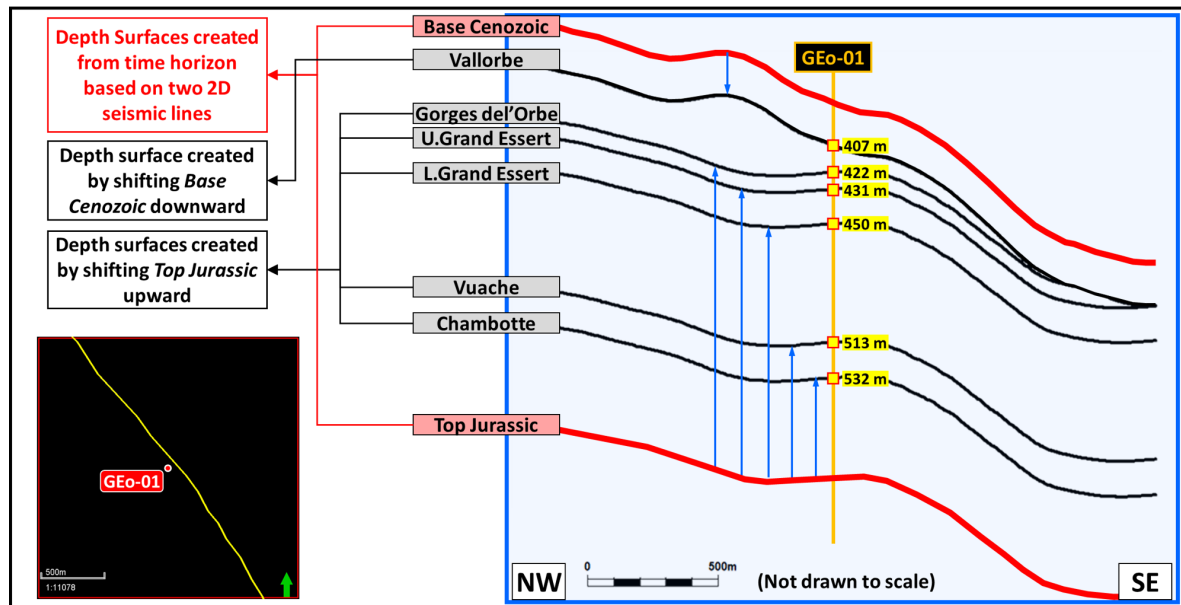


**Figure 5.1:** Schematic cross-section illustrating the construction of the modelling grid horizons. The lower left figure shows the cross-section location within the study area in a map view. The formation well tops are presented in meters Measured Depth (mMD).

### 5.1.2 Fault Model

The provided 2D fault interpretations in the TWTT seismic profile consist of six faults (Figure 3.3). The traces of the 2D fault interpretation on the seismic profile were converted from the time domain to the depth domain. The depth traces of the 2D faults were extended laterally in the 3D space with a specific strike direction (Figure 5.3). The faults were extended to the edge of the study area with a strike direction of ENE-WSW ( $068^\circ$ ). The chosen strike direction is based on the provided 3D fault model.

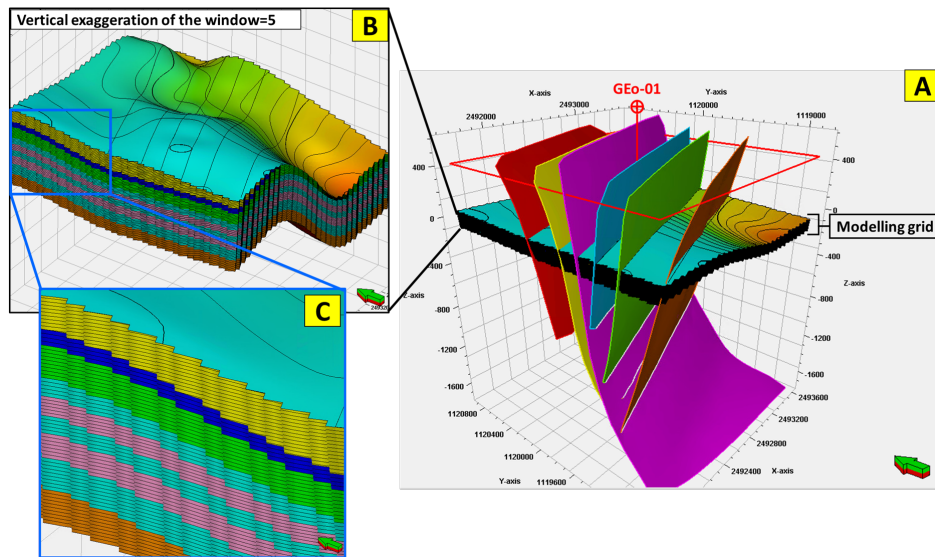


**Figure 5.2:** A) Structural model that includes the horizon grid and the faults. B) The modelling grid of all the formations in the Lower Cretaceous, (yellow=Vallorbe Fm), (blue=Gorges de l'Orbe Fm), (green=Upper Grand Essert Fm), (light blue & pink=Lower Grand Essert Fm), and (orange=Vuache Fm). In Lower Grand Essert light blue=soft and pink=stiff, based on the stiffness layering. C) Horizon grid showing that each formation is divided into 2 m thick layers.

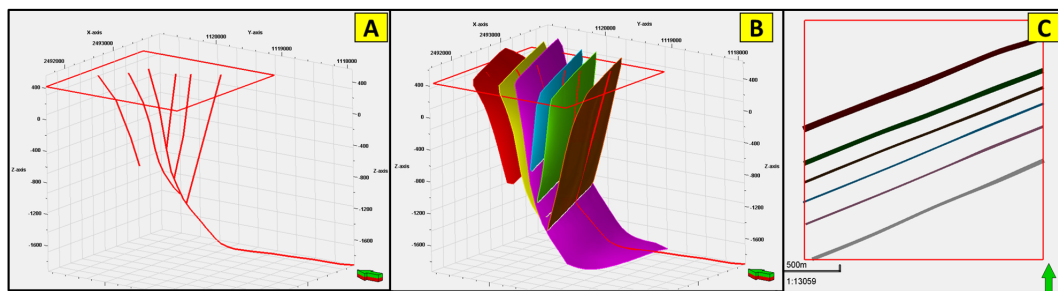


**Figure 5.3:** A) 3D view shows the depth fault traces. B) 3D view shows the laterally extended fault into the 3D space with an angle of  $68^\circ$  with respect to the north. C) Top view showing the faults parts that intersect the modelling grid. The red box represent the 2x2 km study area.

### 5.1.3 Geomechanical Logs and Rock Stiffness Partitioning Results

#### 5.1.3.1 Young's Modulus and Poisson's Ratio Logs Results

##### Young's Modulus Calculation Using a Scaling Factor

To investigate the reliability of [Yasar and Erdogan \(2004\)](#) empirical relations, velocity log was calculated using the measured density log in Equation 4.2. The calculated velocity log was compared with the measured P-sonic in GEO-01 by plotting them together in the same graph (Figure 5.4 A). The comparison shows a shift between the two logs, however, both logs illustrate the same general trend. To compensate for the observed shift between the measured P-sonic and calculated velocity logs, different scaling factors were applied on the measured P-sonic using Equation 5.1.

$$(Scaled\ Psonic) = (Measured\ Psonic) * Scaling\ Factor \quad (5.1)$$

The range of the applied scaling factors was between 1.0 and 1.8 with a 0.1 increment. Every time a scaling factor is applied to the measured P-sonic log, the difference between the scaled P-sonic and the calculated velocity logs was quantified. The quantification was done by obtaining the root mean square error (RMSE) between the values of the two logs using Equation 5.2 ([Barnston, 1992](#)). The scaling factor of 1.4 resulted in the lowest RMSE (Figure 5.5). The calculated velocity and the scaled-measured P-sonic with a scaling factor of 1.4 are compared by plotting them in the same graph (Figure 5.4 B). In general, both logs display the same trend and values. The Young's modulus log was calculated using the scaled-measured P-sonic with a scaling factor of 1.4 in Equation 4.1 (Figure 5.6 A).

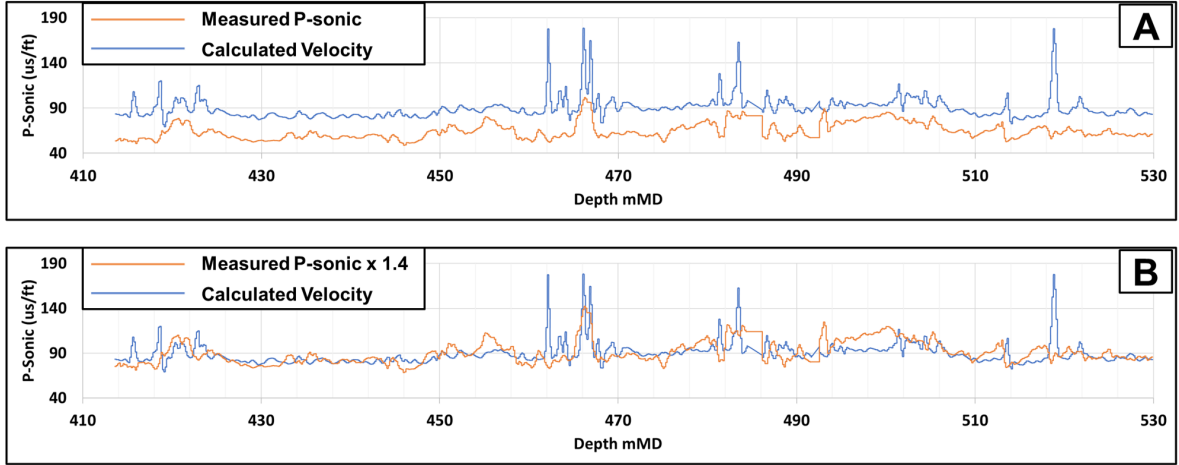


**Figure 5.4:** The blue lines represent the calculated velocity log using the SV-density relation in Equation 4.2. The orange line in (A) represents the measured P-sonic log in GEO-01. The Orange line in (B) represents the measured P-sonic log in GEO-01 scaled with a factor of (1.4).

$$RMSE = \sqrt{\frac{\sum_{i=1}^N (x_i - \hat{x}_i)^2}{N}} \quad (5.2)$$

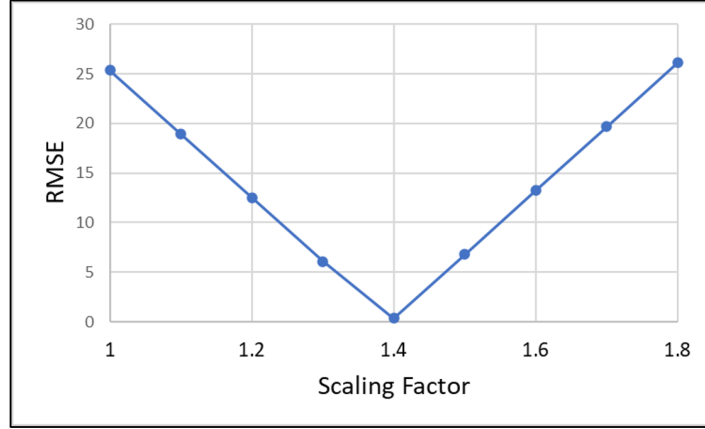


**Figure 5.5:** Different RMSE values between the measured and calculated P-sonic using different scaling factors for the measured P-sonic.

### Alternative solution of Young's modulus log

[Koumrouyan \(2019\)](#) calculated the Young's modulus log in GEO-01 well using a different approach. In this approach, P-wave ( $V_p$ ) and S-wave ( $V_s$ ) velocities are estimated using semblance analysis which is based on the datasets recorded by the full-waveform sonic tool. The estimated  $V_p$  and  $V_s$  in addition to the density logs ( $\rho_b$ ) were used to calculate the Young's modulus ( $E$ ) log (Figure 5.6 B). The Young's modulus log is calculated using Equation 5.3 ([Mari and Vergniault, 2021](#)).

$$E = \rho_b V_s^2 \frac{3V_p^2 - 4V_s^2}{V_p^2 - V_s^2} \quad (5.3)$$

The calculated Young's modulus logs using [Koumrouyan's](#) approach and [Yasar and Erdogan Scaled \(1.4\)](#) approach, are compared in Figure 5.6 C. In general, the two logs show good correlation, however, at the following intervals (420-445 mMD), (470-480 mMD), and (520-530 mMD), [Koumrouyan E](#) log displays lower values.

As it is illustrated in Table 5.1, high correlation values between Sound Velocity index and Young's Modulus of  $R^2 = 0.86$  and density of  $R^2 = 0.81$  were found.

**Table 5.1:** Results of regression equations and the correlation coefficients ([Yasar and Erdogan, 2004](#)).

Parameters to be related	Regression equation $Y = AX \pm B$	$R^2$
SV-Young's modulus	$SV = 0.0937E + 1.7528$	0.86
SV- density	$SV = 4.3183\rho - 7.5071$	0.81

To quantify the error in the [Yasar and Erdogan Scaled \(1.4\)](#) Young's modulus log, error bars were established using 20% error margin. Using a scaling factor of 1.2 instead of 1.4 results in a 20% decrease in the Young's modulus log. While using a scaling factor of 1.6 instead of 1.4 results in a 20% increase in the Young's modulus log. The two edges of the error bars represent the result of Young's modulus logs using the scaling factors of 1.2 and 1.6. Young's modulus log that is calculated using [Koumrouyan's](#) approach have its values within the range of the established error bars (Figure 5.6 C).



### Poisson's Ratio Calculation

To calculate the Poisson's ratio log, the measured P-sonic log was directly used in Equation 4.3. The range of the values of Poisson's ratio log is narrow where it fluctuates between 0.27 and 0.31 (Figure 5.6 D).

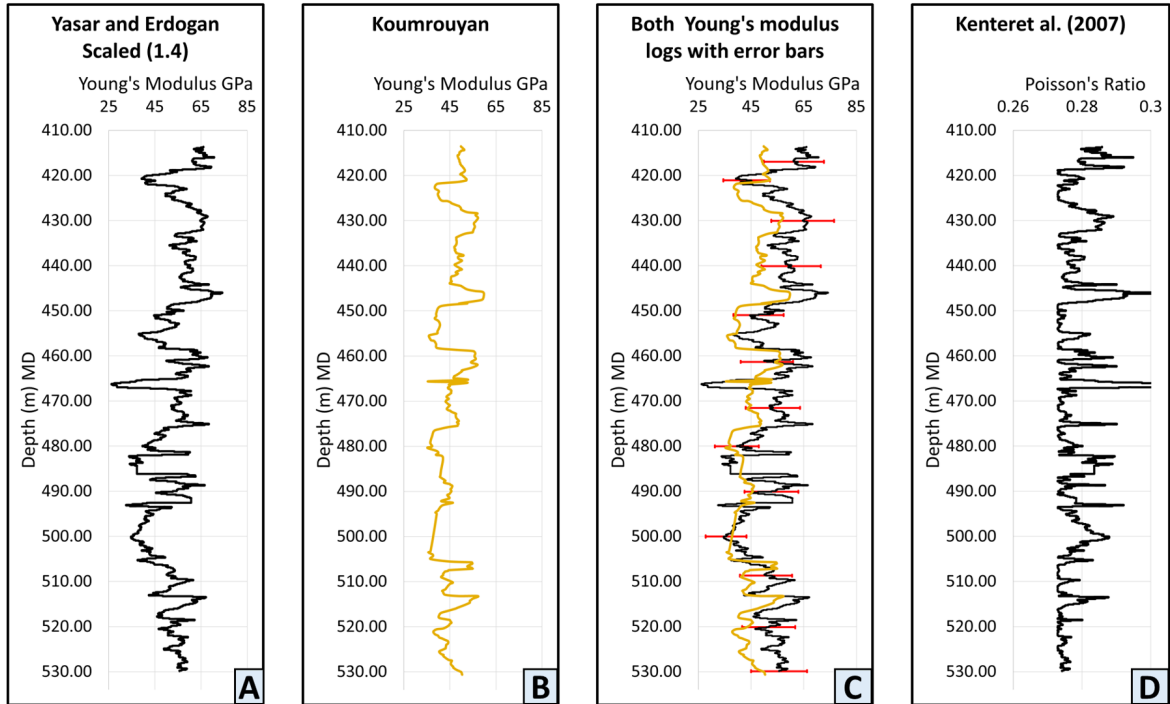


**Figure 5.6:** A) Young's modulus log that is calculated using the empirical relation provided by [Yasar and Erdogan \(2004\)](#) and using scaling factor of (1.4). B) Young's modulus log that is calculated by [Koumrouyan \(2019\)](#). C) Both Young's modulus logs on the same graph with the error bars for the Yasar and Erdogan scaled (1.4) log. The error bars represent the two scaling factors (1.2 & 1.6). D) The Poisson's ratio log that is calculated using the empirical relation provided by [Kenter et al. \(2007\)](#).

#### 5.1.3.2 Stiffness Upscaled Log Result

The lower Cretaceous interval was partitioned based on rock's stiffness. Based on the average of the logs values across the Lower Cretaceous interval, the Gamma ray ( $GR$ ) cutoff is found to be 16  $API$  and the Young's modulus ( $E$ ) cutoff is 53  $GPa$ . The cutoff values in addition to the mentioned criteria in Section 4.3.2 were used to calculate the rock's stiffness log (Figure 5.7 A). In the stiffness log, the blue colour represents soft rock interval  $[(GR > 16 API) \text{ and } (E < 53 GPa)]$ . The red colour represents stiff rock interval  $[(GR < 16 API) \text{ and } (E > 53 GPa)]$ . The green colour represents an interval where the  $GR$  and  $E$  logs do not meet any of the previous two criteria. The stiffness log was upscale manually. The decision to define the Lower Cretaceous geomechanical intervals is based on the the Upscaled Stiffness log where the whole interval was divided into 9 geomechanical layers (Figure 5.7 B).

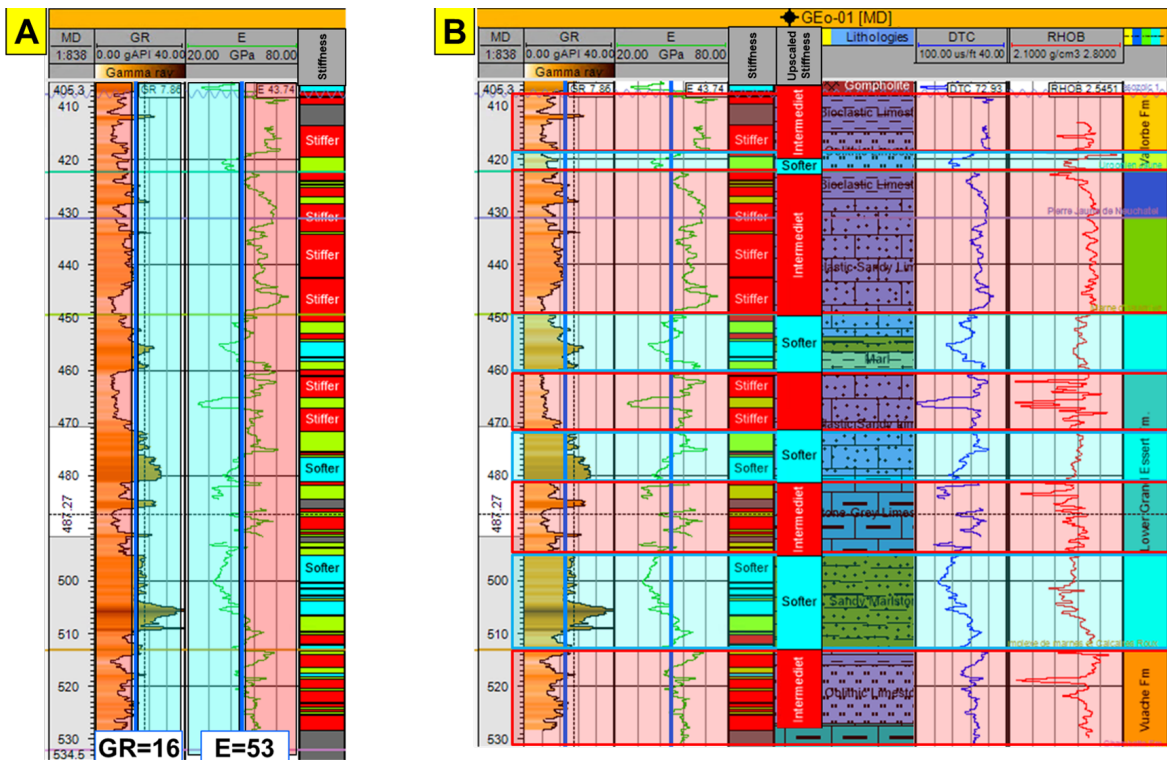


**Figure 5.7:** A) Well logs from GEO-01 well illustrating the Gamma ray  $GR$ , Young's modulus  $E$ , and Stiffness logs. It is also illustrating the cutoff values of  $GR = 16API$  and  $E = 53GPa$ . B) Well logs from GEO-01 well illustrating the Gamma ray  $GR$ , Young's modulus  $E$ , Stiffness, Upscaled Stiffness, lithology, P-sonic, and density logs. The red and blue shaded layers represent stiff and soft rock intervals, respectively.

## 5.1.4 Fracture Analysis and Stress State Interpretation

### 5.1.4.1 Analysis of the Fracture Data

To start with a simple fracture analysis, the following assumption have been made:

- All the fractures are assumed to be formed under the same tectonic event.
- The principle stress state is considered to remain the same for that specific tectonic event.

The full fracture dataset is analysed as one group. The fractures have a consistent dip angle around  $60^\circ$  (Figure 5.9 C). The fracture data show a variety in term of strike direction. The fractures have a variable orientation comprised between NNE-SSW and E-W (Figure 5.8 A).

### 5.1.4.2 Principle Stress State Interpretation

The fractures pole density in the stereonet shows the fractures to have dip azimuth in opposite direction (Figure 5.8 B). In the stereonet, the poles of the fracture data are confined within two arc regions. This fracture pattern suggests that the fractures were formed under a normal tectonic regime. The interpretation of the two arc regions of the fracture poles resembles a

polymodal fracturing system (Healy et al., 2015). The example analogue of the polymodal fracturing system in Figure 5.8 C helped in the interpretation of the principle stress configuration. From the fracture data, the principle stresses are interpreted as following:  $\sigma_1$  to be slightly tilted from vertical,  $\sigma_2$  is oriented NE-SW, and  $\sigma_3$  is oriented NW-SE (Figure 5.9 A).

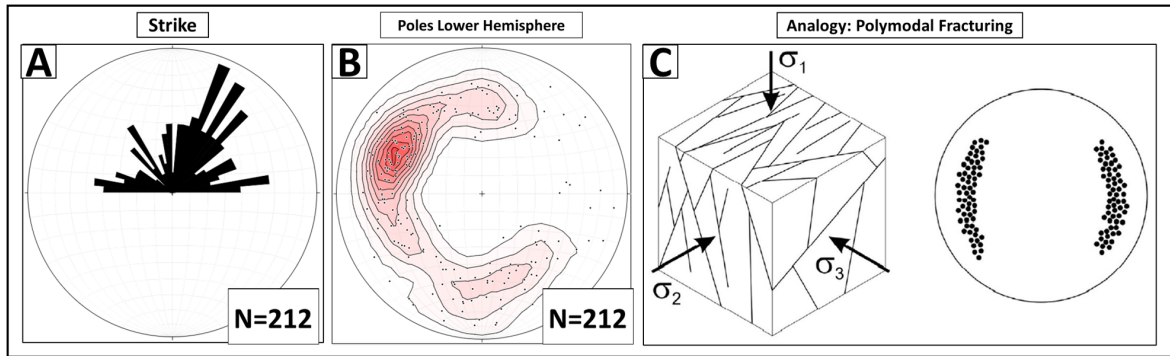


**Figure 5.8:** A) Rose diagram representing the strike of the fracture data. B) Lower hemisphere stereonet illustrating poles the fractures and pole density. C) Schematic block diagrams and correspondent pole measurement of fractures (Lower hemisphere) for a polymodal fracture pattern (Healy et al., 2015).

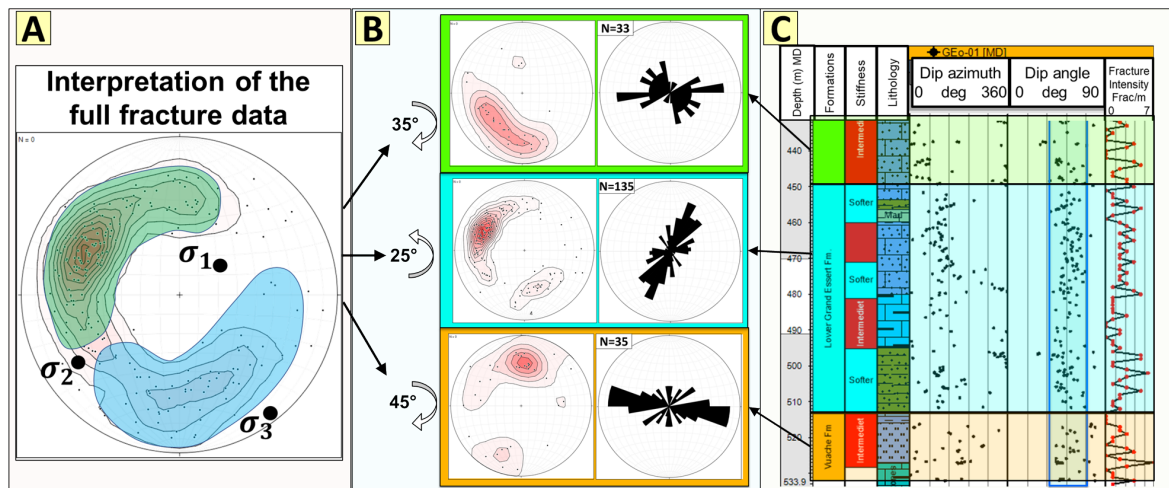


**Figure 5.9:** A) The density of the fractures poles with the interpretation of the related principle stress state. The green and blue arc regions show where the poles of the fractures are confined. B) Fractures strike rose diagram and the fractures pole density for the Upper Grand Essert, Lower Grand Essert, and Vuache Formations. C) Fracture data in GEO-01.

### 5.1.4.3 Fracture Stratigraphy and Fracture Different Directions

The fracture data were partitioned into different groups based on stratigraphic formation. Each fracture group was analysed individually. Due to the scarcity of the fracture number in Vallorbe and Gorges de l'Orbe Formations, the fracture stratigraphy analysis is performed on Upper Grand Essert, Lower Grand Essert, and Vuache Formations. It can be seen that both the Upper Grand Essert and Vuache Formations show a dominant fracture strike orientation

of E-W. On the other hand, Lower Grand Essert Fm. shows a dominant fracture strike orientation of NNE-SSW (Figure 5.9 B&C). A change in the orientation of the fractures is observed in the three formations. Two reasons could explain the observed rotation:

- Variation in rock's stiffness between different stratigraphic layers can induce some variation of the in situ stress magnitude and of the fractures orientation (Stephansson and Zang, 2012). In the Stiffness upscaled log, 3 out of 5 geomechanical layers in the Lower Grand Essert Formation are interpreted as soft layers (Figure 5.7). This could reduce the overall stiffness of the whole formation. This contrast of rock's stiffness between the Lower Grand Essert Formation and the surrounding formations can cause the Lower Grand Essert Formation to accommodate the stress differently and results in a different fracture geometry.
- The proximity of GGeo-01 to the fault damage zone could be another possible reason for the variation of the fractures' orientation. The influence of fault's damage zone on the fractures in GGeo-01 well is investigated. Johri et al. (2014) have studied the fault damage zones in two large scale faults areas. The damage zone in both cases are estimated to have a width of 50 to 80 m. It worth mentioning that the size of the modeled fault around GGeo-01 are much smaller than the two studied faults by Johri et al. (2014). By looking at the map view of the well location and the modelled faults at the Lower Cretaceous level, the shortest distance between GGeo-01 well and the closest modelled TF1 fault is 50m (Figure 5.10).

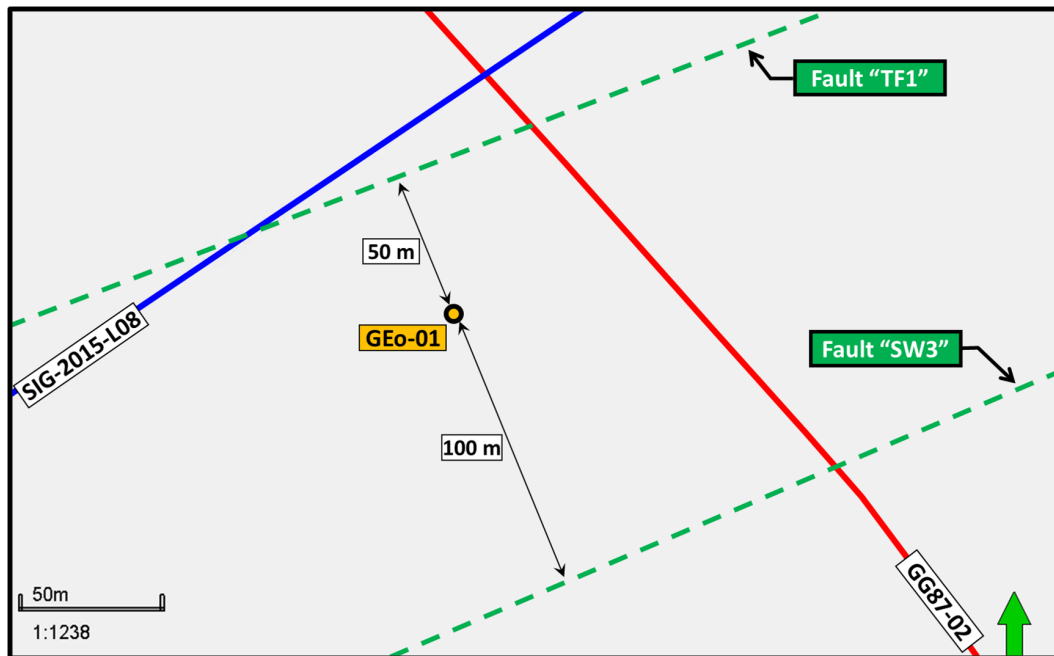


**Figure 5.10:** Map view showing two faults, TF1 and SW3, at the level of the Lower Cretaceous represented by the dashed green lines. It is illustrating the shortest distances between GGeo-01 and the two faults. The red and blue lines are GG-87-02 and SIG-2015-L08 seismic lines, respectively.

## 5.1.5 Estimating Paleo-tectonic stresses and Strain tensors

### 5.1.5.1 Faults Selection and Faults Sizes

The fault model, that was used in the stress inversion tool, had to be simplified for technical reason associated to the DFN Generator tool. The fault simplification is based on the seismic reflector continuity within the Lower Cretaceous interval. Three out of the six interpreted faults, that displaying clear discontinuities in the seismic reflector, are chosen to construct the input fault model in the paleo-tectonic stress inversion tool (Figure 5.11). The selected faults are NW1, SW3, and SW1, where NW1, TF1, and SW2 were discarded.

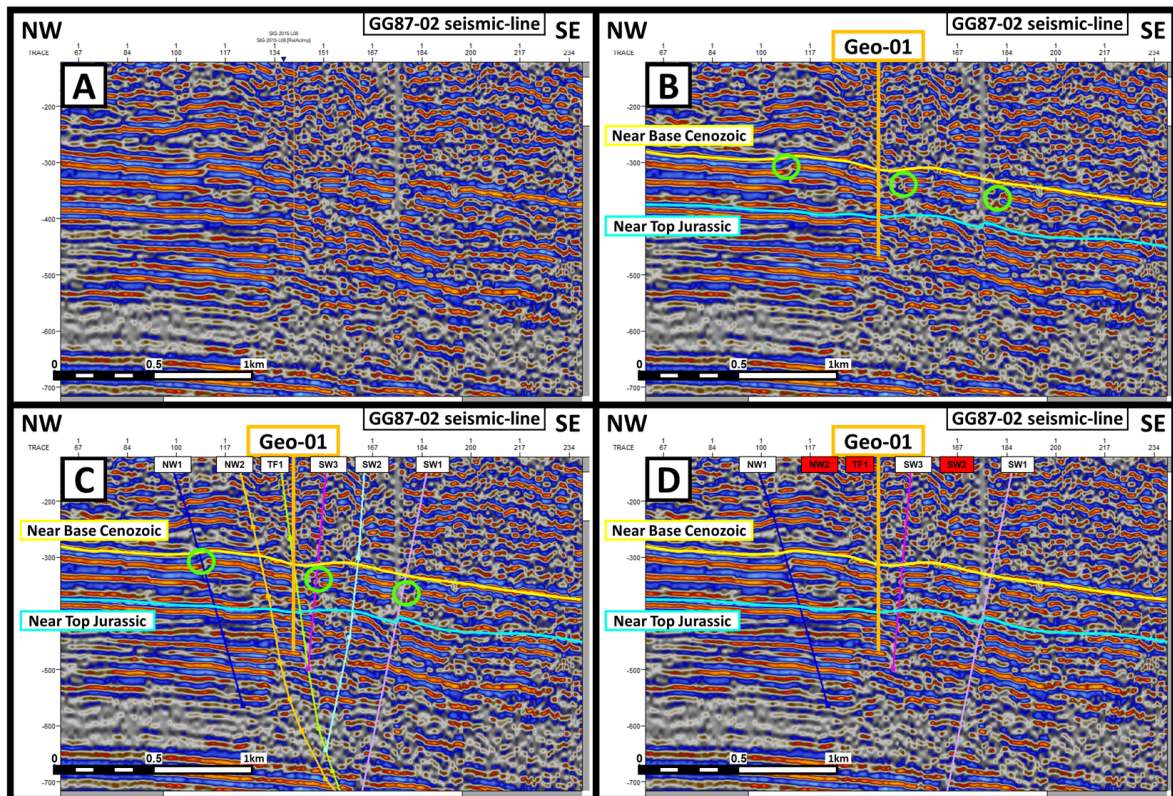


**Figure 5.11:** A) Plain GG87-02 seismic-line. B) The green circles are highlighting the main discontinuities between the Base Cenozoic and Top Jurassic horizon interpretation. C) Illustrating the interpretation of the six faults. D) Illustrating the three selected faults for the fracture network modelling.

The inversion tool does not offer an option to control the fault slip, so the faults are slipping freely during the inversion. The amount of faults slip is associated with the fault size. The slip amount increases with larger faults and decreases with smaller faults. (Figure 5.12). The faults in the study area are assumed to have minor displacement. This assumption is supported by the seismic data where the maximum vertical reflector discontinuity is 20 ms which is translated roughly to 20-30 m. The displacement that is resulted from the slip of the faults in Figure 5.12-C is very close to the estimated displacement from the seismic reflectors. Hence, the fault geometry in Figure 5.12-C is chosen to be used as input in the inversion tool.

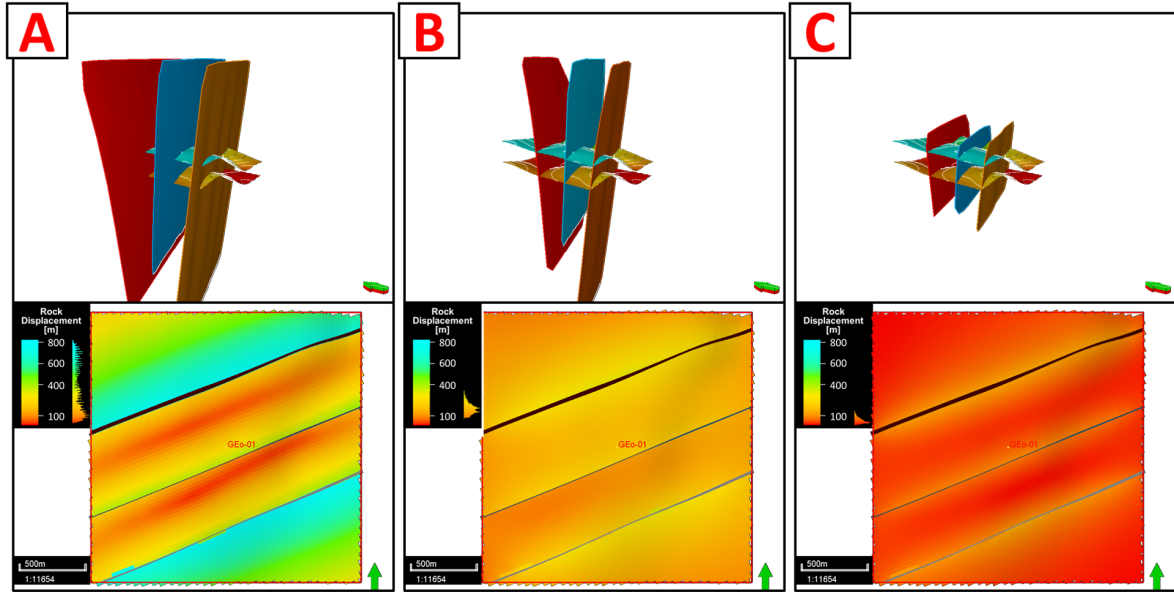


**Figure 5.12:** The top figures illustrating three fault geometries for the inversion tool. The bottom figures illustrating the displacement distribution resulted from the faults slip. All figures have the same colour scale (Red=0 m and blue=800 m). A) Faults with 4km lateral extension. B) Faults laterally extended to the edge of study area. C) Faults that are laterally extended to the edge of study area and cropped vertically from top and bottom.

### 5.1.5.2 Relation between Fracture Geometry and Different Stress Configurations

At the beginning, the inversion is performed using the auto-calculated option. The input for this option are a horizon from the 3D modelling grid, the fault model, and the mechanically classified fracture data. The result of the auto-calculated option is a tectonic domain that represents all the simulations' fitting values between the input fracture geometry and different stress configurations (Figure 5.13). The simulation that illustrates the best fit between the modelled stress and the observed fracture geometry shows a strike-slip regime with 61% fit. However, under the normal regime area in the tectonic domain, where  $\sigma_H$  orientation is between  $20^\circ$  and  $100^\circ$ , the tectonic domain shows high fitting values around 55%. The high fitting of the normal regime is aligned with the pattern of the fracture data which suggests the fractures are formed under a normal regime.

### 5.1.5.3 Producing the Strain Tensors ( $\varepsilon_{xx}$ , $\varepsilon_{yy}$ , and $\varepsilon_{xy}$ )

Due to the the limitation in the paleo-tectonic stress inversion tool, where it ignores the effect of the fracture (see section 4.5.4), the strain values are scaled down with a scaling factor of 100. This scaling factor is chosen because it reduces the assumed strain value in this study ( $3.00E-3$ ) to a typical strain value where fracture network starts to form (around  $-1E-5$ ). The typical strain value (around  $-1E-5$ ) is found from modelling experience of Welch et al. (2019) and Welch et al. (2020). Assuming an uniaxial applied horizontal strain, the maximum horizontal strain  $\varepsilon_{h\max}$  and minimum horizontal strain  $\varepsilon_{h\min}$  are chosen to be 0 and  $-3.00E-05$ , respectively. Using the inputs from Table 5.2, the principal stresses of a

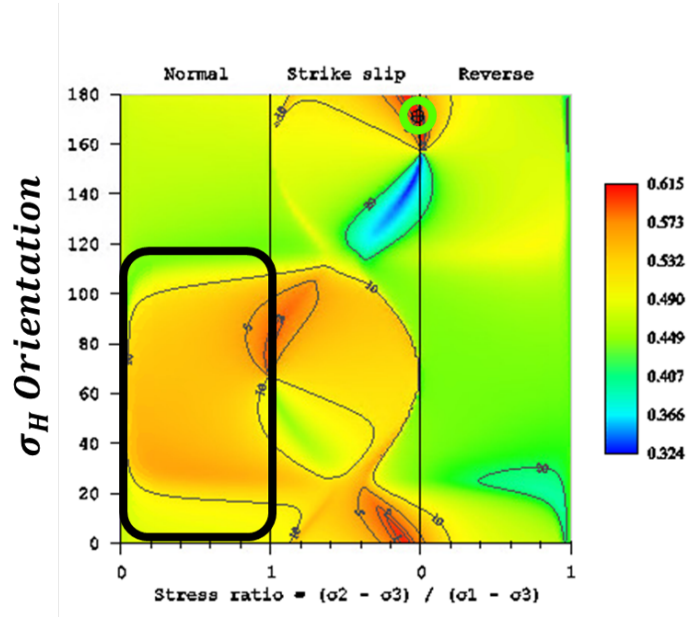


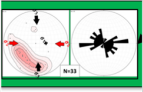
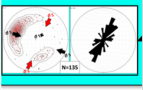

**Figure 5.13:** Tectonic domain showing the result of the paleo-tectonic stress inversion on the data. Green circle represents the simulation with the best fit between the modelled stress and the observed fracture geometry. The black rectangle represent simulations with high fit 55%.

normal regime are calculated using Equations 4.4, 4.5, and 4.6. The results of the calculated principal stresses are as following:  $\sigma'_V = 5.5 \text{ MPa}$ ,  $\sigma'_{H \max} = 1.6 \text{ MPa}$ , and  $\sigma'_{h \min} = 0.4 \text{ MPa}$ .

**Table 5.2:** The input used in the stresses calculations.

Input	Symbol	Value	Unit
Depth	$z$	450	m
Gravity	$g$	9.81	m/s <sup>2</sup>
Rock Density	$\rho_{Rock}$	2250	kg/m <sup>3</sup>
Fluid densit	$\rho_{Fluid}$	1000	kg/m <sup>3</sup>
Maximum horizontal Strain	$E_{h \max}$	0	–
Minimum horizontal Strain	$E_{h \min}$	-3.00E-05	–
Yong's modulus	$E$	5.05E+10	Pa
Poisson ratio	$\nu$	0.27	–

The tectonic inversion tool was run three times for each of the targeted sedimentary formations (Upper Grand Essert, Lower Grand Essert, and Vuache Formations). In all runs, the same calculated principal stresses ( $\sigma'_V$ ,  $\sigma'_{H \max}$ , and  $\sigma'_{h \min}$ ) were used as inputs whereas the orientation of maximum horizontal stress ( $\sigma_{H \max} \text{ Orientation}$ ) is used differently.  $\sigma_{H \max} \text{ Orientation}$  was chosen based on the interpretation of fractures pattern in each of the targeted sedimentary formations (Figure 5.14). Moreover, in each run, the horizon input corresponds to the top of the associated sedimentary formation. Therefore, the resulted principle strain tensors ( $E_{xx}$ ,  $E_{yy}$ , and  $E_{xy}$ ) are presented along the input horizons. The perturbed field around the faults are captured in the strain tensors outputs (Figure 5.15).

$\sigma_H$ Orientation	Fracture Data	Formation
90°N		U. Grand Essert Fm.
30°N		L. Grand Essert Fm.
100°N		Vuache Fm.

**Figure 5.14:** The input orientations of the maximum horizontal stress for different formations based on the fracture data interpretations.

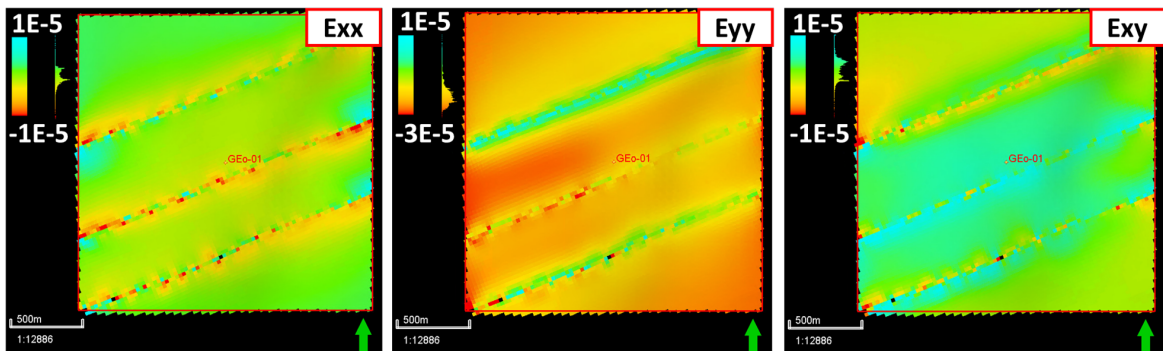


**Figure 5.15:** An example of the principal strain tensors output with  $\sigma_{H \max}$  orientation=90° along Upper Grand Essert Formation.

## 5.2 Discussion and Uncertainties of the Input Data for the DFN Generator

### 5.2.1 The Structural Model Uncertainties

The main uncertainties of the structural model resulted from the scarcity of data which prevents the geometries of the subsurface to be adequately captured. The available 2D seismic profiles do not capture all the details of the fault geometry. The orientations of the laterally extended faults are unknown where assumptions have to be made to build the fault model. The produced strain tensors using the inversion tool are based on the interaction between the far-field stress configuration input and the fault model. When fault model is changed, by changing the faults' orientation, the inversion tool will produce different distribution of the strain tensors. Consequently, different strain tensor distribution will cause the fractures to propagate differently in the DFN Generator tool. Therefore, any change in the faults' orientation will influence the results of the final DFN model.

The range of fault damage zone thickness in the study area was estimated to be 50-80m (see section 5.1.4.3). A change in the faults' orientation will make the distance between the fault and the location of GEO-01 well larger or smaller (Figure 5.16). Therefore, the lack of understanding of the subsurface faults orientation introduces an uncertainty of whether GEO-01 well is located within a fault damage zone or not.



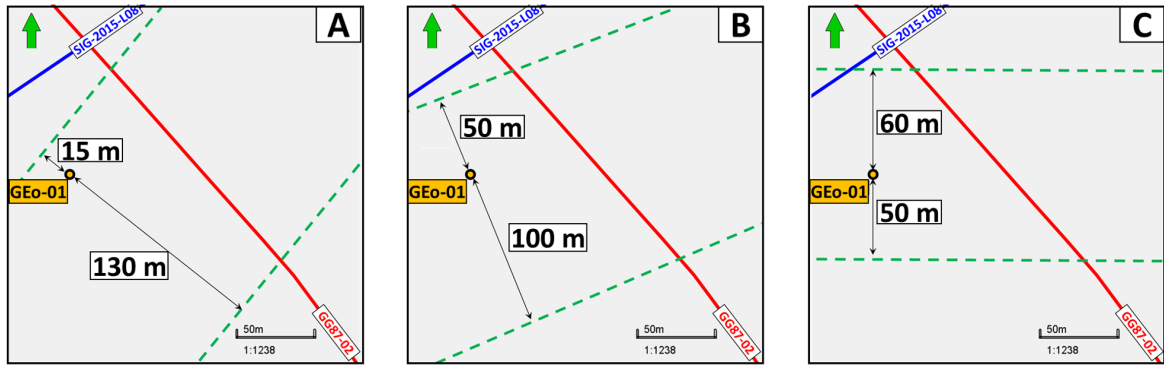


**Figure 5.16:** Distances between GGeo-01 well and the faults (TF1 & SW3) at Lower Cretaceous level with the following strike angles with respect to north: A) 40°, B) 68°, and C) 90°.

## 5.2.2 Scaling Factor discussion and Young's Modulus Log Selection

Part of the Young's modulus calculation process, a scaling factor of 1.4 had to be applied on the measured P-sonic log to use the empirical relations that are obtained by [Yasar and Erdogan \(2004\)](#). The scaling factor could possibly be forcing the measured P-sonic log to match the calculated velocity log. Nevertheless, the empirical relations are obtained using rock samples test results in the laboratory whereas the P-sonic and density logs in GGeo-01 are measured on site. Therefore, the scaling factor might have to be applied to correct the difference between the two different datasets.

The difference between the approaches of [Koumrouyan](#) and [Yasar and Erdogan](#) scaled (1.4) to calculate the Young's modulus logs is that [Koumrouyan](#)'s approach used two steps to calculate the Young's modulus log: estimate the  $V_p$  and  $V_s$  and then calculate the Young's modulus log. In the [Yasar and Erdogan](#) Scaled (1.4) approach, only one step is used to calculate the Young's modulus log by directly using the established empirical relation. This could be an advantage for the latter approach to be used in this project.

## 5.2.3 Rock Stiffness Partitioning Uncertainties

The process of dividing the whole interval into 9 different layers has uncertainties. The method depends mainly on the Young's modulus logs which itself includes assumptions and uncertainties during calculation. Moreover, the stiffness log contains three colours, the blue colour corresponds to soft intervals, the red colour corresponds to stiff intervals, and the green colour corresponds to intervals that do not meet any of the two assigned criteria (see section 5.1.3.2). In the calculated stiffness log, there are few intervals that have green colour. During the upscaling process of the stiffness log, those green intervals were assigned to either the soft or stiff rock group. At intervals where the borehole condition is bad and the Young's modulus log becomes unreliable, the Gamma ray log is used alone to assign the green interval to the soft or stiff rock group. The decision of assigning the green intervals could also be based on a combination of various petrophysical logs. For example, the green interval at depth 420 mMD is assigned in to the soft rock group because of the low value of the density and P-sonic logs (Figure 5.7).

#### 5.2.4 Fracture Data Related Tectonic Events

The pattern of fracture data in GEO-01 well suggests that the fractures were formed under a normal tectonic regime. The study of faults data in the outcrops of the Jura Mountains suggests that several stress state have successively took place (Hombert et al., 2002). After the analysis of the collected faults data in Jura Mountains, three main stages were identified: N-S compression during Eocene, WNW-ESE Extension during Oligocene, and a compression with a fan-shape stress distribution almost perpendicular to the major thrust axes during Late Miocene. The interpretation of the normal tectonic regime from the fracture data in GEO-01 could be related to the identified WNW-ESE extensional stage. Nevertheless, the timing of the observed fractures formation is uncertain.

#### 5.2.5 Uncertainties of the Paleo Stress Inversion Results

In this project, the paleo-tectonic stress inversion technique is used mainly to produce the distribution of the strain tensors that are related to the calculated stresses. The strain tensors are main inputs in the DFN Generator tool and they have major influence on the final DFN model. The produced strain tensors are based on fixed values of the elastic rock properties, Young's modulus and Poisson's ratio. This uncertainty should be taken in consideration when using the output strain tensors.

Moreover, The size of the used fault model during the inversion is reduced where the faults were cropped vertically from the top and the bottom. The advantage of this step is that it makes the modelled fault displacement resembles the same range of the identified fault displacement in the seismic data. However, the modification of the fault size might introduce an uncertainty to the result of the tectonic domain results.

# Forward Modelling (DFN Model Generation)

# 6

In this project, the DFN model was generated for the following stratigraphic formations: Upper Grand Essert, Lower Grand Essert, and Vuache Formations. This chapter describes the inputs and how they are used in the DFN Generation tool.

## 6.1 Forward Modelling Inputs

### 6.1.1 Default Input Parameters

All the default parameters are kept the same in all DFN modelling runs as listed in Table 6.1. For the DFN Generator detailed settings, refer to Appendix B.1. The present day depth of the targeted reservoir is used as a proxy for the input of "depth at time of deformation". Furthermore, the mean density of the overlying sediments is calculated by averaging the density log in GEO-01 well.

**Table 6.1:** Mechanical properties and stress state default input parameters that are used in the DFN Generation.

<b>Stress State Inputs</b>	Value	Unit
Stress distribution scenario	Stress shadow	
Depth at time of deformation	400	m
Mean density of overlying sediments	2400	kg/m <sup>3</sup>
Fluid density	1000	kg/m <sup>3</sup>
Initial fluid overpressure	0	Pa
Initial stress relaxation	1	-
<b>Mechanical Properties</b>	Value	Unit
Biot Coefficient Inputs	1	-
Friction coefficient on the fractures	0.5	-
Crack surface energy	1000	J/m <sup>2</sup>
Rock strain relaxation time constant	0	ma
Fracture strain relaxation time constant	0	ms
initial microfracture density	0.001	frac/m <sup>3</sup>
Initial microfracture size distribution coefficient	2	-
Subcritical fracture propagation index	10	-
Critical fracture propagation rate	2000	m/s

### 6.1.2 Young's Modulus and Poisson's Ratio Models Creation

The calculated Young's modulus and Poisson's ratio logs in section 5.1.3.1 are used to populate the 3D grid. First, both logs were upscaled based on the 2m thick layers in the 3D grid using arithmetic average method. The upscaled logs were used as inputs in a Petrophysical

Modelling tool in *Petrel 2018* to populate the upscaled logs in 3D grid using a method in called "Closest". In this method, the upscaled values in each layer were populated laterally along its correspondent layer in the 3D modelling grid. The final products are 3D models of both properties (Figure 6.1).

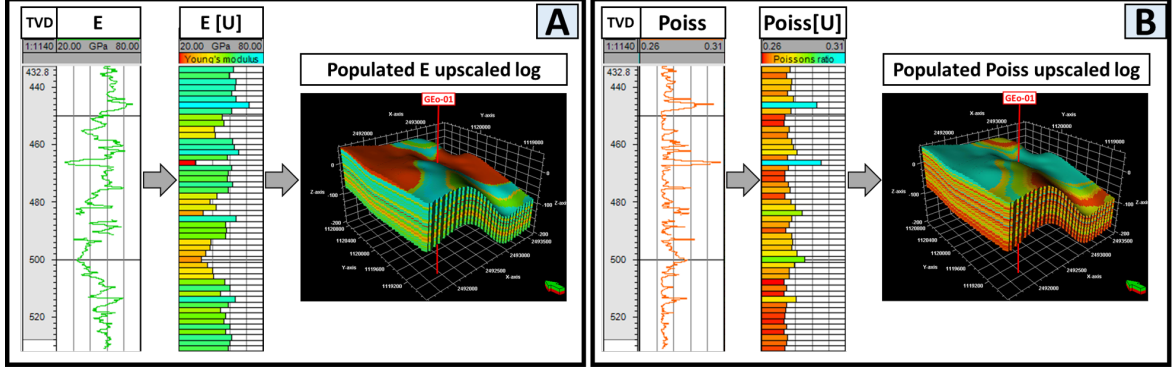


**Figure 6.1:** Well log, upscaled well log, and populated properties in the modelling grid of both properties: A) Young's modulus and B) Poisson ratio. (Vertical exaggeration of the window=5).

### 6.1.3 Strain Related Models

Due to a limitation in the paleo-tectonic stress inversion tool, the assumed strain value in this project ( $3E-03$ ) was scaled down by a factor of 100 (see section 5.1.5.3). Therefore, for each stratigraphic formation, the correspondent produced principal strain sensors ( $\varepsilon_{xx}$ ,  $\varepsilon_{yy}$ , and  $\varepsilon_{xy}$ ) were scaled up again using the same factor. The purpose of this step is to bring the strain values back to the same order of the original assumption.

The scaled up principal strain tensors were used as inputs to calculate the azimuth of minimum horizontal strain ( $\theta$ ), the minimum horizontal strain ( $\varepsilon_{hmin}$ ), and the maximum horizontal strain ( $\varepsilon_{hmax}$ ) using Equations 4.8, 4.9, and 4.10. Using the assumed time period of the fractures formation ( $t= 1$  Ma), the minimum and maximum horizontal strain rates are calculated using Equations 4.11 and 4.12.

The results of the azimuth of minimum horizontal strain, the minimum strain rate, and the maximum strain rate are presented along the top horizons of each of the modelled stratigraphic formation. Those three results along the top horizon of each of the modelled formation were extrapolated vertically to populate the full 3D grid (Figure 6.2).

A quick test was performed to validate the vertical extrapolation step. In this test, the principal strain tensors were produced twice using the same input parameters. In the first time, they were produced along the top horizon of the 3D grid and in the second time they were produced along the bottom horizon of the 3D grid. The strain tensors results along both horizons are almost identical which confirms the validity of the vertical extrapolation step.

## 6.2 DFN Model Creation Approach and Results

### 6.2.1 DFN Model Creation Approach

The constructed 3D grid consists of 2m thick layers. Upper Grand Essert Formations includes 9 layers, Lower Grand Essert Formations includes 31 layers, and Vuache Formations includes

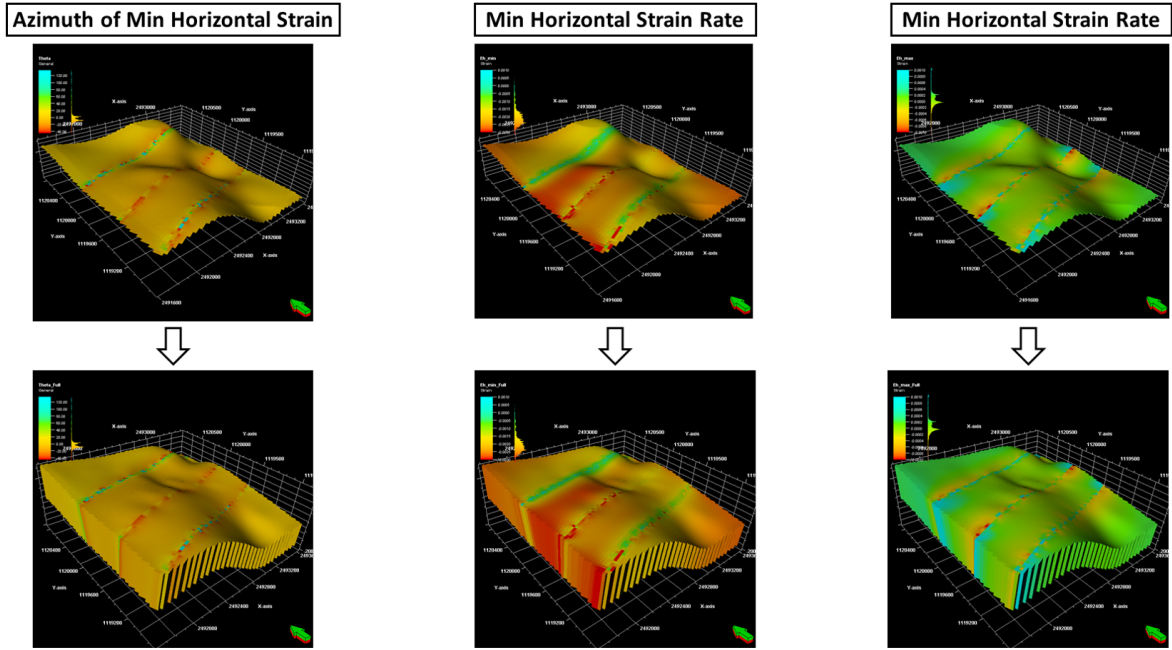


**Figure 6.2:** The top figures illustrate the properties along one Upper Grand Essert Formation. The bottom figures illustrate the populated properties in the full modelling grid. (Vertical exaggeration of the window=3).

9 layers. The DFN Generator was run over each layer separately to produce a total of 49 DFN layers (Figure 6.3). All the inputs remained the same except three input models: the minimum horizontal strain azimuth ( $\theta$ ), the minimum horizontal strain rate, and the maximum horizontal strain rate. Due to a limitation in the computational power, the DFN was run for all layers at three small locations (Figure 6.4). The size for Location 1 and 2 are 500x500m where for Location 3 is 500x800m. The locations were selected to capture the behaviour of the modelled DFN around the faults and also away from the faults.

## 6.2.2 DFN Results

In the 3D grid, the 2m layers in the same stratigraphic formation illustrate different values of Young's modulus and Poisson's ratio properties (Figure 6.1). However, the final DFN model shows that all DFN layers that are generated in one stratigraphic formation have almost identical fracture network. Therefore, the modelled DFNs are mainly influenced by the inputs of the strain models and not affected by the inputs of the elastic properties.

Examples of a single 2 m DFN layer in each stratigraphic formations are shown in Figure 6.5. The produced DFN layers in Upper Grand Essert and Vuache Formations show fractures, that are away from the faults, oriented almost E-W whereas in Lower Grand Essert Formation show fractures oriented NNE-SSW. This is similar to the observed fracture pattern in GGeo-01 well. Furthermore, the fractures tend to change their orientation when they are growing close to the faults. This is a response to the perturbed stress field that is modelled in the paleo-tectonic stress inversion tool.

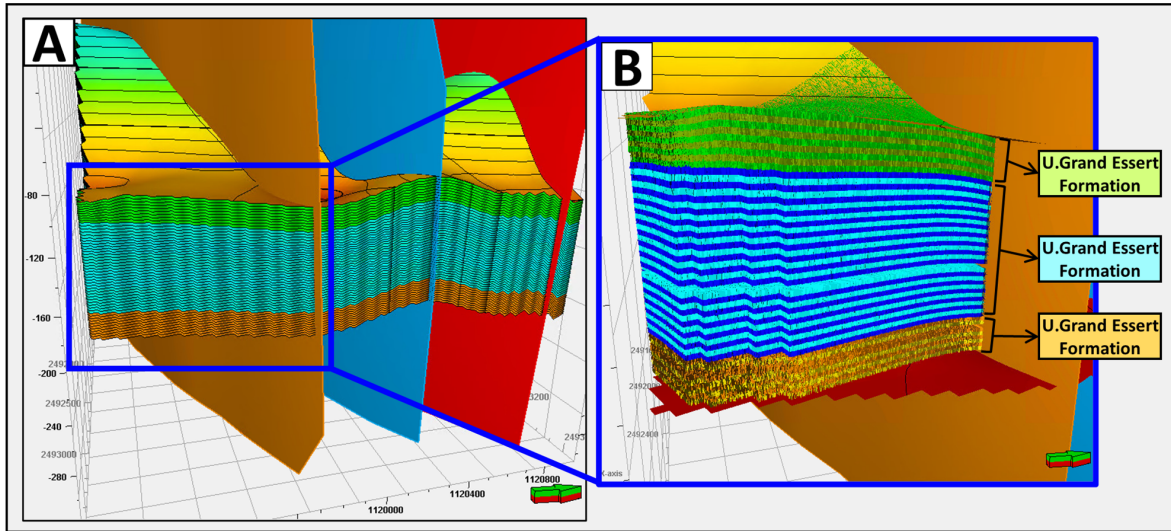


**Figure 6.3:** A) The modelling grid for the three formations, Upper Grand Essert (green), Lower Grand Essert (light blue), and Vuache Formations (orange). B) The populated DFN models in all layers for three the formations at (Location 3). (Vertical exaggeration of the window=5).

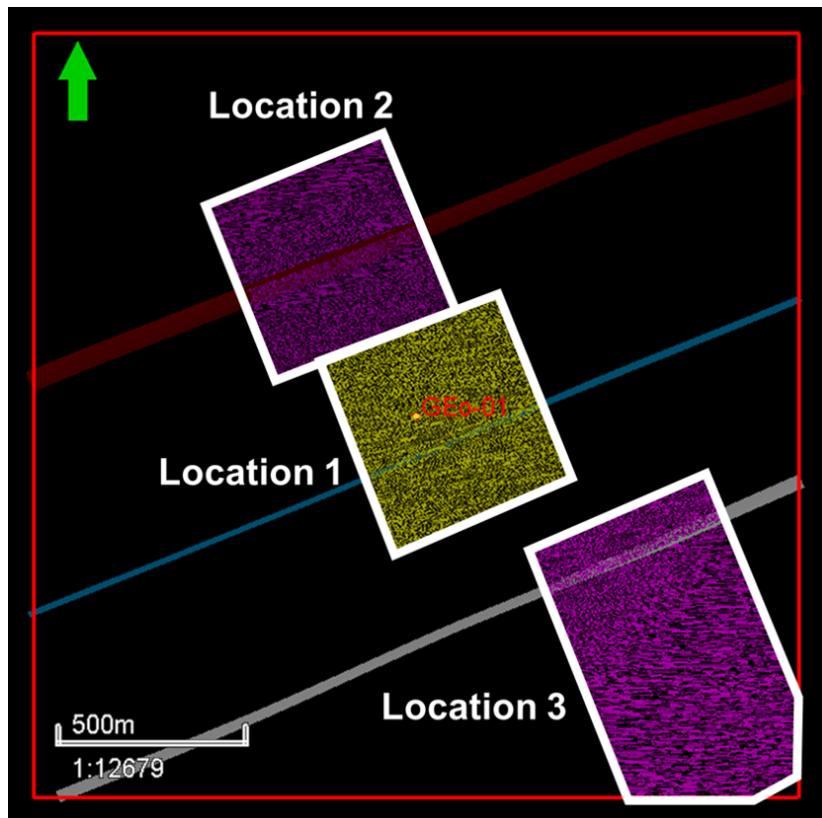


**Figure 6.4:** Map view of the study area showing the location of the generated DFN models in addition to the faults.

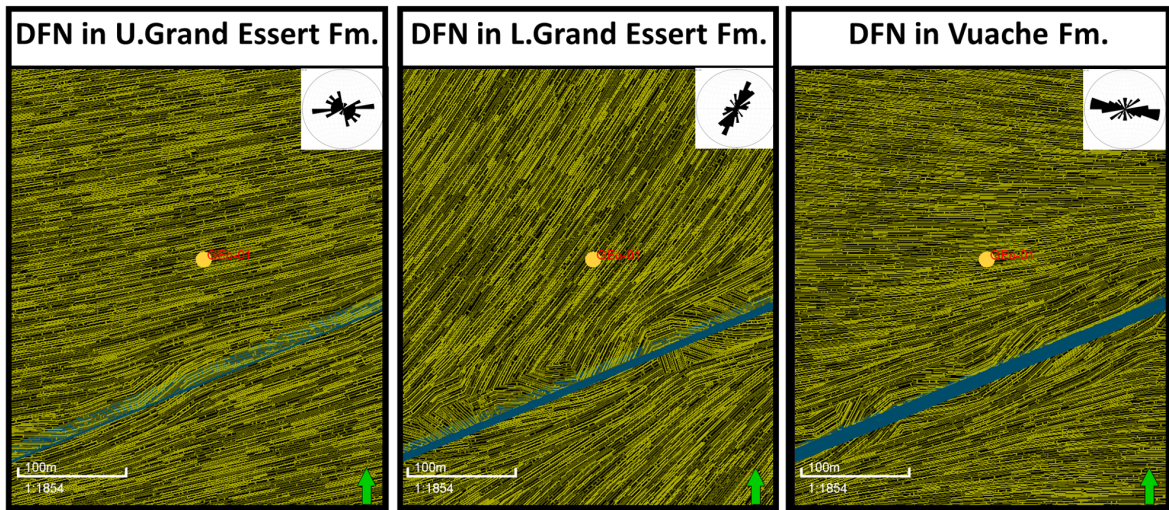


**Figure 6.5:** Examples of a single 2m layer of DFN for three formations around GGeo-01 location. The correspondent fracture strike rose diagram from GGeo-01 are presented in the right upper corner.

## 6.3 Evaluation and Discussion of the Results

### 6.3.1 Fracture Data Extraction and Analysis

The modelled fracture network in the DFN Generator tool consists of two fracture sets. This is because the DFN Generator considers the growth of two sets of fractures due to the initially distributed microfractures that are striking perpendicular to the horizontal principal strains. In addition, the strain is applied until no more macrofracture could nucleate or propagate and the fracture network becomes fully saturated.

The modelled fracture networks are considered fully anisotropic network. Those fully anisotropic networks consist of long and unbounded primary fractures that are connected by short secondary fractures which terminate against them (Figure 6.6 B).

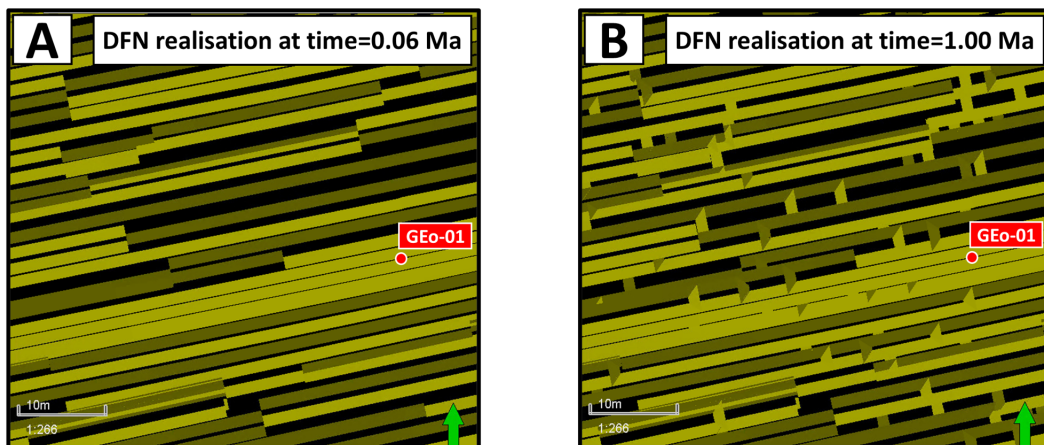


**Figure 6.6:** Close image for the modelled fracture geometry in Upper Grand Essert Fm. around GGeo-01. A) DFN realisation at time=0.06 Ma, B) Final DFN realisation at time=1.00 Ma.

During the propagation of the fully anisotropic network, the primary fracture set reaches saturation and stops growing before the secondary fracture set has started to grow (Figure 6.6 A and B). The primary set is striking perpendicular to the maximum horizontal strain whereas the secondary set is striking perpendicular to the minimum horizontal strain.

The fracture data of one modelled DFN layer include dip azimuth, dip angle, and length of the fractures. At Location 1 (500x500m), the number of the modelled fractures is around 95,000 fractures in one DFN layer. The length of the fractures ranges between 0.5 and 30 m with some exceptions where the length of the fractures can reach up to 75 m. The distribution of fracture length shows that more than half of the fractures have lengths of less than 3.25m (Figure 6.7). As expected, the distribution of the fracture dip azimuth of the full fracture data show two sets of fractures that are perpendicular to each other. For example, one DFN layer in Upper Grand Essert Fm. at Location 1 illustrates one fracture set dipping towards north and south and another fracture set dipping towards east and west (Figure 6.8 A).

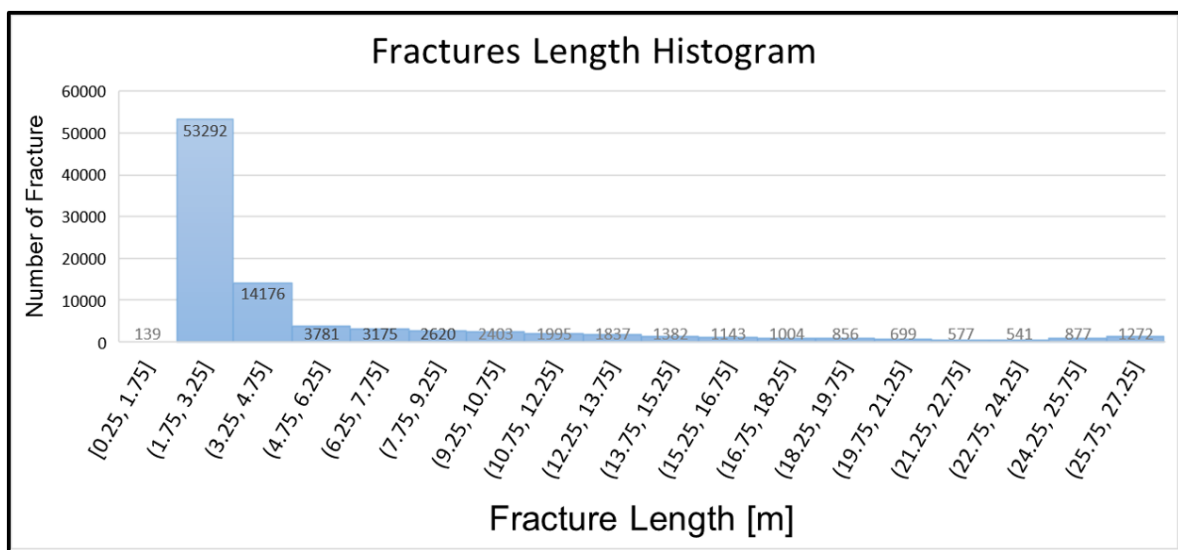


**Figure 6.7:** Histogram of the modelled fractures length in Upper Grand Essert Formation.

To observe the orientation of the primary fracture set, all the fractures that are longer than 3.25 m are considered as part of the primary fracture set. The full fracture data at Location 1 from the DFN layer in Upper Grand Essert were filtered by applying a fracture length cutoff of 3.25 m. The primary set show fractures that are dipping towards north and south (Figure 6.8 B). The filtering process shows that the primary set accounts for less than 50% of the total fractures in the modelled DFN. The same filter was applied to the DFN data of the other two formations, Lower Grand Essert and Vuache Formations. (Figure 6.9). All the fractures in the modelled DFNs have dip angle ranging between 50° and 70°.



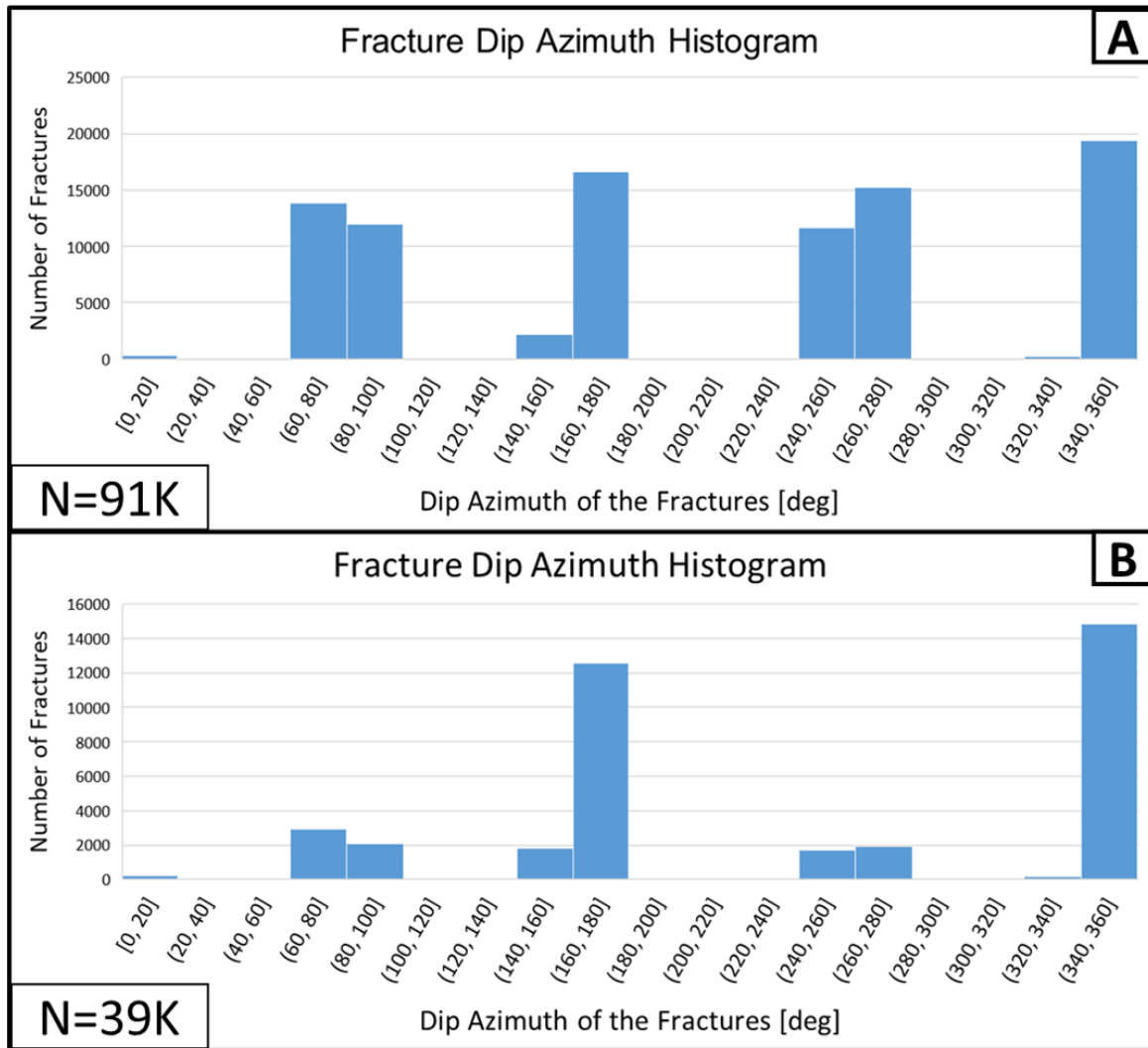


**Figure 6.8:** Fracture dip azimuth histogram on one DFN layer in Upper Grand Essert Fm. for A) Full exported data from one layer in Location 1, B) Filtered data using fracture length cutoff=3.25m in Location 1.

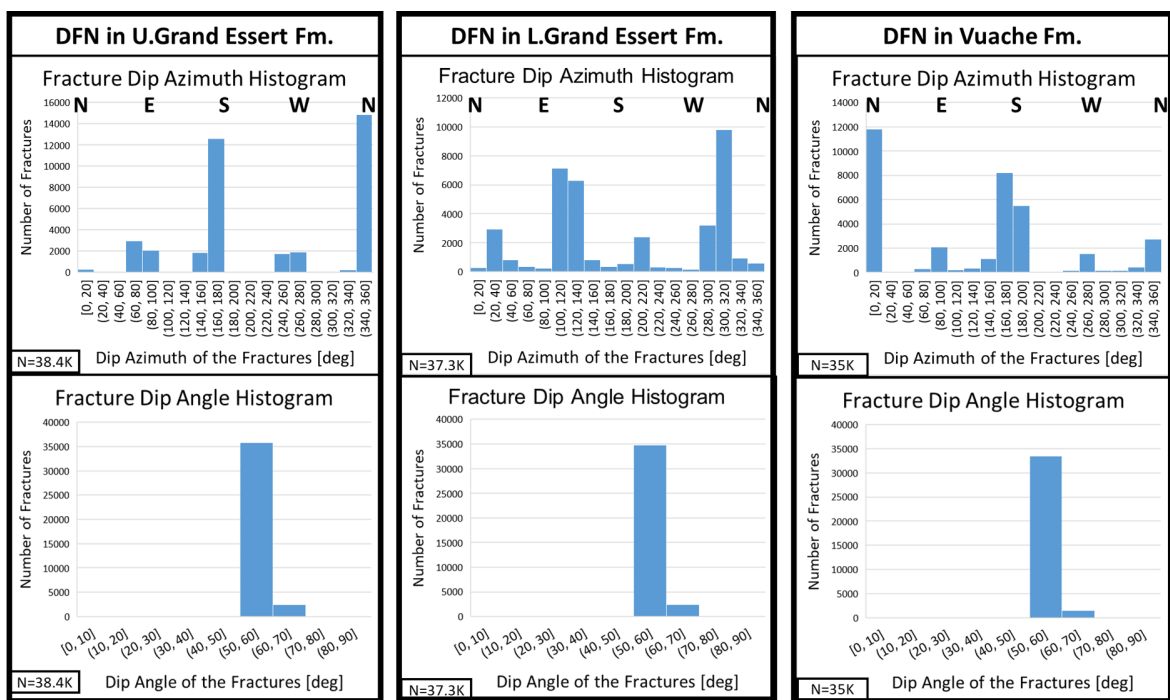


Figure 6.9: Top: Fracture dip azimuth histogram. Bottom: Fracture dip Angle histogram.

There are different methods to generate DFN models where they can be modelled based on stochastic generation and geomechanical simulation (Lei et al., 2017). Even though the stochastic DFN generation approach has the advantage of efficiency and it is applicable for various scale of 3D problems, it has some limitations. The stochastic approach over-simplifies the fracture geometries. It also include some uncertainties in statistical parameters and it ignores the tectonic and the mechanical properties constraints (Lei et al., 2017). On the hand, the geomechanical DFN simulation approach captures some mechanical characteristics of natural fractures . It is also constrained with the estimated paleostress fields (Lei et al., 2017). In this study, the geomechanical DFN approach was chosen because GEO-01 provides a constraint on the the mechanical properties of the subsurface rocks. In addition, the borehole fracture data provide an estimation of paleostress field during the fracture formation. Furthermore, a hybrid geomechanics-based stochastic simulation approach was used by Lo (2019) to generate a DFN model in Geneva Basin. A pure geomechanical modelling approach was adapted in this study to provide an alternative realization of DFN model in Geneva Basin. The adapted approach simulates the fracture growth under the constrain of the available data.

In this section, the advantages, weaknesses and uncertainties that are related to the produced DFN model will be discussed. Moreover, the implication for the Geothermal application and the improvement in future work that could be applied will be discussed as well.

## 7.1 Advantages and Limitation of the Modelling Approach

- One of the advantages of this approach is that it can resemble some of the fracture attributes. The produced DFN in this study mimics the the observed changed in fractures' directions in GEO-01 well. This is done by controlling the horizontal paleo-tectonic stress in different intervals separately.
- Another strength of this approach is that the modelled DFN is constrained away from the well location by the subsurface fault geometry and far-field tectonic stress. The fractures growth away from the faults is constrained by the applied horizontal strain and close to the faults the fracture growth is constrained by the perturbed stress field.
- On the other hand, this approach considers only a single tectonic regime that is responsible for the creation of all fractures. In case of multiple fracture sets that are formed under multiple tectonic regimes, they can not be simulated using this approach.
- The adapted approach produces DFN model that consist of several layers of layer-bound fractures. This makes the vertical extent of the fractures limited by the thickness of the modelled layers.
- The DFN forward modelling requires large computational time.

## 7.2 Assumptions and Uncertainties

The constructed subsurface fault geometry has uncertainty regarding the configuration of the faults. Since the inversion tool is sensitive to the fault geometry, the uncertainty of the fault geometry affects the paleostress inversion results, in turn, it affects the final DFN model.

The adapted modelling technique simulates the DFN model with the existence of the fault model. So, the modelled fractures are influenced by the perturbed stress field of the pre-existing faults. Therefore, this assumption introduces an uncertainty to the produced DFN model since the relative timing of the faults and the fractures creation in Geneva Basin is still unknown.

The relative magnitude and orientation of the paleo-tectonic stress are difficult to estimate (Maerten et al., 2016). In this study the configuration of the paleo-tectonic stress was defined based on the interpretation of the fractures pattern along the well borehole. The modelled fractures are dependant on the interpreted paleo-tectonic stress configuration. This introduces uncertainties to the DFN model since different paleo-tectonic stress configuration will result in different DFN model.

In addition, the strain and the duration of the fractures formation are assumed based on typical values provided by Welch et al. (2019) and Welch et al. (2020). The produced DFN model is dependant to those assumptions where different strain assumption can change the fracture network characteristics.

## 7.3 Implication for Geothermal Exploration

### 7.3.1 Applicability for Dynamic Modelling

The fracture networks contributes to the reservoir fluid flow by enhancing the reservoir permeability. The produced DFN model is supposed to visualize subsurface natural fracture network in the targeted reservoir in the study area. One way to evaluate the representativeness and the applicability of the produced DFN model to be used for geothermal application is to upscale it to a permeability model and use it in a dynamic simulation. The aim of this simulation is to compare the dynamic modeling results with the extended well test which was performed in GEO-01. Few points have to be taken in consideration regarding the produced DFN model before using it in a dynamic modelling:

- The DFN model has limitation in the vertical extent of the fractures where it consist of multiple layers of layer-bound fractures. This might affect the vertical permeability of the upscaled permeability model.
- As it is shown in Figure 6.6 in section 6.3.1, the produced DFN consist of two sets of fractures that are perpendicular to each other. The primary set consists of long fractures and the secondary set consists of very short fractures that are terminating against the fractures of the primary set. The secondary fracture set account for almost 55% of the total number of the modelled fractures. Comparing this with the observed fracture in GEO-01, the secondary set account for 30-40% of the full data. The number of the fractures in the secondary set in the modelled DFN is overestimated. This overestimation might influence the upscaled permeability model by changing the anisotropy of the permeability.

- Furthermore, the the present day in-situ stress orientation can cause fracture opening or closure where the apertures of fractures will be influenced (Min et al., 2004), Hence the present day in-situ stress configuration should be taken into account in the dynamic modelling since it can enhance or diminish the permeability of the natural fracture.

Two main challenges are associated with applying the modelling approach in this study on a larger scale:

- Creating the DFN model on a larger area using the same limited datasets will result in an under-constrained model. More data have to be acquired in new locations to constrain the large scale model.
- Sufficient computational power should be provided for a large scale DFN model creation since one of the limitation of this approach is that it requires large computational time.

### 7.3.2 Uncertainties Mitigation and Model Improvement

The fault model geometry has a major influence on the final modelled DFN (see section 5.2.1). Due to the lack of seismic data, the fault modelling process is associated with lots of assumptions and uncertainties. To reduce the uncertainty that is related to the subsurface fault model, the same DFN modelling approach can be applied again using different fault configurations such as orientation and lateral extension of the faults (e.g. Figure 7.1). The resulted DFN models from different fault configuration can be compared with the produced one in this study as well as other studies (e.g. Lo, 2019) by use them as inputs in the dynamic modelling.

Data acquisition is important to reduce the subsurface geological model uncertainty, especially 3D seismic survey where it provides the best representation to the subsurface geological model. Furthermore, To better understand the history of the fracture development and to reduce the uncertainties related to the predicted paleo-tectonic stress, outcrop study focusing on fracture population should be conducted (Doesburg, in prep - MSc 2021-2022). This will give more insight about the fracture system in a different dimension from the borehole fracture data such as the geological history, and fault-fracture relative formation timing.

Finally, new hybrid approaches to create DFN models that assimilate the advantages of different approaches should be investigated. This might help in creating a better fracture network that resemble the subsurface fracture network in the study area.

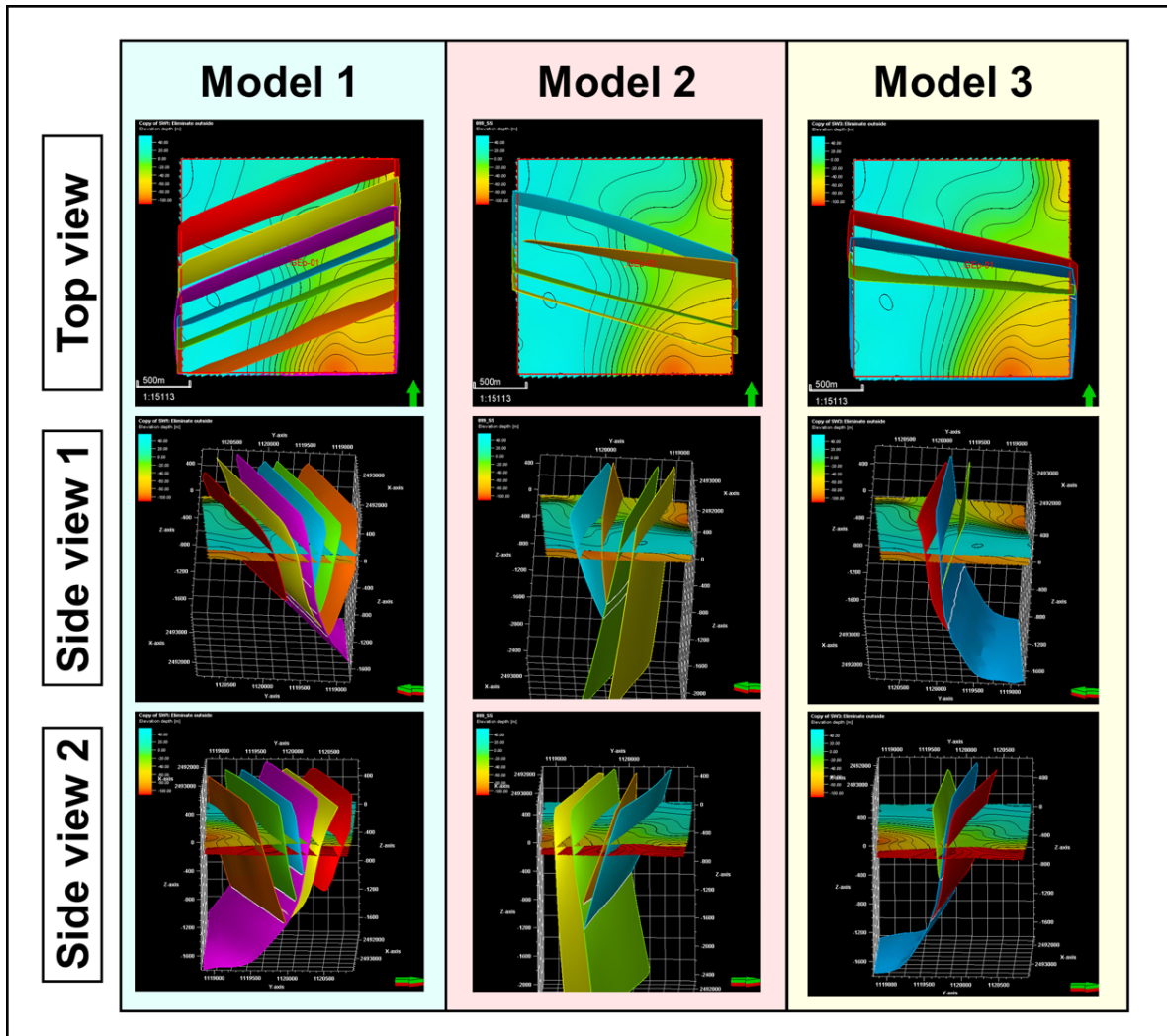


**Figure 7.1:** Three different fault model configurations in the study area. Model 1 is the base model that has been used in this study. Model 2 and 3 are possible fault models that are provided by the Department of Earth Science of the University of Geneva.

## Conclusion

---

The aim of this study is to reduce the risk of the ongoing Geothermal exploration program by estimating the influence of the natural fracture on the Lower Cretaceous reservoir in Geneva Basin. A Discrete Fracture Network (DFN) model was produced to represent the fracture network in a geothermal carbonate reservoir in the Lower Cretaceous. The work concerns DFN modelling using a novel workflow that utilizes geomechanical forward modelling techniques. The DFN model was constructed under the assumption of pre-existing faults. The DFN model was created using 2D seismic lines in addition to GGeo-01 well data including interpreted fractures using borehole images.

The DFN modelling inputs include geological subsurface model, fracture data, paleo-tectonic stresses configuration, Young's modulus and Poisson's ratio properties. Based on the 2D faults and horizons interpretation, a 3D geological model was constructed. The orientation of the faults were chosen to have a strike of N068°. In this project, the fracture data are assumed to be formed under single tectonic regime. The fracture pattern suggests that they were formed under a normal tectonic regime. The Young's modulus and Poisson's ratio logs were calculated using empirical relations and velocity well log. The calculated Young's modulus and Gamma ray logs were used to partition the formations of interest in mechanical units. The Lower Cretaceous Interval was divided into 9 layers based on rock's mechanical layering. The analysis of the fracture data illustrates a change in the direction of the fractures with depth. This change in fractures' direction could be explained by the variation in rock's stiffness between different stratigraphic layers.

Two techniques were used to model the subsurface fracture network: paleo-tectonic stress inversion technique and fracture network forward modelling (DFN Generator) technique. The DFN creation workflow start by using paleo-tectonic stress inversion tool to evaluated the fitting between the observe fractures and the interpreted configuration of paleo-stresses under the existence of the faults. Principal strain tensors, that are related to the interpreted stress configuration, were produced by the paleo-tectonic stress inversion tool. The principal strain tensor were used to calculate the strain related models which in turn were used along with the the Young's modulus and Poisson ratio models as inputs for the DFN Generator. The modelled DFN replicates the change in direction of the fractures at the well location. Away from the well, the DFN model is constrained by the subsurface fault geometry and far-field tectonic stress.

One of the approach limitation is that it cannot be used to simulate fracture sets that are resulted from multiple tectonic regimes. Another approach limitation is that it produces only layer-bound fractures where the fractures' vertical extend is limited to the top and bottom of the layers in the constructed 3D grid. Additionally, The forward modelling tool require large computational power. Several assumptions are made though the DFN generation such as the orientation of the fault geometry, relative timing between the faults and fracture formation, and the assumption of the single tectonic regime. Those assumptions introduce uncertainties to the final DFN model. To reduce the uncertainties of the modelled DFN, more data should be acquired especially 3D seismic survey to better constrain the subsurface geological model.

Field study should be conducted to constrain the predicted paleo-tectonic stress and gain more insight about the fracture system.

The applicability of the DFN model to the Geothermal application can be investigated by upscaling it to permeability model and use it in a dynamic modelling simulation. The results of the dynamic modelling can be compared with the extended well test which was performed in GGeo-01. The limitation and the uncertainties of the model should be considered during the dynamic modelling.



# References

---

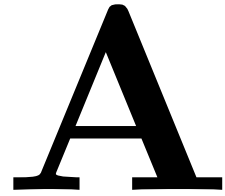
- Bai, T., Pollard, D., and Gao, H. (2000). Explanation for fracture spacing in layered materials. *Nature*, 403(6771):753–756.
- Bai, T. and Pollard, D. D. (2000). Fracture spacing in layered rocks: a new explanation based on the stress transition. *Journal of Structural Geology*, 22(1):43–57.
- Barnston, A. G. (1992). Correspondence among the correlation, rmse, and heidke forecast verification measures; refinement of the heidke score. *Weather and Forecasting*, 7(4):699–709.
- Boersma, Q. (2020). Natural fracture network characterisation: Numerical modelling, outcrop analysis and subsurface data.
- Bourne, S. J. (2003). Contrast of elastic properties between rock layers as a mechanism for the initiation and orientation of tensile failure under uniform remote compression. *Journal of Geophysical Research: Solid Earth*, 108(B8).
- Brentini, M. (2018). *Impact d'une donnée géologique hétérogène dans la gestion des géoressources: analyse intégrée et valorisation de la stratigraphie à travers le bassin genevois (Suisse, France)*. PhD thesis, University of Geneva.
- Chelle-Michou, C., Do Couto, D., Moscariello, A., Renard, P., and Rusillon, E. (2017). Geothermal state of the deep western alpine molasse basin, france-switzerland. *Geothermics*, 67:48–65.
- Clerc, N., Rusillon, E., Moscariello, A., Renard, P., Paolacci, S., and Meyer, M. (2015). Detailed structural and reservoir rock typing characterisation of the greater geneva basin, switzerland, for geothermal resource assessment. In *Proceedings World Geothermal Congress*.
- Gudmundsson, A. (2011). *Rock fractures in geological processes*. Cambridge University Press.
- Healy, D., Blenkinsop, T. G., Timms, N. E., Meredith, P. G., Mitchell, T. M., and Cooke, M. L. (2015). Polymodal faulting: Time for a new angle on shear failure. *Journal of Structural Geology*, 80:57–71.
- Higgins-Borchardt, S., Sitchler, J., and Bratton, T. (2016). Chapter 7 - geomechanics for unconventional reservoirs. In Ma, Y. Z. and Holditch, S. A., editors, *Unconventional Oil and Gas Resources Handbook*, pages 199–213. Gulf Professional Publishing, Boston.
- Homberg, C., Bergerat, F., Philippe, Y., Lacombe, O., and Angelier, J. (2002). Structural inheritance and cenozoic stress fields in the jura fold-and-thrust belt (france). *Tectonophysics*, 357(1-4):137–158.
- Johri, M., Zoback, M. D., and Hennings, P. (2014). A scaling law to characterize fault-damage zones at reservoir depths. *AAPG Bulletin*, 98(10):2057–2079.
- Kenter, J. A., Braaksma, H., Verwer, K., and van Lanen, X. M. (2007). Acoustic behavior of sedimentary rocks: Geologic properties versus poisson's ratios. *The Leading Edge*, 26(4):436–444.

- Koumrouyan, M. (2019). *Geomechanical Characterisation of Geothermal Exploration Borehole: Implication for the GGeo-01 Well, in Geneva*. PhD thesis, Centre d'hydrogéologie et de géothermie CHYN-Université de Neuchâtel.
- Laubach, S. E., Lander, R., Criscenti, L. J., Anovitz, L. M., Urai, J., Pollyea, R., Hooker, J. N., Narr, W., Evans, M. A., Kerisit, S. N., et al. (2019). The role of chemistry in fracture pattern development and opportunities to advance interpretations of geological materials. *Reviews of Geophysics*, 57(3):1065–1111.
- Lei, Q., Latham, J.-P., and Tsang, C.-F. (2017). The use of discrete fracture networks for modelling coupled geomechanical and hydrological behaviour of fractured rocks. *Computers and Geotechnics*, 85:151–176.
- Lo, H. Y. (2019). *Discrete fracture network modelling in the Geneva Basin (Lower Cretaceous carbonates): implication for geothermal exploration*.
- Maerten, L., Maerten, F., Lejri, M., and Gillespie, P. (2016). Geomechanical paleostress inversion using fracture data. *Journal of structural Geology*, 89:197–213.
- Mari, J.-L. and Vergniault, C. (2021). Sismique en forage et diagraphies acoustiques. In *Sismique en forage et diagraphies acoustiques*. EDP Sciences.
- Matte, P. (2001). The variscan collage and orogeny (480–290 ma) and the tectonic definition of the armorica microplate: a review. *Terra nova*, 13(2):122–128.
- Min, K.-B., Rutqvist, J., Tsang, C.-F., and Jing, L. (2004). Stress-dependent permeability of fractured rock masses: a numerical study. *International Journal of Rock Mechanics and Mining Sciences*, 41(7):1191–1210.
- Moeck, I. S. (2014). Catalog of geothermal play types based on geologic controls. *Renewable and Sustainable Energy Reviews*, 37:867–882.
- Moscariello, A. (2016). Geothermal exploration in sw switzerland. In *European Geothermal Congress*.
- Moscariello, A. (2019). Exploring for geo-energy resources in the geneva basin (western switzerland): opportunities and challenges. *Swiss Bulletin für angewandte Geologie*, 24(2):105–124.
- Moscariello, A. (2021). The geomorphological landscapes in the geneva basin. In *Landscapes and landforms of Switzerland*, pages 83–96. Springer.
- Moscariello, A., Gorin, G., Charollais, J., and Russillon, E. (2014). Geology of western switzerland and nearby france in a geo-energy perspective.
- Nelson, R. (2001). *Geologic analysis of naturally fractured reservoirs*. Elsevier.
- Rawnsley, K., Rives, T., Petti, J.-P., Hencher, S., and Lumsden, A. (1992). Joint development in perturbed stress fields near faults. *Journal of Structural Geology*, 14(8-9):939–951.
- Roylance, D. (2001). Transformation of stresses and strains. *Lecture Notes for Mechanics of Materials*.

- Rusillon, E. (2017). *Characterisation and rock typing of deep geothermal reservoirs in the Greater Geneva Basin (Switzerland & France)*. PhD thesis, University of Geneva.
- Schlumberger (1991). *Log interpretation principles/applications*. Schlumberger Educational Services.
- Sibson, R. H. (1998). Brittle failure mode plots for compressional and extensional tectonic regimes. *Journal of Structural Geology*, 20(5):655–660.
- SIG (2018). Demande de contribution à la recherche de ressources géothermiques dans le canton de Genève : phase de prospection - programme géothermie 2020.
- Stephansson, O. and Zang, A. (2012). ISRM suggested methods for rock stress estimation—part 5: establishing a model for the in situ stress at a given site. *Rock Mechanics and Rock Engineering*, 45(6):955–969.
- Strasser, A., Charollais, J., Conrad, M. A., Clavel, B., Pictet, A., and Mastrangelo, B. (2016). The cretaceous of the swiss jura mountains: an improved lithostratigraphic scheme. *Swiss Journal of Geosciences*, 109(2):201–220.
- Trice, R. (1999). A methodology for applying a non unique, morphological classification to sine wave events picked from borehole image log data. *Geological Society, London, Special Publications*, 159(1):77–90.
- Welch, M., Lüthje, M., and Oldfield, S. (2020). *Modelling the Evolution of Natural Fracture Networks*. Springer.
- Welch, M. J., Luthje, M., and Glad, A. C. (2019). Influence of fracture nucleation and propagation rates on fracture geometry: insights from geomechanical modelling. *Petroleum Geoscience*, 25(4):470–489.
- Yasar, E. and Erdogan, Y. (2004). Correlating sound velocity with the density, compressive strength and young’s modulus of carbonate rocks. *International Journal of Rock Mechanics and Mining Sciences*, 41(5):871–875.



# Fracture Data



## Lithology Based

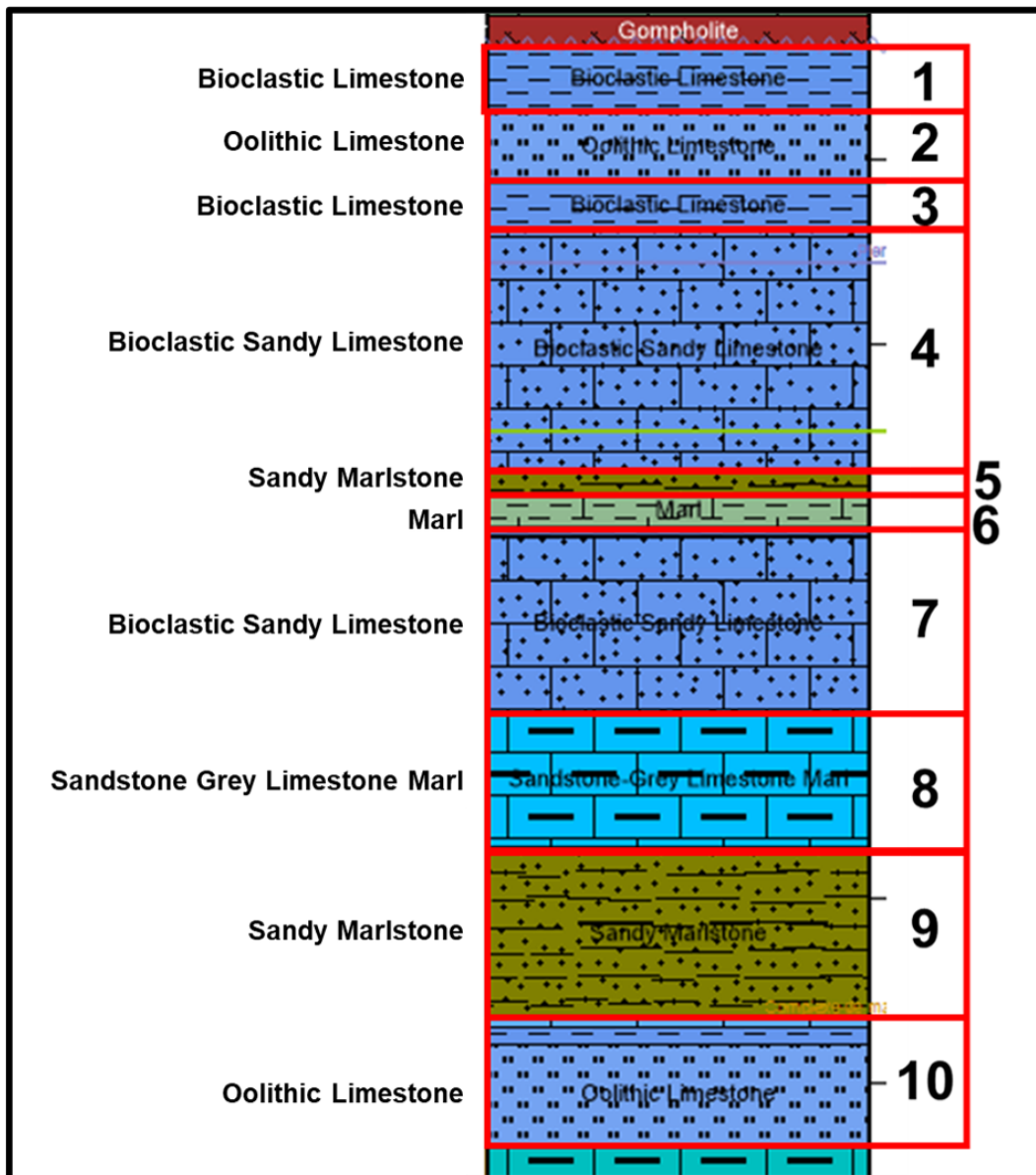
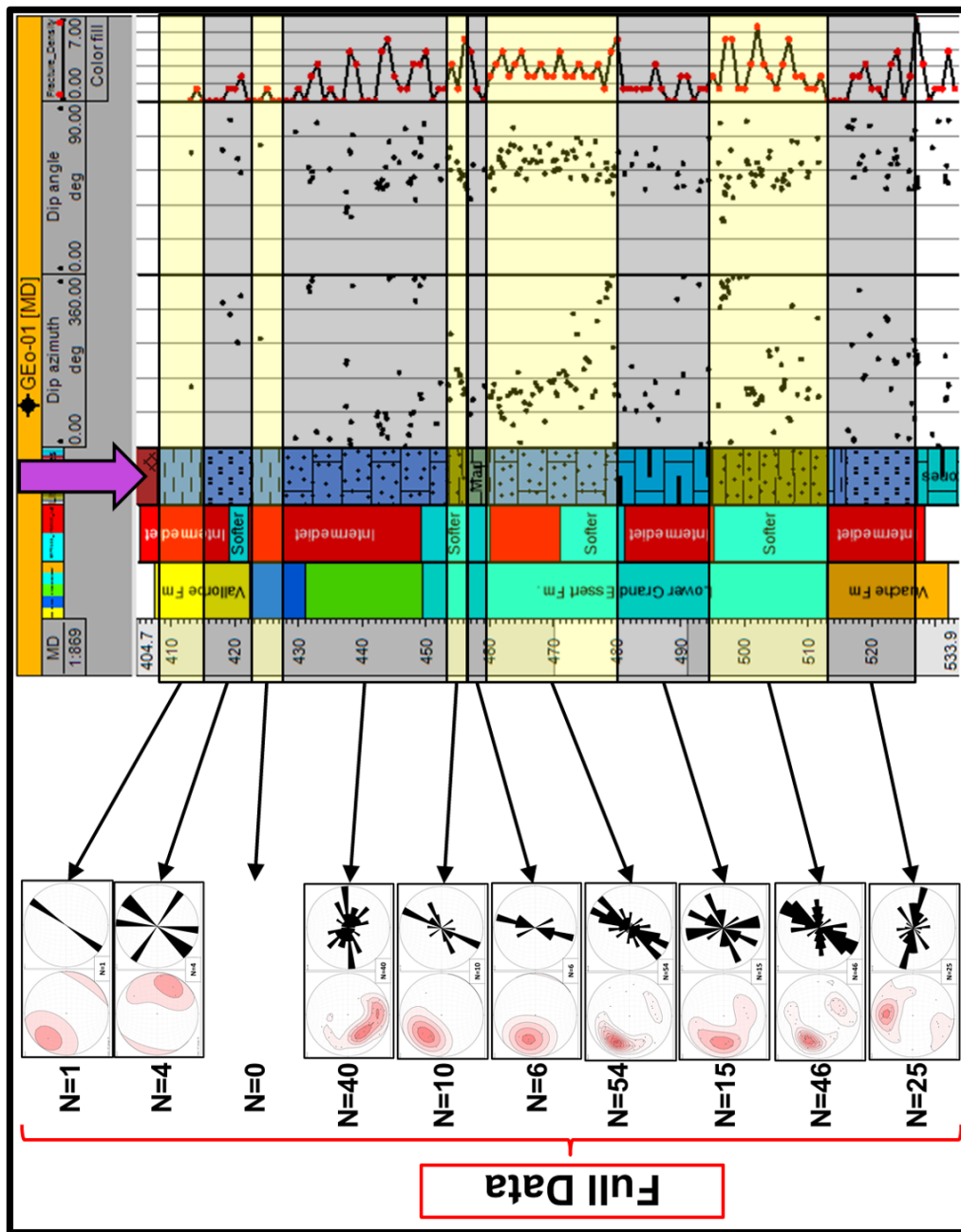
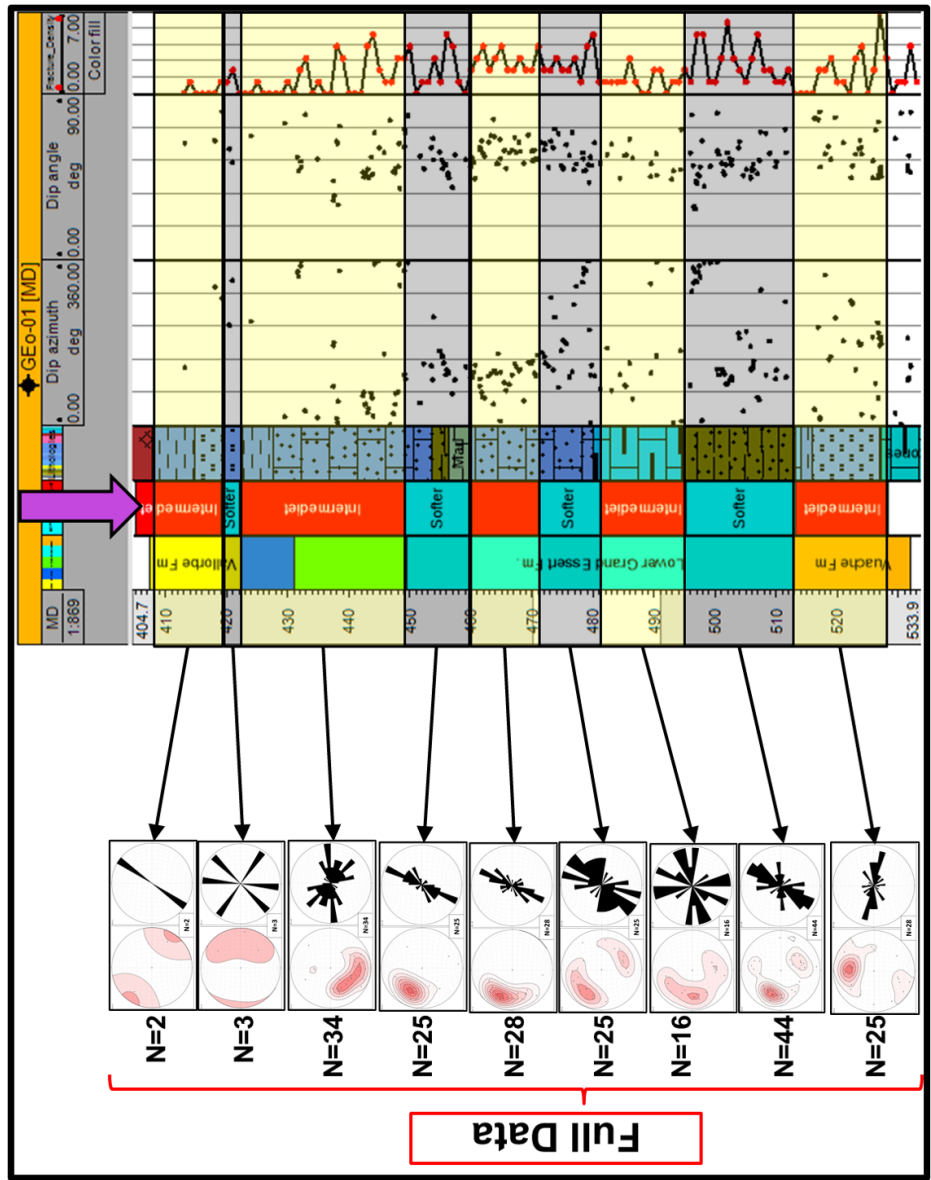


Figure A.1: Categorization of different lithology layers.



**Figure A.2:** This figure shows the fractures data for the 10 different lithology layers. Full Data include all the fractures. 2 Sets Data include on the the NNE-SSW and the E-W sets.

# Geomechanical Based



**Figure A.3:** This figure shows the fractures data for the 9 different geomechanical layers. Full Data include all the fractures. 2 Sets Data include on the the NNE-SSW and the E-W sets.

# Formation Based

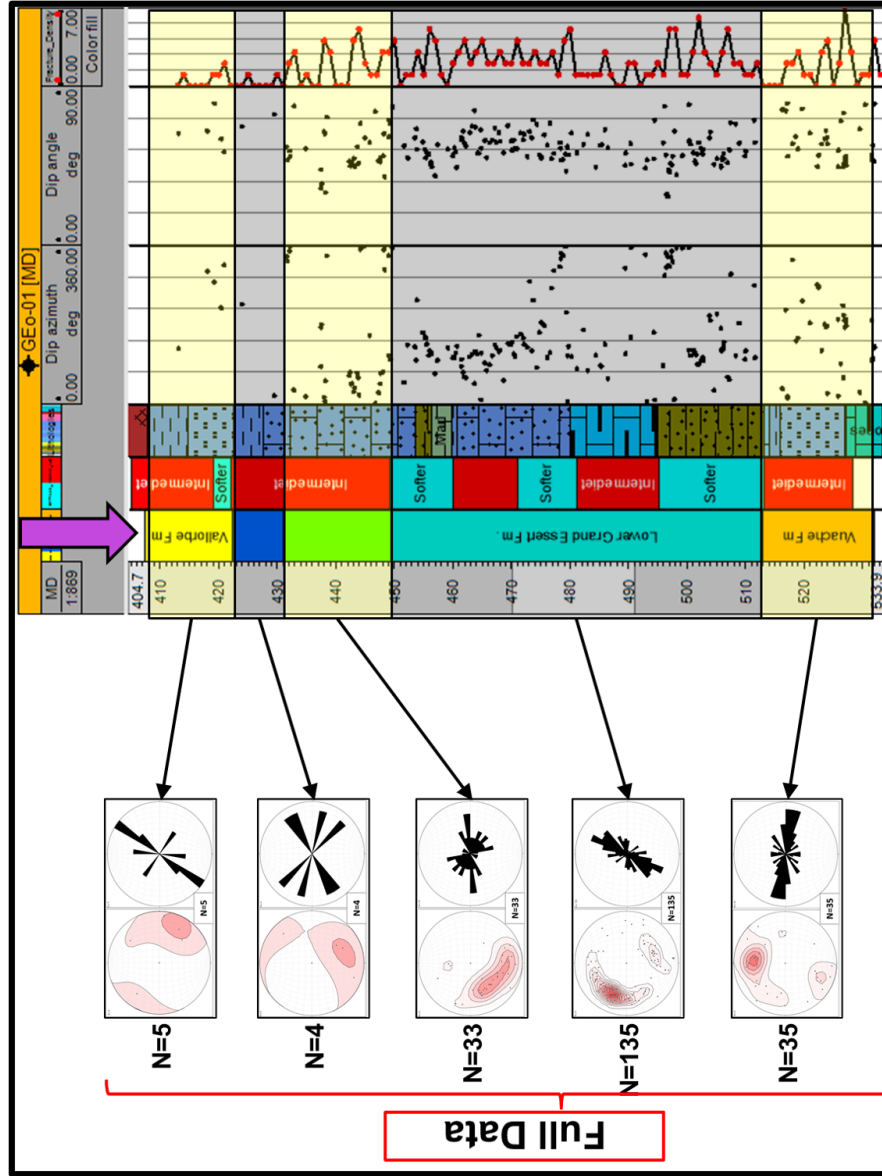


**Figure A.4:** This figure shows the fractures data for the 5 different lithological formation. Full Data include all the fractures. 2 Sets Data include on the the NNE-SSW and the E-W sets.



## B.1 DFN Generator Input

The screenshot shows a software interface with a tabbed menu at the top containing 'Main settings', 'Mechanical properties', 'Stress state', 'Outputs', and 'Control parameters'. The 'Main settings' tab is active. The interface contains the following fields and controls:

- Model name:** A text input field containing 'New DFN' and a blue question mark icon.
- Grid:** A button with a right-pointing arrow and a blue question mark icon, followed by an empty text input field.
- Start column (I index):** A text input field containing '1'.
- Number of columns (I index):** A text input field containing '1' and a blue question mark icon.
- Start row (J index):** A text input field containing '1'.
- Number of rows (J index):** A text input field containing '1' and a blue question mark icon.
- Top of brittle layer (K index):** A text input field containing '1'.
- Bottom of brittle layer (K index):** A text input field containing '1' and a blue question mark icon.
- Minimum horizontal strain azimuth (deg):** A button with a right-pointing arrow, an empty text input field, 'Default value' 0, 'deg', and a blue question mark icon.
- Minimum horizontal strain rate (/ma, tensile negative):** A button with a right-pointing arrow, an empty text input field, 'Default value' -0.01, '/ma', and a blue question mark icon.
- Maximum horizontal strain rate (/ma, tensile negative):** A button with a right-pointing arrow, an empty text input field, 'Default value' 0, '/ma', and a blue question mark icon.
- Generate explicit DFN?:** A checked checkbox and a blue question mark icon.
- Number of intermediate outputs:** A dropdown menu showing '0' and a blue question mark icon.

Figure B.1: Main settings

## B.2 Large DFN Figures

Parameter	Default Value	Unit
Young's Modulus (Pa)	10000000000	Pa
Poisson's ratio	0.25	
Biot coefficient	1	
Friction coefficient on the fractures	0.5	
Crack surface energy (J/m <sup>2</sup> )	1000	J/m <sup>2</sup>
Rock strain relaxation time constant (ma)	0	ma
Fracture strain relaxation time constant (ma)	0	ma
Initial microfracture density (fracs/m <sup>3</sup> )	0.001	fracs/m <sup>3</sup>
Initial microfracture size distribution coefficient	2	
Subcritical fracture propagation index	10	
Critical fracture propagation rate (m/s)	2000	

Average mechanical properties across all cells?

Figure B.2: Mechanical properties inputs

Parameter	Value	Unit
Stress distribution scenario	Stress shadow	
Depth at time of deformation (m)	400	m
Mean density of overlying sediments (kg/m <sup>3</sup> )	2400	kg/m <sup>3</sup>
Fluid density (kg/m <sup>3</sup> )	1000	kg/m <sup>3</sup>
Initial fluid overpressure (Pa)	0	Pa
Initial stress relaxation	1	

Average stress/strain state across all cells?

Figure B.3: Stress State inputs

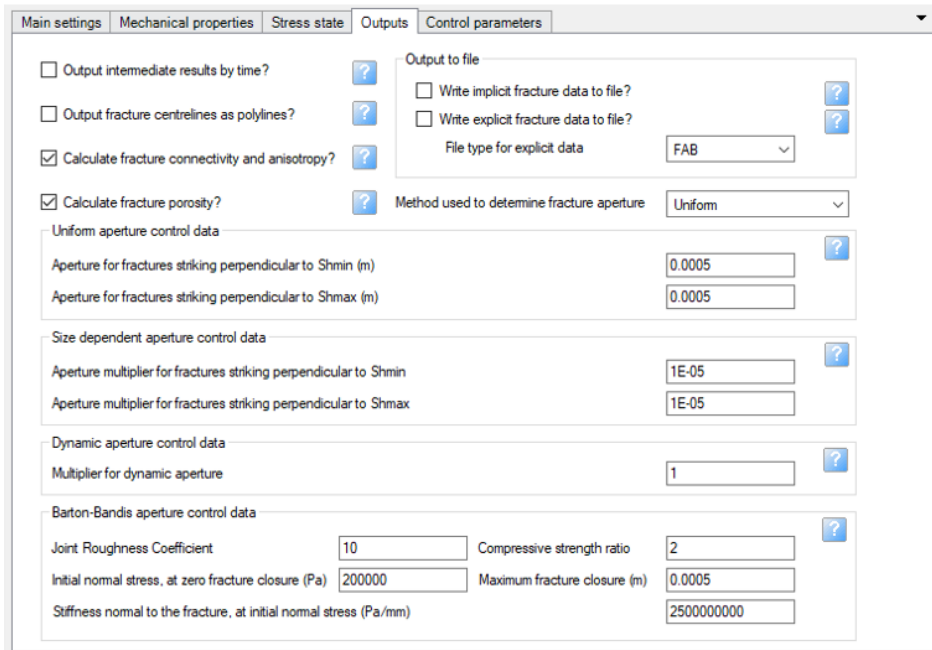


Figure B.4: Outputs control

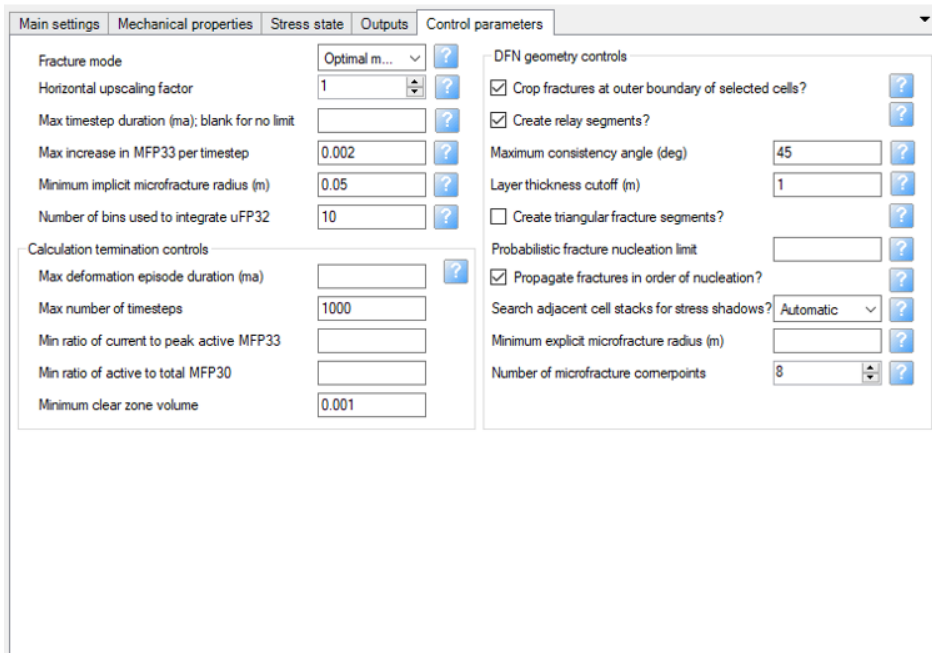
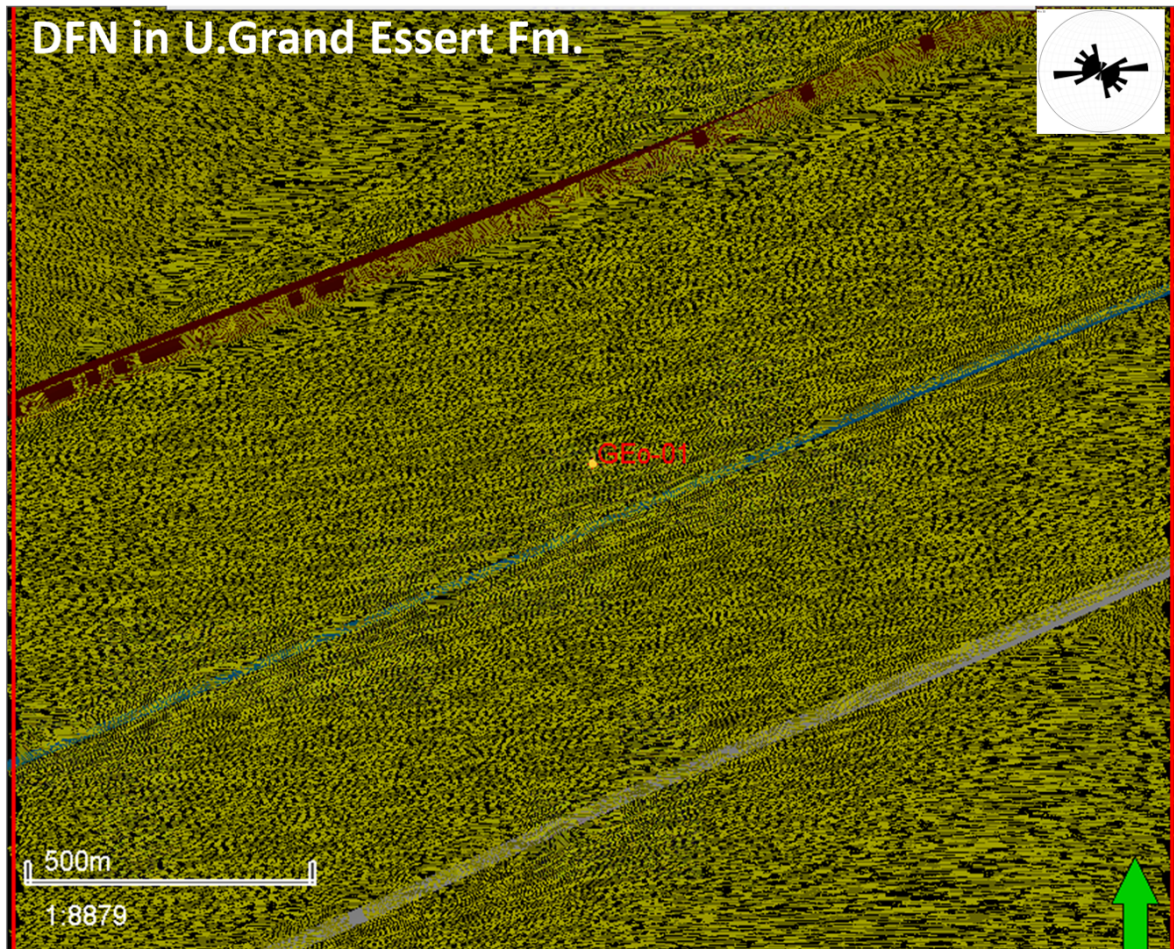
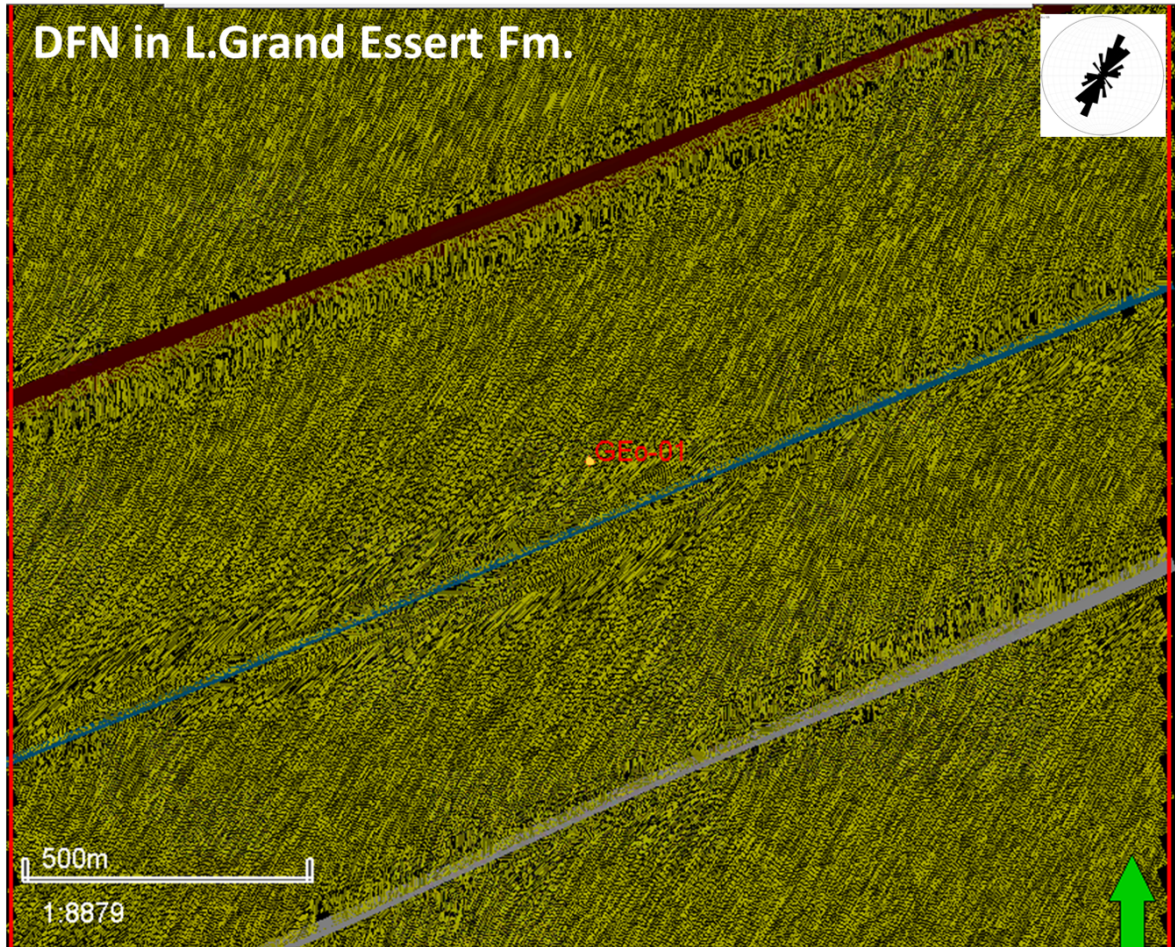


Figure B.5: Control parameters



**Figure B.6:** DFN result in U. Grand Essert Formation. The correspondent strike rose diagram is presented in the right upper corner.



**Figure B.7:** DFN result in L. Grand Essert Formation. The correspondent strike rose diagram is presented in the right upper corner.

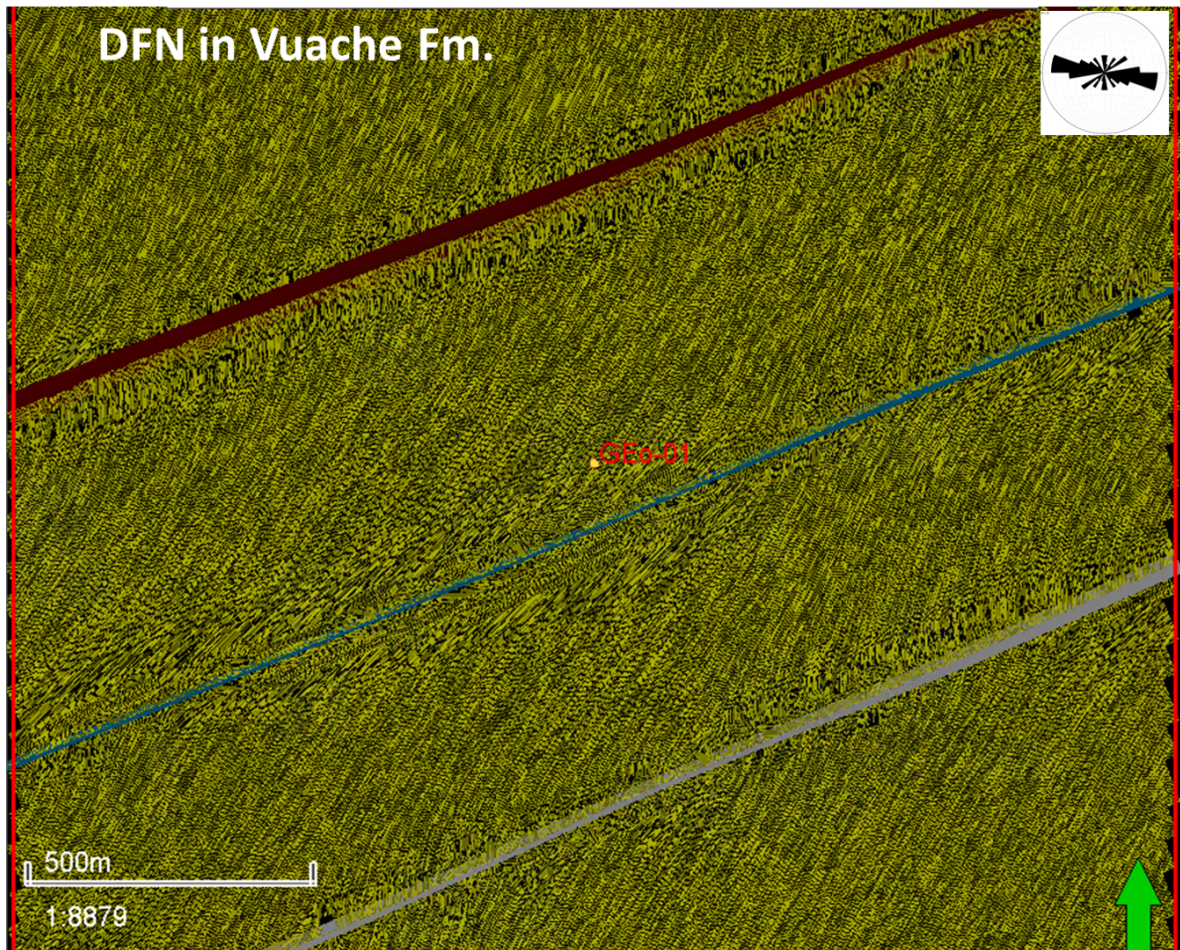


**Figure B.8:** DFN result in Vuache Formation. The correspondent strike rose diagram is presented in the right upper corner.